2017

Numerical Simulations of Mass Transfer in Close and Contact Binaries Using Bipolytropes

Kundan Vaman Kadam
Louisiana State University and Agricultural and Mechanical College

NUMERICAL SIMULATIONS OF MASS TRANSFER IN CLOSE AND CONTACT BINARIES USING BIPOLYTROPES

A Dissertation

Submitted to the Graduate Faculty of the
Louisiana State University and
Agricultural and Mechanical College
in partial fulfillment of the
requirements for the degree of
Doctor of Philosophy

in

The Department of Physics and Astronomy

by
Kundan Vaman Kadam
B.S. in Physics, University of Mumbai, 2005
M.S., University of Mumbai, 2007
May 2017

Acknowledgments

I am grateful to my advisor, Geoff Clayton, for supporting me wholeheartedly throughout the graduate school and keeping me motivated even when things didn't go as planned. I'd like to thank Hartmut Kaiser for allowing me to work on my dissertation through the NSF CREATIV grant. I am thankful to Juhan Frank for insightful discussions on the physics of binary systems and their simulations. I am thankful to Joel Tohline for discussions about bipolytropes. His excitement about simulating "bi-bi-polytropes" (bipolytropic binaries) someday, was contagious. I am thankful to Jan Staff for guiding me through the initial Flow-ER code simulations. I'd like to thank Dominic Marcello for developing Octotiger, and helping me with the code and the simulations. I am thankful to Patrick Motl for numerous perceptive discussions on VoIP about binary evolution and numerical hydrodynamics. After addressing his comments on the manuscripts, I feel like there is nothing left for the referee to throw at me. I'd like to thank my mom and my sister for enabling me to pursue a career I find meaningful. Lastly, I'd like to thank my friends who were there for me when I needed them.

Contents

List of Tables

List of Figures

Abstract

We present the first self-consistent, three dimensional study of hydrodynamic simulations of mass transfer in close and contact binary systems, with both stars represented as bipolytropes (composite polytopes). The project is motivated by the recent eruption of V1309 Scorpii which was proved to be the merger of a contact binary system. The final eruption is assumed to be the disruption of the core of the secondary inside the more massive star.

The initial, equilibrium binary models are rotating synchronously in circular orbits and are obtained using the Bipolytropic Self Consistent Field (BSCF) technique, which is a modification of Hachisu's Self Consistent Field (HSCF) method. Both stars have a fully resolved core and envelope structure where the difference in equation of state is represented by different polytropic indices and the difference in composition is represented as the ratio of the average molecular weights. The validity of the BSCF method is confirmed by constructing single, rapidly rotating stars and toroidal disks and comparing their properties with well established numerical as well as analytical results.

We simulate mass transfer and mergers of bipolytropic binary systems using two fully three-dimensional grid-based Eulerian codes, Flow-ER and Octotiger, at two different resolutions. We discuss the suitability of both the codes to simulate bipolytropic stellar binaries faithfully. The simulations conducted using the Flow-ER code show certain numerical artifacts due to the limited resolving capacity of the implemented fixed cylindrical grid. We compare the results of these simulations with ones carried out using Octotiger with Adaptive Mesh Refinement (AMR) capabilities, where most of the limitations have been improved upon. The initial conditions for each simulation across the codes are chosen to match as closely as possible so that the simulations can be used as benchmarks. Although there are some key differences, the detailed comparison of the simulations suggests that there is remarkable agreement between the results obtained using the two codes. With the comparison across the resolutions, we find that both the hydrodynamic codes are convergent. This study enables us to confidently simulate mass transfer and merger scenarios of binary systems involving bipolytropic components.

Chapter 1
Introduction

In the simplest terms, a contact binary is a system of two stars that are so close to each other that the distance between them is smaller than their combined radii. As a consequence, they revolve around the common center of mass while touching each other, like a pair of peanuts inside their common shell (see Figure 1.1). Contact binary systems are also known as W Ursae Majoris or W UMa type stars, after the prototype discovered in 1903 (Müller & Kempf, 1903). About one in every 500 stars is actually a binary system of W Uma type in the Galactic disk (Rucinski, 2006). From a statistical analysis of observed contact binary systems, Li *et al.* (2007) show that these systems are long-lived and secularly stable on nuclear timescale, with a lifetime of a few billion years. Somehow, nature is able to get these two stars to coexist as an intimately interacting pair for a relatively long time. It was assumed that this kind of system naturally proceeds toward merger (Robertson & Eggleton, 1977). The merged object is believed to eventually form a blue straggler, an anomalously young-looking star for a given cluster. The merger event itself is relatively rare, since it proceeds on the timescale of the order of less than an hour and until recently, there were no confirmed observations of such a coalescence event.

The eruption of V1309 Scorpii started like an ordinary nova on September $2^{\rm nd}$, 2008 (Nakano *et al.*, 2008). The event was classified as a nova because of the rapid increase in brightness and location inside our galaxy. Soon after its discovery, however, it was clear that the V1309 Sco eruption was not a nova. As more spectroscopic data became available, it was realized that the remnant had cooled very rapidly in a matter of days (Mason *et al.*, 2010). This was an indication that the nova belonged to a peculiar class called "luminous red novae" (LRN), because the spectrum becomes redder or cooler as the remnant evolved. This is also called a V838 Mon type event, after the prototype. Before V1309 Sco, there were several possible explanations for a V838 Mon type event. Munari & Henden (2005) proposed a thermonuclear shell event in an evolved massive star, while Lawlor (2005) considered a very late He-shell flash in a post-asymptotic giant branch (AGB) star. Other proposed explanations involved stellar mergers (Soker & Tylenda, 2003) and red giants swallowing planets (Retter & Marom, 2003).

The progenitor of V1309 Sco was fortituously in the field of view of the OGLE (Optical Gravitational Lensing Experiment) project for about six years before the outburst. OGLE archival photometric data show telltale signs of an eclipsing contact binary in the pre-outburst lightcurve (Tylenda *et al.*, 2011), thus proving that red novae can indeed result from the coalescence of two stars. This discovery was remarkable because we have now observed a stellar merger event in real time. Thus the eruption of V1309 Sco may be considered a Rosetta stone in the studies of the nature of V838 Mon type eruptions.

Although contact binary systems have been known for over a century, their nature still remains enigmatic. Observationally, the light curve of a contact binary system has almost equal depth minima (Figure 2.4), hence the temperature of the components is very nearly equal. This is true

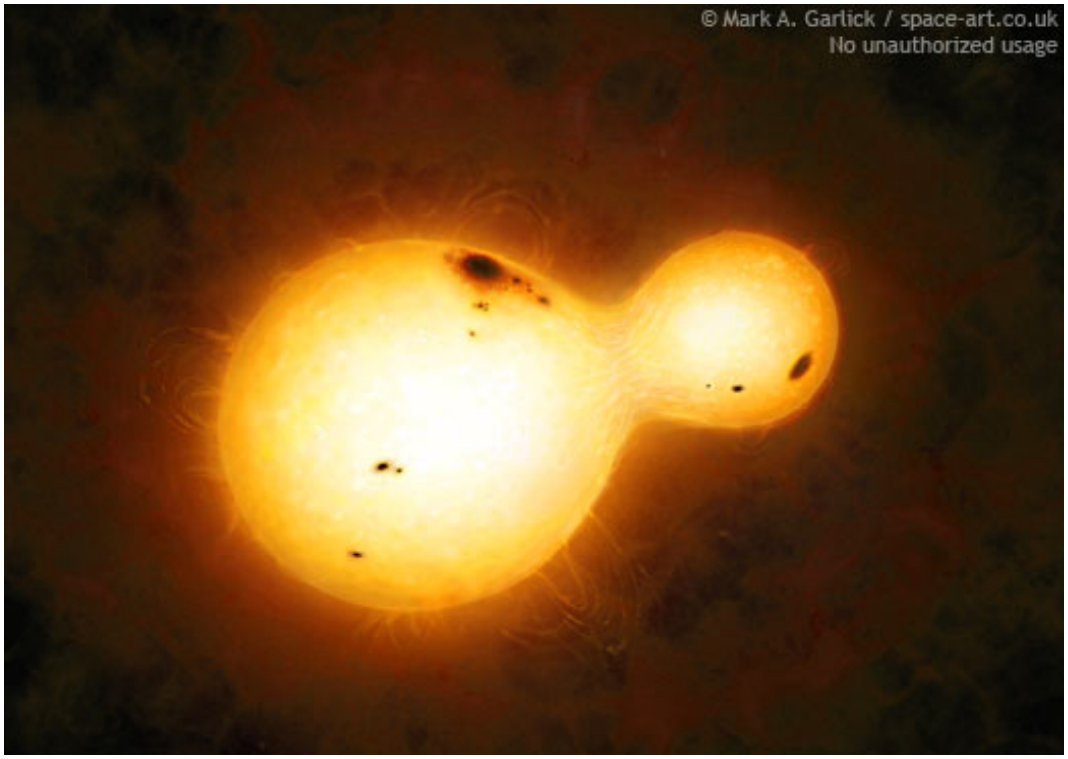

FIGURE 1.1: An artist's conception of a W UMa type system (Copyright Mark A. Garlick / space-art.co.uk).

even when the two stars have very different masses, with the mass ratio (q) as low as 0.1 (Rasio, 1995). There are two major issues with the interpretation of the observations pertaining to these systems. First, Kuiper (1941) demonstrated that a contact binary system cannot simply form by bringing together two unequal, zero-age main-sequence (ZAMS) components (Kuiper's paradox). This is because the stellar radii have to satisfy two contradictory conditions simultaneously, one relates to the mass-radius relation of the main-sequence stars and the other relates to the size of the Roche lobes in a binary system. The second issue, called Lucy's paradox, is the problem of luminosity redistribution in the contact system so as to make the surface brightness nearly equal.

A model for contact binaries should explain the observed properties, secular stability of the system as well as their formation scenario and evolutionary status. In this respect, there are two contending theories, the discontinuity theory (DSC) and the thermal relaxation oscillation (TRO) model as summarized in Shu (1980). Lucy (1968) argued that the observed properties imply that a contact binary either evolves subsequently from an initially detached binary or the structure is not in thermal equilibrium. The DSC theory proposed by Shu *et al.* (1976a) assumes a discontinuity against thermal diffusion at the base of the common envelope. Flannery (1976) showed that the structure of a contact binary with a common convective envelope is unstable when subject to mass transfer. He, along with Lucy (1976), advanced the TRO model where individually, both components are out of thermal equilibrium and the system oscillates between contact and semi-detached states on a thermal timescale.

Another major puzzle pertaining to contact binary systems is their evolutionary status. One of the earlier theories for the origin of a contact binary system was fission from a single, rapidly rotating star, but this argument had serious flaws. According to known models of stellar evolution, stars this close should merge into a single star in the pre-main-sequence contraction phase (Tohline, 2002). Therefore the pair has to form farther apart and gradually lose angular momentum to reach contact. Contracting orbits could result from a resisting medium but the densities in the interstellar medium are not high enough to cause sufficient angular momentum loss. Schatzman (1962) postulated an efficient mechanism of angular momentum loss for stars with convective envelopes, now called magnetic braking, which seems like the main culprit for systems with component masses below about 1.3 $M_{\odot}$. As discussed in section 2.2.2, the period distribution of contact binary systems is also very interesting. Paczyński *et al.* (2006) analyzed data from the All Sky Automated Survey (ASAS) project and found 11,076 eclipsing binaries in contact, semi-detached and detached states. In a semi-detached binary, one component is in the process of transferring mass to its companion and a detached binary is simply a binary system where no mass transfer is currently taking place. The period distribution of contact binaries shows a peak at 0.37 days (d) and a sharp cut-off at 0.2 d but there are very few detached binaries below 1 d (see Figure 2.10), which is unexpected as the contact configurations are assumed to form from detached binaries with comparable period. Paczyński *et al.* (2006) express our lack of understanding by claiming that the contact binaries seem to appear out of nowhere. Li *et al.* (2007) suggest that this result supports the hypothesis that the contact binaries undergo TRO.

The most promising scenario for the formation of W UMa type binaries and the one that we will assume throughout our discussions is postulated by Stępień (2006). He argues that a contact binary system, in general, is in an advanced evolutionary state and has undergone rapid mass transfer before reversal of the initial ZAMS mass ratio. The evolution of these binaries consists of three phases. The ZAMS progenitor of the system is a close but separated binary with initial total mass of 1.8-2 $M_{\odot}$ and initial period of 2.5-3.1 days. In the first phase, the binary looses angular momentum through magnetic braking. The more massive star eventually runs out of hydrogen in its core and starts to puff up. Phase two begins when this star fills its Roche lobe radius. There is a fast mass transfer event from the more massive star to the less massive one until the equilibrium radius of the initially more massive star becomes smaller than its Roche lobe. This happens after reversal of the mass ratio. The binary spends phase two in this semi-detached, Algol-like state with the initially less massive star now having more mass. In phase three, the now more massive star continues to evolve on a nuclear timescale and the system remains in contact. As we will discuss later, in the particular case of V1309 Sco, the progenitor contact binary system is assumed to develop a tidal instability, called the Darwin (1880) instability, during phase three. This leads to a merger and the observed LRN eruption.

Stępień (2009) gives a hydrodynamic model for large-scale circulations and energy transport in contact binaries. He postulates that energy is transported from the primary to the lower mass component by means of a steadily circulating stream in the equatorial region. This resolves Lucy's paradox and maintains thermal stability of the system. The dynamic stability and exact nature of the heat transfer mechanism has not yet been verified from first principles with models which are fully self-consistent.

The current dissertation attempts to address some of the aforementioned issues with the help of fully three dimensional hydrodynamic simulations. There are two key steps in order to simulate a contact binary system in dynamical equilibrium or a merger scenario. In the first step, we obtain the initial structure of a close binary. In the case of V1309 Sco, it is assumed that the cause of the final eruption is the disruption of the core of the secondary inside the primary star (Tylenda *et al.*, 2011; Stępień, 2011). Hence, we need a core-envelope structure for our stars having two different equations of state, in general. The core is also mostly helium and has a different composition or average molecular weight as compared to the mostly hydrogen envelope. We use a bipolytrope, also known as composite polytrope, to approximate such a star. A polytrope is a stellar model which assumes that the pressure is a function of density, and it is independent of temperature. A bipolytrope is two such polytropes stacked on top of each other, in order to represent a core-envelope structure, for example. The initial model also has to be self-consistent with respect to Poisson's equation and the equations of stellar structure. We build the initial models using a modified version of Hachisu's Self Consistent Field (HSCF) technique (Hachisu, 1986b), which we call the Bipolytropic Self Consistent Field (BSCF) technique. This is an iterative numerical method by which one can determine the equilibrium structure of a synchronously rotating binary system (represented by a barotropic fluid) with unequal masses. The composition difference between the core and the envelope can be mimicked by specifying the jump in the molecular weight in the BSCF method. This method can also produce rapidly rotating single bipolytropic stars, the properties of which have implications for rotating bodies, e.g. magnetic braking of stars and the internal structure of gaseous planets.

In the next step, we study the dynamic evolution of bipolytropic binary systems using hydrodynamic codes. The initial plan was to use the explicit, three dimensional code Flow-ER [Motl *et al.* (2002), D'Souza *et al.* (2006)], which is a finite difference Eulerian code, written in Fortran and parallelized using MPI, implemented in a uniform cylindrical grid. However, a hydrocode which uses a fixed cylindrical grid for evolving a binary has its drawbacks. If a star is not placed at the center, its resolution in the azimuthal direction is very limited. There is also a discontinuity in the density at the core-envelope interface which is hard to preserve with a fixed cylindrical geometry. The numerical methods implemented in a cylindrical geometry cannot preserve steep density gradients near the center of a bipolytropic star. This results in the fall of central densities of the stars on a dynamical timescale, making the interpretation of the results difficult. Dr. Dominic Marcello in our research group has been leading the development of an AMR grid based hydrodynamic code, Octotiger, where these drawbacks can be minimized. This code conserves mass, linear momentum, angular momentum and energy to machine precision (Marcello *et al.* 2017, in preparation). The code is parallelized using a new runtime system called HPX (High Performance ParallaX) which allows the program to scale and perform better than conventional MPI (Message Passing Interface) programming models.

This is the first attempt in the astrophysical community to study the dynamical behavior of binary systems where both components are modeled as bipolytropes. As discussed before, even if the TRO model is assumed, contact binaries are stable over the thermal or Kelvin-Helmholtz time scale. The thermal timescale is of the order 10^7 years for a low mass star, while the dynamical time for the same star is much shorter, of the order of an hour. Our fully 3D hydrodynamic codes are capable of evolving binary systems only on the dynamical timescale, hence the secular behavior

of these systems will not be tested. Using our methods, however, we can study the dynamical properties of close and contact binary systems with the aim of gaining insight into constraining the problem of their stability and structural properties. We can also examine their behavior in dynamical scenarios such as mergers in great detail.

Chapter 2

V1309 Scorpii as a Merger Event of a Contact Binary

2.1 The Luminous Red Nova V1309 Scorpii

The word "nova" means "new" in Latin, implying an appearance of a new star in the sky. When a star in our galaxy is observed to suddenly get brighter by about 9 magnitudes in less than a few days, it is generally classified as a nova. Novae have been studied extensively and are classified into several subtypes such as classical novae, recurrent novae etc. For example, if a white dwarf (WD) accretes mass from its companion, the mass accreted onto the surface of the WD eventually explodes in a thermonuclear runaway process, resulting in a classical nova explosion about $10^4 - 10^5$ times more luminous than the sun. Even though the object gets fainter over the coming months, the observed spectrum shows the hotter layers of the WD's photosphere that are subsequently exposed (Bode & Evans, 1989). On the other hand, an LRN or a V838 Mon type eruption displays some unusual characteristics common to only handful of events. A V838 Mon type event reaches a maximum luminosity of 10^6 $\mathrm{L}_\odot$, which is $10 - 100$ times greater than a classical nova. The object then decreases in brightness, however, instead of getting hotter by exposing inner layers, the erupting object then cools dramatically and the spectrum evolves into one similar to a supergiant star. Additional events in this class include V4332 Sgr, M31RV, M85 OT2006, and, of course, V1309 Sco. In this section we will see how the V1309 Sco LRN was a result of a merging contact binary system.

2.1.1 V1309 Scorpii

V1309 Sco was discovered on September 2^{nd}, 2008 (Nakano *et al.*, 2008) and Mason *et al.* (2010) soon recognized that this was not a typical classical nova. In a little over a month, the spectrum evolved from an early K-type giant to a late M-type star. This means that the temperature of the object decreased from about 5200 K to 4000 K in a few weeks. Other features of V1309 Sco in common with the V838 Mon type eruption are the eruption timescale, outburst amplitude and expansion velocity. The time scale is on the order of months and the outburst amplitude, defined as the magnitude difference between maximum light minus the progenitor's magnitude, is 7 to10 magnitudes. Expansion velocities measured from P-Cygni profiles were a few hundred $\mathrm{km/s}$ as opposed to few thousand km/s in the case of a classical nova.

Located in the direction of the Galactic center, the progenitor of V1309 Sco was situated within the monitoring field of the OGLE III and IV projects. OGLE (Optical Gravitational Lensing Experiment) is a Polish astronomical project based at the University of Warsaw which used the Las Campanas observatory in Chile. The project was mainly concerned with discovering dark matter using gravitational microlensing. Tylenda *et al.* (2011) found that the progenitor of V1309 Sco was observed $\sim$2000 times by OGLE and $\sim$1300 times prior to the eruption. The archival lightcurve is depicted in Figure 2.1. We will discuss the lightcurve in detail in section 2.1.2.

The observed evolution of the basic parameters of V1309 Sco is summarized in Table 2.1. The assumption that the progenitor was a contact binary helps us to calculate other parameters like

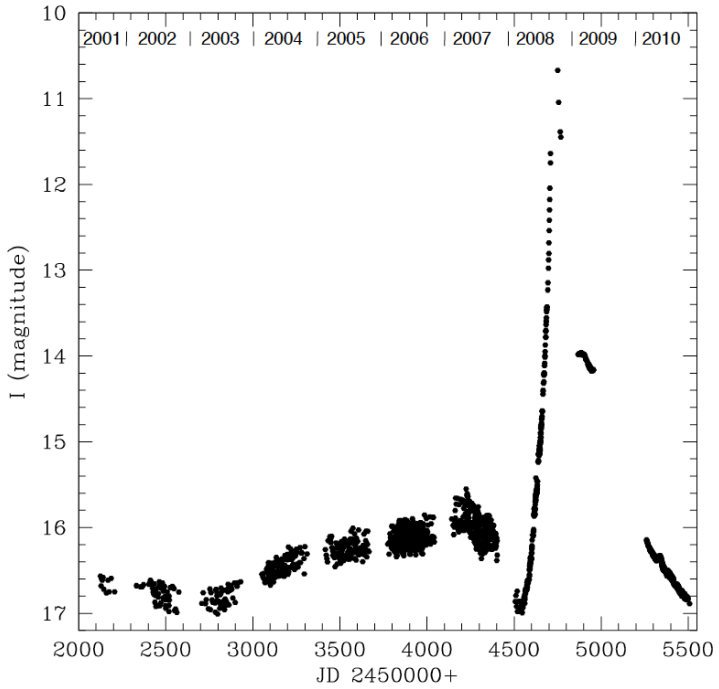

FIGURE 2.1: The light curve of V1309 Sco: I magnitude versus time since Julian Date 2450000 (Tylenda *et al.*, 2011)

effective radius ($R_{\rm eff}/R_{\odot}$) and luminosity ($L_{\rm eff}/L_{\odot}$). Even with the lack of direct spectroscopic observations of the progenitor, Tylenda *et al.* (2011) used typical parameters from other contact binary systems to draw some useful conclusions about the merged object as follows. Assuming a total mass of 1-3 $\rm M_{\odot}$, and a period of 1.43 days, Kepler's law gives us the separation of 5.4-7.7 $\rm R_{\odot}$. Using mass ratio values between 0.07 and 1, which is within the range observed in W UMa systems, we can get radii of the Roche lobes and thus the sizes of individual stars ($\rm R_{eff}/R_{\odot}$). Effective temperature is obtained from a few measurements in the V band before the eruption. Thus from the surface area and effective temperature we can get the luminosity of the pre-outburst object (3.0-8.6 $\rm L_{\odot}$) and hence its distance of 3.5 ± 0.7 kpc.

2.1.2 The Progenitor

Figure 2.1 shows the light curve of the V1309 Sco eruption in the I photometric band. The I band is a standard, well-defined photometric passband with permitted frequencies in the near infrared region. The gaps in the data are because of the conjunction of the progenitor with the sun each year. Notice that the object gradually brightens until about May 2007 and then the magnitude drops significantly before the actual eruption. The data is divided into epochs (starting in 2001), defined as the continuous set of data between these gaps. The epochs are numbered with the last digit of the year of observation. The most significant feature of the progenitor is the ∼0.5 magnitude variations which are periodic (See Figure 2.2). Tylenda *et al.* (2011) used a method employing periodic orthogonal polynomials to fit the period. This method is particularly useful for finding a periodicity in unevenly sampled observations. Their results are summarized in Figure

TABLE 2.1: Observed parameters of V1309 Sco

JD	Data Source	Spec. Type	$T_{\rm eff}$	$R_{\rm eff}/R_\odot$	$L/L_\odot$
4718.9	AAVSO	F9	5830	174.	3.16×10^4
4721.0	AAVSO	G1	5410	177.	2.40×10^4
4722.9	AAVSO	G5	4870	209.	2.22×10^4
4724.9	AAVSO	K1	4360	252.	2.06×10^4
4730.9	AAVSO	K3	4150	297.	2.36×10^4
4735.0	AAVSO	K4	3980	312.	2.21×10^4
4737.9	AAVSO	K5	3900	297.	1.84×10^4
4750.0	AAVSO/ OGLE/ITF	M4	3510	155.	3.27×10^3
4934.8	OGLE	M7	3130	34.	98.5
5282.0	OGLE	M5	3370	9.5	10.4
5437.0	SAAO	M4	3420	6.9	5.9
5474.5	OGLE	M3	3565	5.4	4.2

Basic observed parameters of V1309 Sco in outburst and decline (Tylenda *et al.*, 2011). JD is time in Julian Day, $T_{\rm eff}$ is effective temperature, and $R_{\rm eff}/R_\odot$ and $L/L_\odot$ are radius and luminosity in solar units.

2.3. The solid line is a least squares fit of an exponential formula to the data given by,

$$P(t) = 1.4456 \exp\left(\frac{15.29}{t - t_0}\right) \tag{2.1}$$

where the period (P) is in days, time (t) is in Julian days, and $t_0 = 2455233.5$. The variations start with a period of ∼1.4 day and decrease by 1.2% during the pre outburst observations. This can be interpreted as resulting from an unstable phase of evolution in which the orbit shrinks, ultimately leading to a merger.

Using the period from Equation 2.1, Tylenda *et al.* (2011) folded the observations and obtained light curves for each epoch. The results are displayed in Figure 2.2. One mechanism through which the progenitor system can become unstable is called the Darwin instability. Darwin (1880) showed that in a close binary, if the spin angular momentum of one of the components exceeds $1/3^{\rm rd}$ of the orbital angular momentum, J_{orb}, a small amount of total angular momentum loss can cause the primary component to lose tidal synchronization. As a result, the tidal forces spin up the primary at the cost of J_{orb}, reducing the separation and resulting in an unstable orbit. In Figure 2.2, the light curve starts with equal depth primary and secondary eclipses in the first epoch in 2001. This tells us that both the components had similar temperatures as in a W UMa system. As the progenitor of V1309 Sco gradually evolves, one peak gets significantly brighter than the other. This may be due to the formation of a bright spot formed at the leading edge of the secondary, as it revolves asynchronously in the common envelope (CE). In epoch 7, the smaller peak completely disappears. This indicates that the system evolved into a roughly spherical shape with a bright spot covering a large fraction of the surface. The decline right before the outburst as seen clearly in Figure 2.1 is believed to be due to the formation of dust which obstructs the light. Theories other than a stellar merger, such as pulsation and rotation of a single star, fail

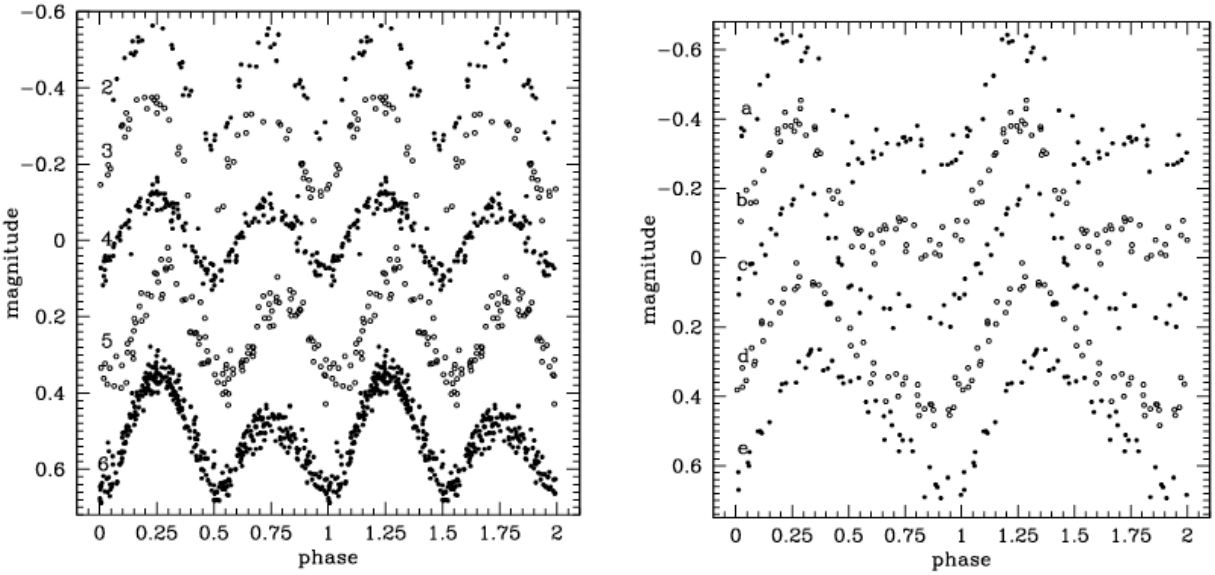

(a) Epochs 2-6

(b) Epoch 7

FIGURE 2.2: The light curves obtained from folding the data with the period given by Equation (2.1). The epoch 7 is divided into five parts. The zero point on magnitude scale is arbitrary (Tylenda *et al.*, 2011) .

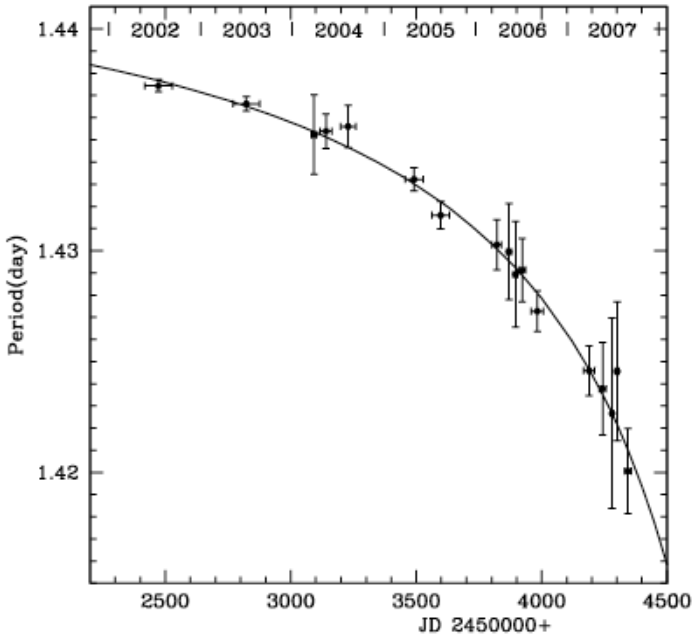

FIGURE 2.3: The evolution of the period of the V1309 Sco progenitor. The solid line shows the least squares fit (Tylenda *et al.*, 2011).

to explain all the observed properties and there is no known mechanism that would produce an eruption of such a magnitude in a single, giant star.

2.2 Contact Binary Systems

In this section we briefly report the observational properties of the W UMa type systems, as well as discuss the current understanding of their internal structure, stability and evolutionary status.

2.2.1 Observed Properties

The first discovered contact binary was found by Müller & Kempf (1903), and they reported it as a variable star with an unusually short period. This was the prototype W Ursae Majoris (W UMa) and the period was about eight hours. The reported period, however, was four hours because the eclipses had equal depths, which is a typical feature of a contact binary light curve, along with continuous light variation. Müller & Kempf (1903) proposed that this could be a system of two celestial bodies almost equal in size and luminosity, whose surfaces are at a slight distance from each other. Figure 2.4 shows the first light curve of W UMa.

An interpretation of the system as a contact binary with components surrounded by a CE was given by Kuiper (1941). Figure 1.1 in the previous chapter shows an artist's conception of an unequal mass contact binary (compare against the last row in Figure 2.5). Although the temperatures of both the components in a contact system are similar, a temperature difference of a few hundred degrees Kelvin is typical (Yakut & Eggleton, 2005). Binnendijk (1970) divided contact binaries into two subtypes, A-type and W-type. In an A-type contact binary the deeper (primary) eclipse corresponds to the occultation of the hotter primary component by the lower mass, secondary component. The components consisting of earlier spectral type, A to G (Bilir *et al.*, 2005), are slightly evolved and near terminal-age main-sequence (TAMS) on the Hertzsprung-Russell (HR) diagram. The total mass of the system is typically more than about 2 $M_{\odot}$. In a W-type contact binary, the primary eclipse corresponds to the occultation of the secondary component, which is hotter. These systems typically possess components with late spectral type (F to K) and are closer to zero-age main-sequence (ZAMS) than the A-type systems. Each component in a contact binary system is nearly the same spectral type. The periods of contact binaries are typically short, between 0.25 and 1 d. Eggen (1967) discovered that the color or the spectral type of W UMa type systems is related to the orbital period, with shorter period systems being redder.

In order to understand and further discuss the nature of a contact binary system, we need to consider the effective potential of a gravitationally bound binary system, also called the Roche potential (Φ_R). The Roche potential of a binary is viewed from a non-inertial frame of reference rotating with the same frequency as the system's orbital angular velocity. The binary components are approximated by point masses and revolve around the common center of mass (CoM) in circular orbits. The Roche potential is given by,

$$\Phi_{\mathbf{R}}(\boldsymbol{r}) = -\frac{\mathrm{GM}_1}{|\boldsymbol{r}-\boldsymbol{r}_1|} - \frac{\mathrm{GM}_2}{|\boldsymbol{r}-\boldsymbol{r}_2|} - \frac{1}{2}\Omega^2\boldsymbol{d}^2 \tag{2.2}$$

where $\boldsymbol{r}_1$ and $\boldsymbol{r}_2$ are position vectors and M_1 and M_2 are the masses of the two stars, Ω is the orbital angular velocity of the system, $\boldsymbol{d}$ is the distance from the axis of rotation and G is the gravitational constant. Figure 2.6 gives the shape of the Roche potential in the equatorial plane.

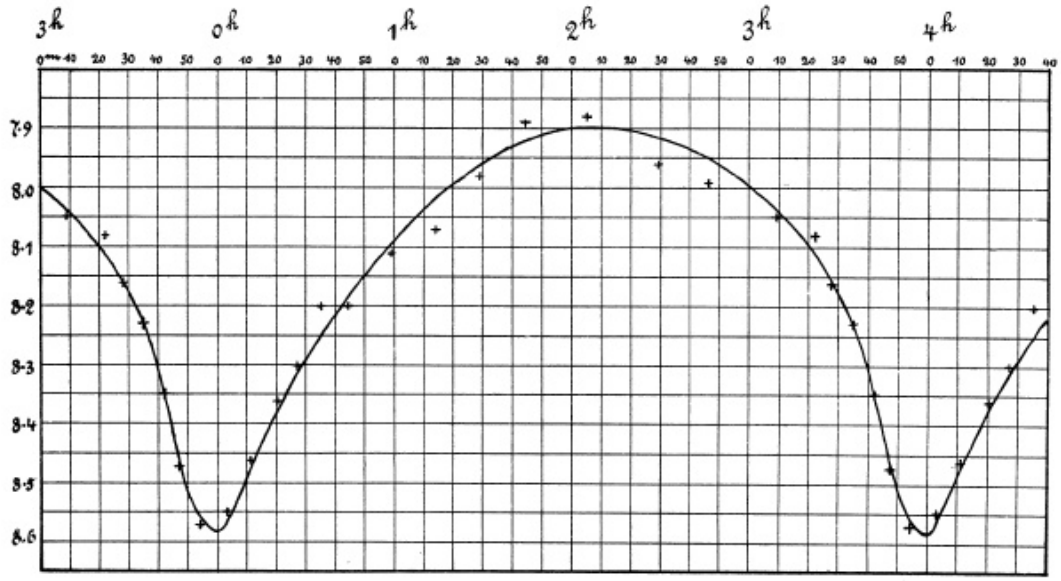

FIGURE 2.4: Early light curve of W Ursae Majoris (Müller & Kempf, 1903).

The surface inside which an orbiting body or the stellar material is gravitationally bound to only one of the stars is known as the Roche lobe. This is an equipotential surface with two teardrop shaped lobes in three dimensions. There are five points of interest in this potential, called Lagrange points, denoted by L_1- L_5. The point of intersection of the two Roche lobes is called the inner Lagrange point (L_1). The L_1 point is a saddle point in the potential. Matter at this point is equally bound to both stars. If either of the stars grows larger than its Roche lobe, then this star will begin to transfer mass to its companion through the L_1 point. The second Lagrange point (L_2) is located beyond the smaller mass along the line joining the center of masses of the two components, where the gravitational force due to the masses is cancelled by the centrifugal force. An analogous point located near the larger mass is called the L_3 point. The equipotential surface with the same potential as L_1 is called the inner equipotential surface (or contact surface), and that with the same potential as L_2 is called the outer equipotential surface. The final two Lagrange points, L_4 and L_5, form an equilateral triangle with the two stars as the base, in the plane of the orbit. These points are the locations of the maximum potential as depicted in Figure 2.6. The precise shape of the Roche lobe depends on the mass ratio, separation, and in the case of real stars, the mass distribution. Note that there is no analytical solution for the potential when the masses involved are not point sources but extended fluid bodies. However, the general structure of the Roche geometry remains similar.

Inner and outer contact surfaces for different mass ratios are demonstrated in Figure 2.5 (Kuiper, 1941). If neither of the stars fill its Roche lobe, the system is a detached binary. If one of the companions fills its Roche lobe, the system is called semi-detached. In a semi-detached binary, the Roche lobe filling star transfers matter onto the other through the L_1 point. The star filling its Roche lobe is called the donor and the one gaining the material is called the accretor. Here the mass ratio is defined as the ratio of the mass of the donor to that of the accretor. Finally, if both stars fill their Roche lobes, the system forms a contact binary. We will call the

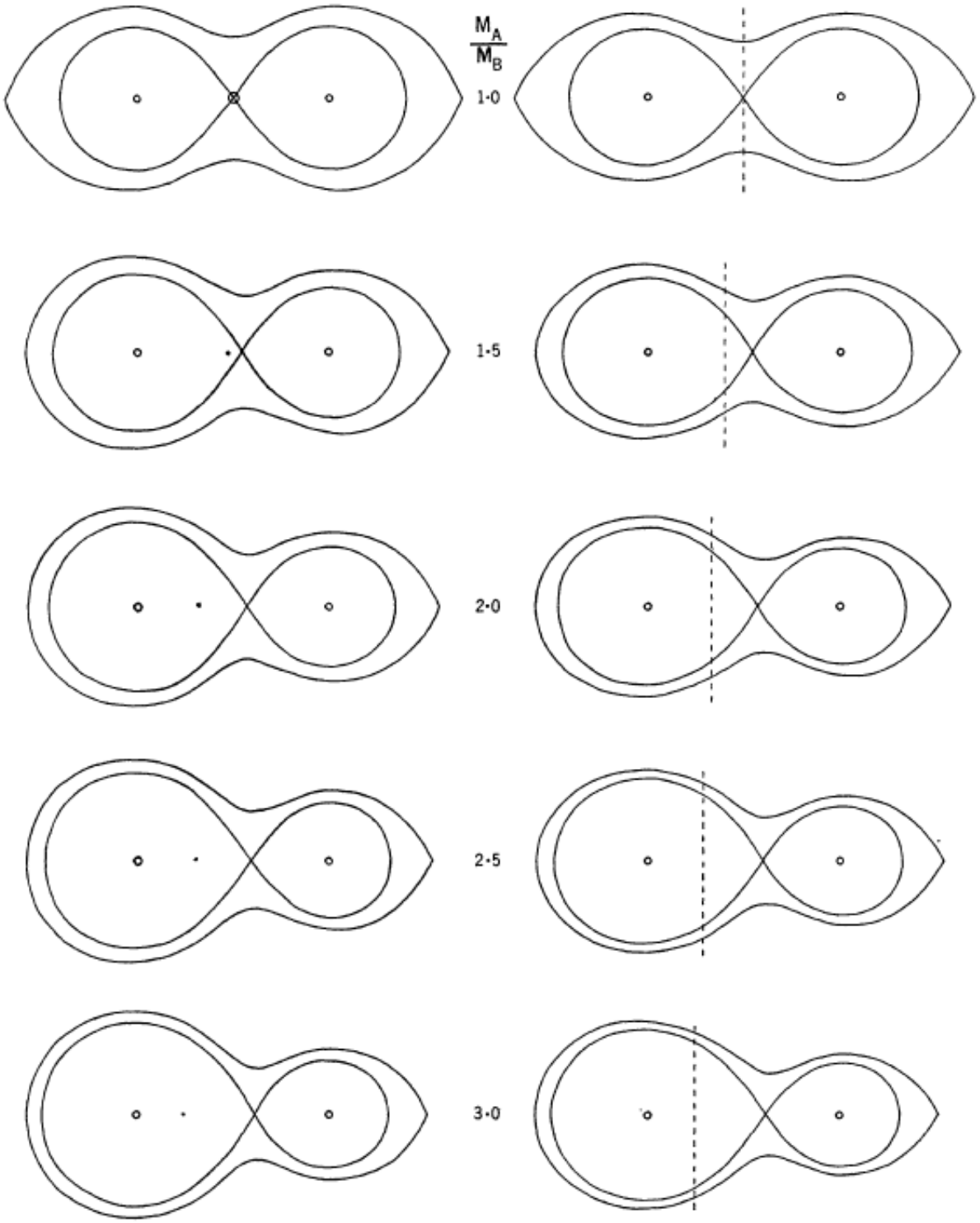

FIGURE 2.5: Inner and outer contact surfaces for binaries with different mass ratios. Figures in the left column show equatorial cross sections and figures in the right one show vertical cross sections with the dashed line as axis of rotation (Kuiper, 1941). Here $\frac{M_A}{M_B}$ is the ratio of the mass of the primary to that of the secondary, which is the inverse of the mass ratio.

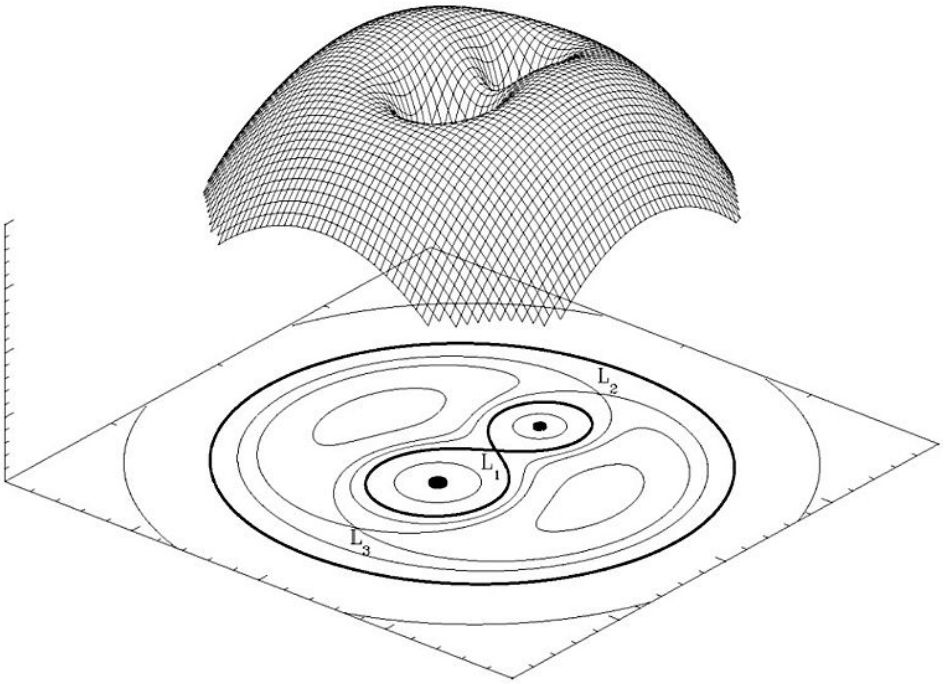

FIGURE 2.6: A surface contour plot of the Roche potential in the equatorial plane of a binary with a mass ratio 0.5 (van der Sluys, 2006).

more massive star the primary, and the other star the secondary. The mass ratio in this case is conventionally the ratio of the mass of the secondary to that of the primary, hence it is always less than unity. In a contact binary, both the components are at least touching at the L_1 point. The stellar surfaces lie between the inner and the outer critical equipotential surfaces. The stars are said to be surrounded by a common envelope (CE) lying between these two surfaces. The system rotates synchronously, meaning that the same side of one component always faces the other component, due to tidal locking. If the stars overflow the outer critical surface, mass is lost through the L_2 point. For binary systems which don't have a CE, the Roche lobe filling factor (Rlff) of a component is defined as the ratio of the volume of the star to the volume of its Roche lobe. The Rlff is useful in describing the proximity of a binary component to mass transfer, as at its maximum value of unity, the corresponding component fills its Roche lobe and can start transferring material to its companion through L_1. In a close binary, one or both the stars can significantly deviate from a spherical geometry and conform to an elongated equipotential surface. The stellar radius (R) is then defined as the radius of a sphere having the same volume as occupied by the star. The radius of the Roche lobe is defined in a similar way, in terms of the equivalent volume. An approximate analytic formula for the Roche lobe radius is given by Eggleton (1983) as

$$\frac{R_L}{a} = \frac{0.49q^{2/3}}{0.6q^{2/3} + ln(1 + q^{\ 1/3})} \tag{2.3}$$

where R_L is the Roche lobe radius of the primary, a is the separation. In a contact configuration, it is difficult to distinguish between the two stars for the purpose of calculating the masses and

radii. In this case the stars are separated by means of an imaginary plane at the L_1 point, normal to the line joining the CoM of the two stars. The knowledge of Roche geometry is essential for understanding the properties and behavior of close and contact binary systems, as we shall see throughout this study.

The contact binaries show a seemingly contradictory property. Kuiper (1941) pointed out that the surface of a contact binary must lie between the inner and outer critical Roche surfaces as depicted in Figure 2.5. The corresponding value for the stellar radius of both the components in a contact binary approximately equals the Roche radius, satisfying a relation $R_L \propto M^{0.46}$. The main-sequence mass-radius relation of an isolated star, however, is approximately given by $R \propto M^{0.57}$ for high mass stars and $R \propto M^{0.8}$ for low-mass stars (Kippenhahn & Weigert, 1994). Thus the two mass-radius conditions that the components have to satisfy are not compatible unless the mass ratio is unity. W UMa systems show a mass ratio less than unity and close to 0.5 (Binnendijk, 1970). This lowest order phenomenon concerning the structure of the contact binary systems is known as Kuiper's paradox (Kuiper, 1941).

As mentioned earlier, the temperatures of both the components in a W UMa type binary are nearly equal, despite the two components having potentially widely different masses. This implies that the components violate the ZAMS mass-luminosity relation, $L \propto M^{3.2}$ (Kippenhahn & Weigert, 1994). Osaki (1965) first proposed the idea of a CE surrounding the two stars which redistributes the luminosity coming out of the stellar interiors. Contact binary systems also often show maxima with unequal heights, with the more luminous maximum following the deeper primary eclipse. This phenomenon is known as the O'Connell (1951) effect and presumably the result of some kind of stream structure flowing between the two components. The implications of these observations on the internal structure of contact binaries are discussed in the next section.

2.2.2 Structure and Evolutionary Status

There are two contending theories for explaining the observed properties of contact binary systems. Shu *et al.* (1976b) advanced the discontinuity theory (DSC) in a series of four papers while Lucy (1976) proposed the thermal relaxation oscillation (TRO) theory. This section briefly describes both these theories, along with current understanding about the evolutionary status of contact binary systems.

DSC theory:
Shu *et al.* (1976b) state that the Kuiper paradox arises because of the competition between the mechanical requirements (Roche radii) and thermal requirements (ZAMS radii) of the contact binary system. They propose a resolution to this problem as follows. The dynamic timescale of a star, defined as the "free fall" time without any pressure support, is given by

$$T_{dyn} = \left(\frac{R^3}{2GM}\right)^{1/2}. \tag{2.4}$$

The thermal timescale, also known as Kelvin-Helmholtz timescale, is defined as the time required to radiate the total gravitational energy of a star at current luminosity. Hence

$$T_{KH} = \frac{GM^2}{LR}. \tag{2.5}$$

The thermal timescale is at least three orders of magnitude larger than the dynamical timescale of a star. Since the two cores of a contact binary produce different intrinsic luminosities, fluid must flow in order to compensate for the uneven distribution of the sources of heat. As the dynamic timescale is several orders of magnitude smaller than the thermal timescale, even small flows can redistribute the heat effectively. Above the Roche lobe, the horizontal redistribution of material is possible in a much more efficient way, as it is bound to both the stars. This is because the gas moving from one star to the other does not have to do work against gravity. Below the Roche lobes, such horizontal redistribution is hindered by the self gravity of the star, thus there can be a discontinuity at the Roche surface. This discontinuity exists only in the secondary, where the pressure is continuous but the density and temperature (or their gradients) are not. In the case of convective envelopes, the discontinuity is maintained against thermal diffusion by assuming that the CE has the same specific entropy as the primary envelope. This makes the CE more buoyant than the secondary material just below the Roche lobe. Since the secondary does not have a direct outlet for the luminosity coming from the core, its material expands at constant volume and spills inside the primary through the L_1 point. This mass loss is balanced by the circulation currents in the secondary CE, which deposit the same amount of material. Thus the CE is mechanically coupled to the primary. A similar discontinuity is proposed for stars with radiative envelopes, however, the primary also exhibits a "weak" contact discontinuity, where only the gradients of density and pressure are discontinuous. This forms the basis of the DSC theory, explaining several observed properties.

Stępień (2009) suggested a semi-analytical hydrodynamic model for the energy transport between the components of a low-mass contact binary. Due to the non-uniform heating of the base of the CE, it must be treated as baroclinic rather than barotropic. A barotropic fluid is one in which the pressure depends only on the density and vice versa. In other words, isobaric (constant pressure) surfaces are isopycnic (constant density) surfaces. But in a baroclinic fluid, isobaric and isopycnic surfaces cross each other, creating a misalignment in their respective gradients. A different vertical (i.e., normal to the surface) pressure stratification in the components produces a horizontal pressure gradient. This gradient in pressure drives mass on a dynamical time scale and creates large-scale circulation flows. In the absence of the Coriolis force, the resulting large-scale flows are symmetric around the axis joining the center of the two stars. However, the Coriolis force cannot be neglected for a flow velocity which is a significant fraction of the sound speed. Since the Coriolis force is given by $-2m\mathbf{\Omega} \times \mathbf{v}$, for a surface flow in the northern hemisphere, the Coriolis force always deflects it towards the right and for a flow in the southern hemisphere, it deflects the flow towards the left of the velocity direction. For a flow which moves from the primary to the secondary on the surface, this force confines the motion in a narrow stream going around the secondary in the equatorial plane. The resulting geometry of the flow in the CE is depicted in Figure 2.7. This stream is assumed to be isolated from the convective envelope of the secondary by means of a radiative transition layer, which acts as an insulator.

Thermal energy is carried to the secondary through the equatorial flow, so there is a significant change in the apparent surface brightness of the contact binary system. This stream around the secondary acts like a hot blanket covering the surface, hindering the normal outward energy flow from the core. This reduction of the radiative surface is compensated for by an increase in surface temperature of the undisturbed part of the secondary. The primary suffers an additional cooling

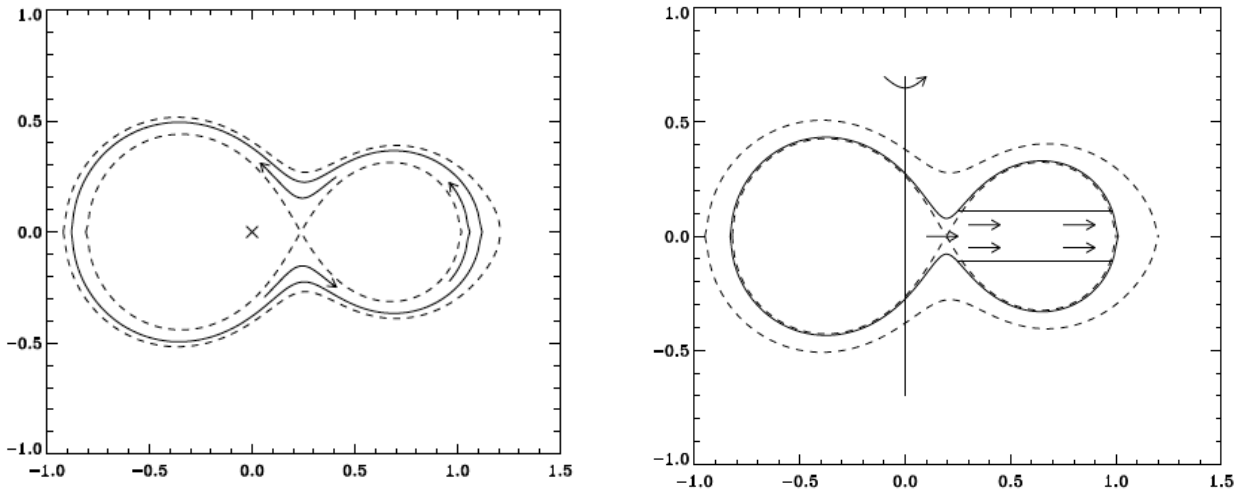

(a) Top-down view

(b) Side view

FIGURE 2.7: The geometry of a contact binary in the equatorial plane and the equatorial stream structure (Stępień, 2009).

due to the stream, which encircles the secondary and feeds low entropy matter to the primary. Because of its low entropy the stream does not fully encircle the primary, and instead disappears in its convective zone. This stream is the reason that both the components show approximately the same temperature as deduced from the light curve. This stream structure also explains the aforementioned O'Connell (1951) effect, since the deeper, primary eclipse will be followed by the hotter side of the stream. The W-type phenomenon where the smaller component displays higher temperature, is not explained by energy transfer alone, as energy cannot be transferred from cooler to hotter components in an isolated system. The most common explanation of W-type phenomena assumes that dark, cool spots cover a substantial fraction of the primary's surface (Rucinski, 1993). Hence, the average apparent temperature is lower than the secondary. W UMa type stars do show very high chromospheric coronal activity (Stępień *et al.*, 2001).

TRO theory:
Lucy (1976) argues that W UMa type systems undergo thermal relaxation oscillations about a quasi-equilibrium state of marginal contact. The motivation comes from the inability of the DSC theory to naturally explain W-type contact binaries which form about half of the contact systems. The DSC theory also struggles to fit asymmetric and aperiodic behavior observed in many of the light curves (Mochnacki & Doughty, 1972; Ruciński, 1973).

Lucy (1976) suggests that for the equal entropy conditions to be valid, the internal adiabatic constants need to be equal for a contact binary, hence for $q \neq 1$, there are no static equilibrium solutions. Consider a recently formed contact binary system which has achieved mechanical equilibrium but not thermal equilibrium. As mentioned earlier, the contact binary components need to have radii almost equal to their corresponding Roche lobe radii. If we assume that the thermal equilibrium in the primary is maintained, the secondary must be compressed in order to reach a radius equal to that of its Roche lobe. This compression of the secondary is indicated by segment B$\rightarrow$B' as it moves from its ZAMS radius to its Roche lobe radius in Figure 2.8. Now consider

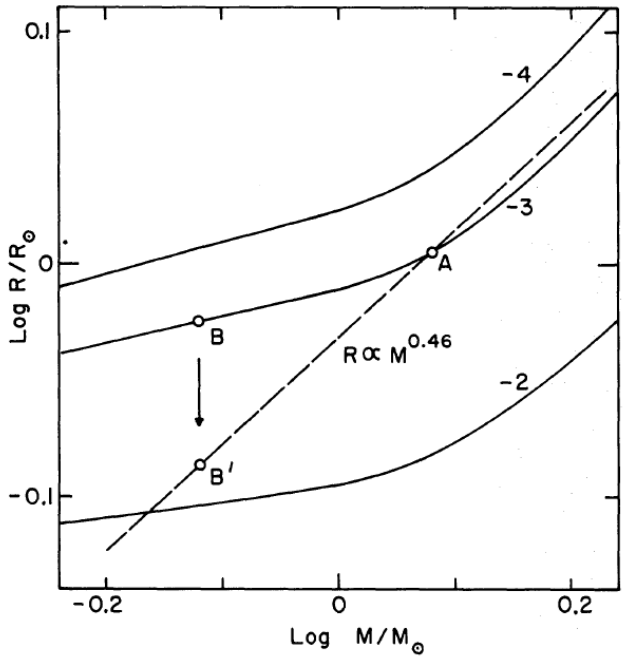

FIGURE 2.8: Mass-radius relation for the Roche lobes (dashed line) and three different values of the adiabatic constants, K (solid lines). The numerical values are log K. A denotes position of the primary and B→B' denotes the migration of the secondary after contact (Lucy, 1976).

the secular evolution of this system. As the secondary is compressed in order to achieve thermal equilibrium, the nuclear energy generation rate increases in its core. This will cause the secondary to slowly expand on a thermal time scale. The deviation from the Roche lobe, however, proceeds on a dynamical time scale and the expansion will result in mass transfer to the primary. Figure 2.8 shows that a small amount of mass loss will not bring the binary into thermal equilibrium, so the mass loss will continue from the secondary to primary. Assuming there is no net mass or angular momentum loss from the system during this time, the mass transfer from a low mass star to a high mass star will cause the separation to increase and the binary will eventually break contact. Thus a newly formed contact binary evolves towards a state of marginal contact.

Once contact is broken, however, the condition for equal entropy or an equal adiabatic constant is no longer valid and the two components will evolve as two separate stars. Figure 2.9 depicts this situation for the two components with respect to the equilibrium ZAMS radii. The ZAMS radius for the primary is greater than the Roche radius and the opposite is true for the secondary. According to Lucy (1976) this is true for a certain domain in the (total mass, total angular momentum, mass ratio)-space. At this point, the primary will try to reach the ZAMS radius by expanding on KH timescale and in compliance with the Roche geometry transfer material to the secondary. The secondary, on the other hand would contract after separation. The mass transfer from the more massive component will drive the binary back into contact and the cycle will repeat. A semi-detached binary which has separated from being in contact will have different surface temperatures, since the stars are no longer thermally coupled, but roughly the same geometry.

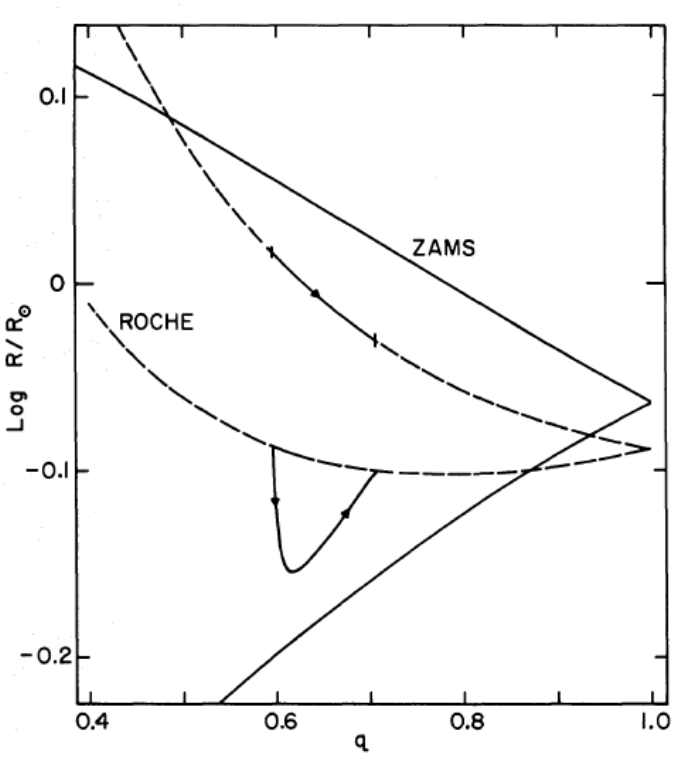

FIGURE 2.9: The solid lines with arrows show the evolution of the binary after loss of contact. Roche lobe radii (dashed) and ZAMS radii (solid) are plotted for both components. After the contact is lost, mass transfer from primary to secondary will cause evolution from left to right (Lucy, 1976).

Shu (1980) proposes that although superficially different, the DSC and TRO theories can be complimentary. In the DSC theory, the assumption is that the discontinuity is secularly stable, while TRO theory relies upon the unproven assumption of a complete oscillation cycle. The two theories are compatible in the sense that even if TRO cycles take place in contact binary systems, the discontinuity has to ensue in the contact phase. Recent statistics of the observed period distribution qualitatively confirm the TRO theory. In TRO theory, the radii of the two components change relatively little so the effects on the light curve due to the geometry remain almost the same as a contact system. The relative depth of the minima changes significantly depending on whether the system is actually in contact or not. Thus this theory requires that semi-detached binaries with a period between 0.2 to 1.3 days are common. Paczyński *et al.* (2006) examined the eclipsing binary distribution from ASAS data. Based on the distribution of close binaries, Figure 2.10, they found that there is no shortage of short period close binaries. The traditional view on the evolution of contact binaries is that they come from detached binaries of comparable period because of angular momentum loss via mechanisms such as magnetic braking. However, the distribution shows very few detached binaries below a period of 1 day, which is surprising.

The Kozai-Lidov mechanism (Kozai (1962), Lidov (1962)) operates in a three body hierarchical system such that periodic changes between the eccentricity and inclination of a binary are caused by the third body revolving on a much wider orbit. Pribulla & Rucinski (2006) showed that up to

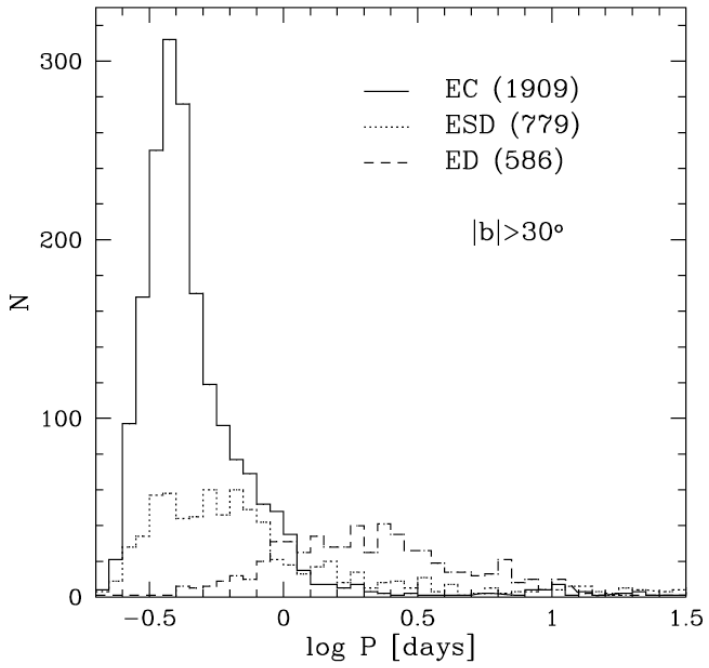

FIGURE 2.10: Period distribution of eclipsing binaries discovered by All Sky Automated Survey (Rucinski, 2006). EC, ED and ESD stands for eclipsing contact, detached and semi-detached binaries respectively.

half of the contact binary systems have a companion. This finding along with the relative scarcity of detached binaries with periods shorter than 1 d suggests that Kozai-Lidov mechanism may be an important channel for forming contact binary systems. Stępień (2006) argues that the basic assumption in the Lucy (1976) model that both the components in a contact binary system are on the main sequence is false. A young ZAMS binary formed from a protostellar cloud can have the shortest period of about 2 d, which is much larger than required to form a contact configuration (Stępień, 1995). As described in section 4.3.2, lower mass stars with convective envelopes can lose angular momentum through magnetic braking. This mechanism takes several GYr, which is of the order of the nuclear timescale, to form a contact system from an initial period of 2 days. W UMa type systems are rare in young clusters but much more common in open clusters older than $5-6$ GYr and in globular clusters (Rucinski, 1998, 2000). Stępień (2006) concludes that the components of a contact binary are not on the ZAMS. A typical W UMa type system is formed after the first episode of mass exchange on the KH timescale and mass ratio reversal. The initial primary is now the secondary and is past its TAMS. The secondary now has a helium core, while the primary is a weakly evolved main sequence star. We will choose the internal structures of the components for the bipolytropic binary simulations assuming this final scenario to be valid in Chapter 6.

Chapter 3

Theoretical Background for Bipolytropes and Mass Transfer

This chapter describes the polytropic approximation that is used in order to represent the equation of state (EoS) of the gas inside stars. Bipolytropes, also known as composite polytropes, are used to approximate the core-envelope structure. The last subsection describes the general, semi-analytical properties and expected behavior of binary systems which are close enough to interact and transfer material.

3.1 Polytropes

Consider the structure of a single, non-rotating star in equilibrium. The equations that describe the stellar structure are as follows (see for example Padmanabhan (2001)). The mass continuity equation is

$$\frac{\mathrm{d}M_r(r)}{dr} = 4\pi r^2 \rho(r) \tag{3.1}$$

where M_r is the mass enclosed in the radius, r, of the star. The equation of hydrostatic balance can be written as

$$\frac{\mathrm{d}P(r)}{\mathrm{d}r} = -\frac{GM_r(r)}{r^2}\rho(r), \tag{3.2}$$

where P is the pressure. Depending on the dominant mechanism of energy transport, the thermal equation can be written as

$$\frac{\mathrm{d}T(r)}{\mathrm{d}r} = -\frac{3\kappa}{4ac}\frac{\rho(r)}{T^3}\frac{L(r)}{4\pi r^2}, \tag{3.3}$$

or

$$\frac{\mathrm{d}T(r)}{\mathrm{d}r} = -\nabla_{ad}\frac{\rho(r)T(r)}{P(r)}\frac{GM_r}{r^2} \tag{3.4}$$

for radiative and convective transfer respectively. Here T is the temperature, L is the luminosity, κ is the opacity, a is the radiation constant and c is the speed of light. The adiabatic temperature gradient, ∇_{ad}, is defined as $\nabla_{ad} = (\partial \ln T/\partial \ln P)_s$, at constant entropy, s . Lastly, the equation for energy production is

$$\frac{\mathrm{d}L(r)}{\mathrm{d}r} = 4\pi r^2 \rho(r)\epsilon, \tag{3.5}$$

where ϵ is the energy generation rate These form a set of four differential equations in five variables - $M_r(r), \rho(r), P(r), T(r)$ and $L(r)$. In order to close the system we need one more equation, which is the equation of state

$$P = \frac{\Re}{\mu}\rho T + P_e + \frac{1}{3}aT^4, \tag{3.6}$$

where $\Re$ is the universal gas constant, μ is the mean molecular weight and P_e is the electron degeneracy pressure. For the four differential equations, the boundary conditions are

$$M_r = 0,\ L = 0 \qquad \text{at} \qquad r = 0, \tag{3.7}$$

$$\rho = 0,\ P = 0 \qquad \text{at} \qquad r = R. \tag{3.8}$$

The opacity and the energy generation rate are not constant throughout the star but depend on the microphysics and their calculation is a vast topic in itself. In general, both κ and ϵ are functions of temperature and density, i.e.

$$\kappa = \kappa(\rho, T) \qquad \text{and} \qquad \epsilon = \epsilon(\rho, T). \tag{3.9}$$

In the end, we get a system with four first order differential equations (Equations 3.1-3.5) and three auxiliary equations (Equations 3.6 and 3.9, the latter denotes two equations) in seven variables (r, ρ, L, P, T, κ, ϵ) with four boundary conditions specified at two different points (Equations 3.7-3.8). There is no general method of solving such a system of coupled equations in closed form without making restrictive assumptions. Hence we need to rely on numerical integration in order to solve them.

The equations of stellar structure fall naturally into two categories, one describing the mechanical structure of the star and the other describing thermal structure. These are coupled only through the temperature dependance of the EoS. If the EoS is imposed beforehand with the complete set of equations of stellar structure, this could give rise to a conflict such that a self consistent model would not be possible (Hansen *et al.*, 2004). Polytropes are stellar models, which assume a power law relationship between pressure and density, which must hold true throughout the star (Chandrasekhar, 1939). This relation is assumed a priori, however, no reference to heat transfer or thermal balance is made. Thus only the mass continuity equation (Equation 3.1) and the hydrostatic equation (Equation 3.2) are used, and inconsistencies with the complete set of stellar structure equations are avoided. Since there are three unknowns, pressure, density and mass as a function of radius, these two equations, along with the EoS are sufficient to obtain a solution.

In a polytropic stellar model, the pressure is given by,

$$P(r) = K\rho(r)^{1+1/\mathrm{n}} = K\rho^{\gamma} \tag{3.10}$$

where n is called the polytropic index, K is polytropic constant. The equation of hydrostatic equilibrium (Equation 3.2) in Lagrangian form is

$$\frac{\mathrm{d}P}{\mathrm{d}M_r} = -\frac{GM_r}{4\pi r^4}. \tag{3.11}$$

Combining this with the continuity equation we get,

$$\frac{1}{r^2}\frac{\mathrm{d}}{\mathrm{d}r}\left(\frac{r^2}{\rho}\frac{\mathrm{d}P}{\mathrm{d}r}\right) = -4\pi G\rho. \tag{3.12}$$

The dimensionless variable θ is defined as

$$\rho = \rho_c\theta^{\mathrm{n}}, \tag{3.13}$$

where ρ_c is the central density. After rescaling r with a new dimensionless variable ξ such that $r = r_n\xi$, we get the famous Lane-Emden equation (Lane, 1870; Emden, 1907)

$$\frac{1}{\xi^2}\frac{d}{d\xi}\left(\xi^2\frac{\mathrm{d}\theta}{\mathrm{d}\xi}\right) = -\theta^{\mathrm{n}} \tag{3.14}$$

where

$$r_n^2 = \frac{(n+1)P_c}{4\pi G\rho_c^2}$$

and P_c is the central pressure. The boundary conditions applied to a polytropic model, analogous to Equations 3.7 and 3.8, are at the center,

$$\theta(0) = 1, \quad \theta'(0) = 0 \qquad \text{at } \xi = 0. \tag{3.15}$$

The surface of the polytrope is located at $\xi = \xi_1$, when $\theta(\xi_1) = 0$. The radius of the polytrope is

$$R = r_n\xi_1 = \frac{(n+1)P_c}{4\pi G\rho_c^2}\xi_1 \tag{3.16}$$

and the total mass can be derived as

$$M = -4\pi\left(\frac{K}{\pi G}\right)^{3/2}\left(\xi^2\frac{\mathrm{d}\theta}{\mathrm{d}\xi}\right)_{\xi_1}. \tag{3.17}$$

In general, the Lane-Emden equation must be solved numerically. The $n = 0$ polytrope corresponds to a constant density sphere and the other analytical solutions exist for $n = 1$ and 5. The solutions with $n \geq 5$ contain infinite mass, hence the range of interest for a complete model is $0 < n < 5$. Although higher polytropic indices may be useful for a truncated or composite polytrope. Figure 3.1 demonstrates the steepening of the density profile with the increase in the polytropic index.

The different states of gas that can be approximated by ploytropes in a stellar context are listed in Table 3.1. Polytropes are a reasonable approximation to represent gaseous planets, main sequence stars, fully convective stars and even compact objects like white dwarfs and neutron stars. The polytropic representation works because in stellar interior, apparent decoupling of temperature and pressure often takes place in certain regimes. As an example, Figure 3.2 compares the numerical solutions of the internal density, pressure and temperature profiles of the standard solar model to an $n = 3$ polytrope. The agreement is reasonable and the largest deviation is in the outer regions where convection plays a significant role. This deviation is also caused largely by the fact that the entropy is not constant throughout a real star. However, the polytropic constant, which is related to the entropy, is assumed constant for a polytropic model.

TABLE 3.1: Polytropes representing different EoS

Description of Gas	EoS	Polytropic Index
Fully convective	$P \propto \rho^{5/3}$	$n = 3/2$
Degenerate non-relativistic	$P \propto \rho^{5/3}$	$n = 3/2$
Degenerate relativistic	$P \propto \rho^{4/3}$	$n = 3$
Fully radiative	$P \propto \rho^{4/3}$	$n = 3$
Magnetic field dominated	$P \propto \rho^{4/3}$	$n = 3$
Isothermal	$P \propto \rho$	$n = \infty$

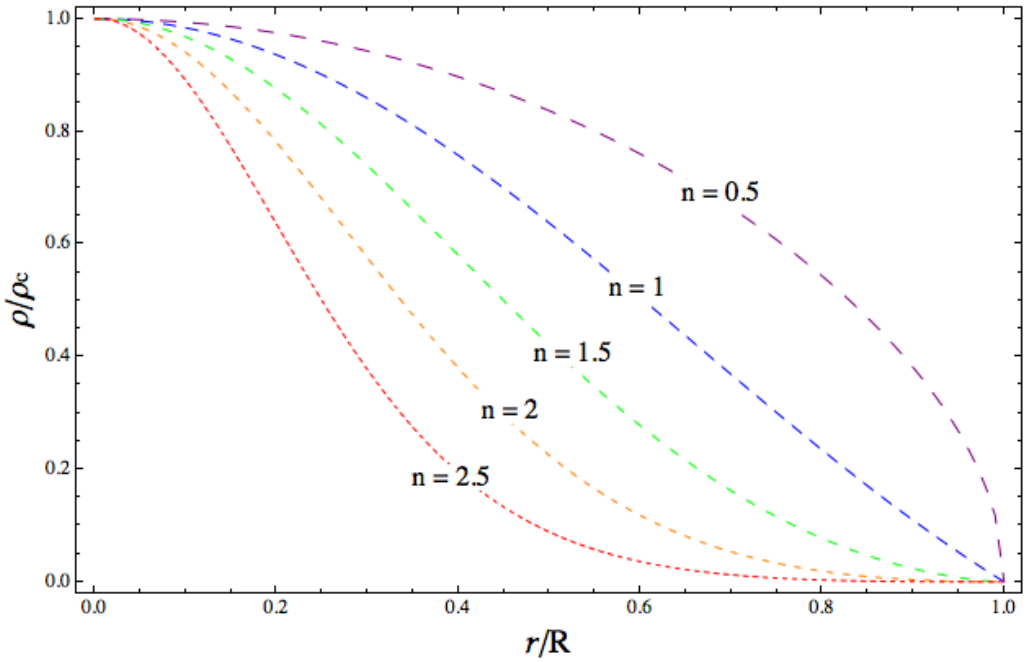

FIGURE 3.1: The density profiles of spherical polytropes with different polytropic indices.

3.2 Bipolytropes

Stellar models which use a polytropic EoS give us a reasonable understanding of the interiors of stars. However, for stars which have a distinct core and envelope structure, especially if centrally condensed, the polytropic model starts to break down. These stars with a well defined core behave in fundamentally different ways and we need a core-envelope structure in order to represent them faithfully. The core can affect the structural properties of more evolved stars such as TAMS, subgiant, red giant and asymptotic giant branch (AGB) stars. Even on the main sequence, low-mass stars (below 1.5 $M_{\odot}$) possess a radiative core and convective envelope and high-mass stars have a convective core and a radiative envelope (Padmanabhan, 2001).

One way to achieve a better approximation is to use bipolytropes, sometimes also referred to as composite polytropes, where the core and the envelope of a star are allowed to have different polytropic indices. This idea was first proposed by Milne (1930) who suggested that the temperature, pressure and mass enclosed would be continuous at the core-envelope interface. Henrich & Chandrasekhar (1941) implemented this condition for a star with an isothermal core and polytropic envelope to infer an upper limit in the core mass fraction. Schönberg & Chandrasekhar (1942) introduced a discontinuous jump in the molecular weight at the core-envelope boundary to deduce the Schönberg-Chandrasekhar (SC) limit. As described in section 3.1, analytical solutions of single polytropic spheres are possible only in the cases where the polytropic index, n, equals zero (constant density), one or five, and only in the non-rotating and spherically symmetric scenario. Analytical solutions for bipolytropes are thus possible only for certain combinations of these three indices (Murphy, 1983; Eggleton *et al.*, 1998).

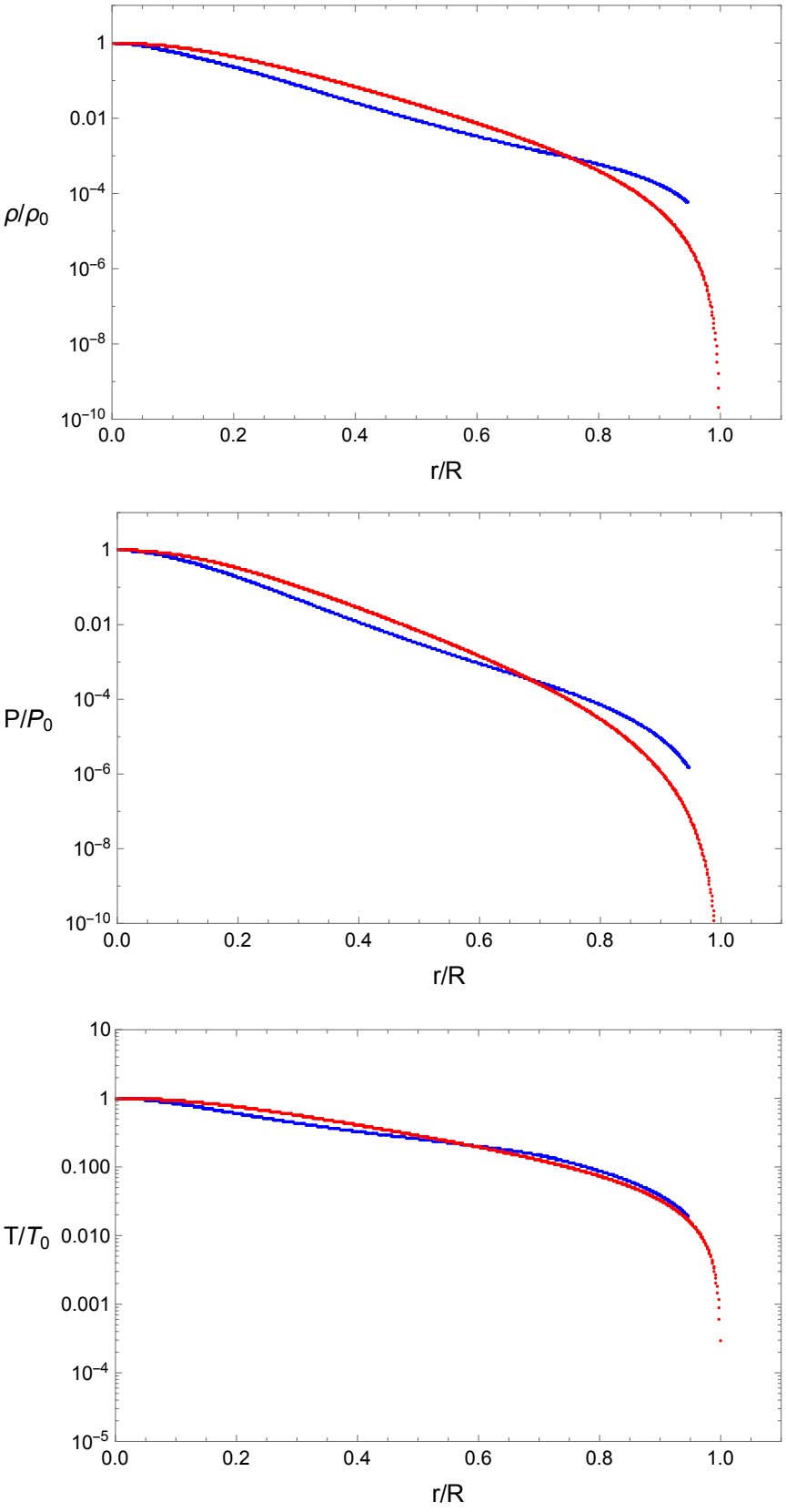

FIGURE 3.2: The density, pressure and temperature profile of the standard solar model (blue) (Bahcall *et al.*, 1995) compared with an $n = 3$ polytrope (red).

A bipolytropic star has one polytropic index for the core ($n_{\rm c}$) and one for the envelope ($n_{\rm e}$), as depicted in Figure 3.3. The subscripts $\rm c$ and $\rm e$ correspond to the core and the envelope, and the subscript $\rm i$ corresponds to the core-envelope interface throughout this dissertation. In general, the polytropic constant is also different for the two regions. The physical quantities which are continuous across the core-envelope interface are pressure, temperature and the mass enclosed. While the pressure in the core and the envelope are represented by the respective polytropic EoS, at any point the total pressure must also be given by the sum of gas pressure and radiation pressure. Hence

$$P = \frac{\rm k_B}{\mu \rm m_H}\rho T + \frac{1}{3}\rm a T^4 \tag{3.18}$$

where $\rm k_B$ is the Boltzmann constant and $\rm m_H$ is the mass of the hydrogen atom. For an evolved star the core composition is different from that of the envelope, hence they have different molecular weights. Since the temperature and pressure are continuous across the boundary, the density across this interface is not continuous, but the jump at the contact discontinuity is proportional to the ratio of molecular weights,

$$\frac{\rho_{\rm ci}}{\rho_{\rm ei}} = \frac{\mu_{\rm c}}{\mu_{\rm e}} \tag{3.19}$$

where $\rho_{\rm ci}$, $\rho_{\rm ei}$ are densities at the interface on the core and envelope side and $\mu_{\rm c}$ and $\mu_{\rm e}$ are the mean molecular weights. These are the boundary conditions at the core-envelope interface of a bipolytrope. The ratio of molecular weights,

$$\alpha = \frac{\mu_{\rm c}}{\mu_{\rm e}} \tag{3.20}$$

represents the discontinuity across the core-envelope interface.

At this point we introduce two key parameters that are used extensively in subsequent discussions of sequences of bipolytropic models. The fractional core mass of a bipolytrope is defined as

$$\nu = M_{\rm c}/M \tag{3.21}$$

where $M_{\rm c}$ is the mass of the core and M is the total mass. The fractional core radius is

$$q = R_{\rm c}/R \tag{3.22}$$

where $R_{\rm c}$ is equatorial radius of the core and R is equatorial radius of the whole configuration. Although the notation for the fractional core radius, q, conflicts with the mass ratio introduced earlier, we decided to use this notation for the ease of comparison with the literature, $\rm e.g.$ Eggleton *et al.* (1998). The fractional core mass and radius are key to model comparisons as well as astrophysically relevant structures. For example, the SC limit is understood in terms of the ν-q diagram (Figure 4.7 on page 38), as we shall see in section 4.1.

3.3 Mass Transfer in Binaries

In this section we briefly review the analytical framework needed to understand the dynamical evolution of mass transfer in close binary systems. Although the following semi-analytical results are derived for separated binary systems in the point mass approximation, they also apply to contact binaries at least qualitatively. This section will also help us interpret the behavior of an interacting binary system.

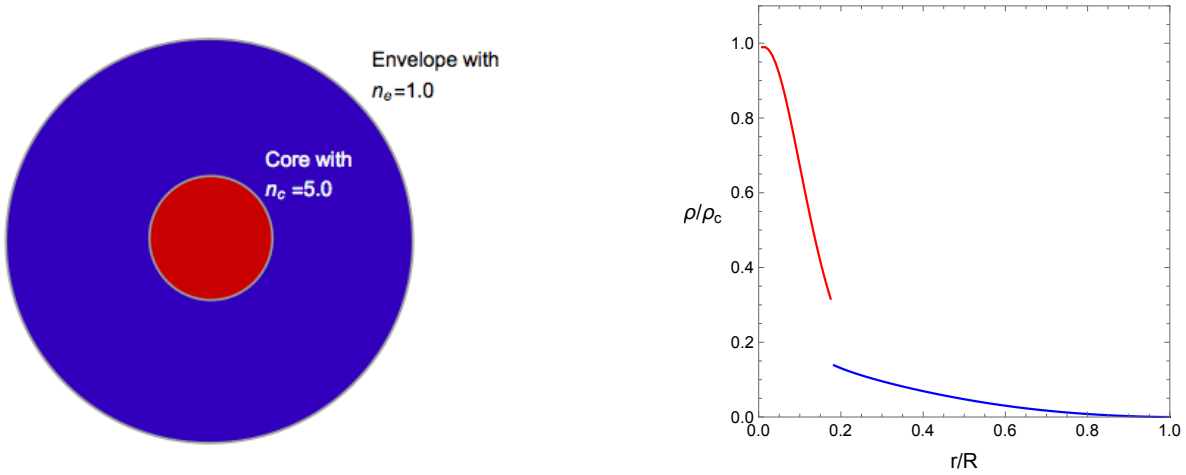

(a) Cross section

(b) Density profile

FIGURE 3.3: A schematic depicting the core-envelope structure in a bipolytropic star and its analytical density profile with $(n_c, n_e) = (5, 1)$ and $\alpha = 2.22$.

Whether a star transfers matter on to its companion in a binary system depends on the following condition.

$$\dot{R}_{\rm d} \geq \dot{R}_{\rm d,L} \tag{3.23}$$

where $R_{\rm d,L}$ is the radius of the Roche lobe of the donor. As seen in section 2.2.1, the Roche lobes are not spherical, but teardrop shaped. The radius of a Roche lobe is defined as the radius corresponding to a sphere with the same volume as that occupied by the Roche lobe. In a close binary system, one or both the stars can have shapes conforming to the critical equipotential surfaces, and far from a perfect sphere. Thus radius of a star is also defined in a similar way. If, as a result of the mass transfer, the Roche lobe radius shrinks at a rate faster than that of the stellar radius, the mass transfer will be unstable. We will next analyze the factors that affect this stability condition for mass transfer.

The period of a binary, P, is related to the separation, a, through Kepler's $3^{\rm rd}$ law,

$$P^2 = \frac{4\pi^2}{\rm GM} a^3. \tag{3.24}$$

The orbital angular momentum of the binary is

$$J_{orb} = (M_1 a_2^2 + M_2 a_1^2) a^2 \Omega, \tag{3.25}$$

where $a_1 = M_2/M$ and $a_2 = M_1/M$ are distances of the two stars from the CoM and M is the total mass. Here either M_1 or M_2 can be the donor star and the mass ratio is defined as $q = M_2/M_1$. Combining the above two equations and eliminating Ω, we get

$$J_{orb} = M_1 M_2 \left(\frac{Ga}{M}\right)^{1/2}. \tag{3.26}$$

The logarithmic time derivative of this equation gives

$$\frac{\dot{J_{orb}}}{J_{orb}} = \frac{\dot{M}_1}{M_1} + \frac{\dot{M}_2}{M_2} + \frac{\dot{a}}{2a} - \frac{\dot{M}}{2M}. \tag{3.27}$$

For simplicity if we assume a conservative mass transfer, where $\dot{J}_{orb} = 0$ and $\dot{M} = 0$, then $\dot{M}_1 = -\dot{M}_2$, and Equation 3.27 now becomes

$$\frac{\dot{a}}{a} = 2\frac{-\dot{M}_2}{M_2}(1-q). \tag{3.28}$$

Thus we find the critical value for the mass ratio at $q_a = 1$ and for $q_a > 1$, the separation shrinks on mass transfer, while for $q_a < 1$, the separation increases. A simpler approximation of the Roche lobe radius (Equation 2.3) which works well for $0.1 \lesssim q \lesssim 0.8$ is given by (Paczyński, 1971),

$$\frac{R_{2,L}}{a} = 0.462\left(\frac{M_2}{M}\right)^{1/3}, \tag{3.29}$$

where M_2 corresponds to the less massive star. Logarithmic differentiation of this equation gives

$$\frac{\dot{R}_{2,L}}{R_{2,L}} = \frac{\dot{a}}{a} + \frac{\dot{M}_2}{3M_2} - \frac{\dot{M}}{3M}. \tag{3.30}$$

Combining Equation(3.27) and Equation(3.30), we get

$$\frac{\dot{R}_{2,L}}{R_{2,L}} = \frac{2\dot{J_{orb}}}{J_{orb}} - \frac{2\dot{M}_1}{M_1} - \frac{5\dot{M}_2}{3M_2} + \frac{2\dot{M}}{3M}. \tag{3.31}$$

For conservative mass transfer, Equation 3.31 becomes

$$\frac{\dot{R}_{2,L}}{R_{2,L}} = -\frac{2\dot{M}_2}{M_2}\left(\frac{5}{6} - \frac{M_2}{M_1}\right). \tag{3.32}$$

Thus $q_{RL} = 5/6$ is a critical mass ratio, since if $q > 5/6$ the Roche lobe of the donor will shrink on mass transfer.

Now consider the behavior of the donor to mass loss, or the left hand side of Equation 3.23. According to Equation 3.32, unless the star can keep up with the contracting Roche lobe, mass transfer for $q > 5/6$ is unstable. The outcome of mass transfer thus depends on the response of the donor's radius to mass loss. This can be derived from the donor's mass-radius relationship,

$$R \propto M^{\xi}. \tag{3.33}$$

For ZAMS stars, the power law exponent ξ equals 0.8 for low-mass stars ($M < 1M_{\odot}$), and that equals 0.57 for high-mass stars ($M > 1M_{\odot}$). Taking the logarithmic time derivative of Equation 3.33 and putting this in Equation 3.32, we get the stability condition

$$q_{\rm crit} = \frac{5}{6} + \frac{\xi}{2}, \tag{3.34}$$

so mass transfer will be unstable above this mass ratio, $q_{\rm crit}$. For a spherical polytrope, the mass-radius relationship is given by

$$R \propto M^{\frac{1-n}{3-n}}, \tag{3.35}$$

hence,

$$q_{\rm crit} = \frac{4n-9}{3(n-3)}. \tag{3.36}$$

Hjellming & Webbink (1987) give the adiabatic response of a mass losing, spherical bipolytrope assuming continuous density, mass and pressure at the core-envelope interface, and a constant adiabatic index (γ). The stability condition is identical to Equation 3.36, where the polytropic index is replaced with that of the core only.

The above calculations are performed using simplified assumptions and the behavior of non-spherically symmetric polytropic or bipolytropic models is quantitatively different, in general. We have assumed a conservative mass transfer where there is no mass loss or angular momentum loss from the system, which is not always true. The equations are derived using point masses, the stars however, are extended bodies and this is especially true in close binaries where their shapes are significantly deformed. The interactions between the orbital and spin orbital momenta are also neglected. The extended mass distribution also affects the Roche geometry assumed throughout the calculations. The equations for extended bodies cannot be solved without the use of numerical techniques such as described in this dissertation. However, the results obtained in this section give us an insight into the binary interactions that take place during mass transfer in a binary system.

Chapter 4
Self Consistent Field Method

First introduced by Ostriker & Mark (1968), the self consistent field (SCF) technique is an iterative method of finding the equilibrium solution of a rotating, gravitationally bound fluid. The SCF method was initially used for describing the structure of an axisymmetric star having kinetic energy of rotation comparable to its gravitational energy. Hachisu (1986a) improved this method to produce rapidly rotating, self-gravitating structures with polytopic as well as zero temperature white dwarf EoS. Later, he developed a variation of this method and showed that it can be used for systems without axial symmetry, such as binary or multiple star systems. These improved methods of calculating equilibrium structures are called Hachisu's Self Consistent Field (HSCF) techniques. Motl *et al.* (2002) used a more generalized version of the HSCF method in order to construct binaries with unequal masses.

In this section we describe a computational method to determine the equilibrium structures of rotating bipolytropes. This is achieved by modifying the HSCF method (Hachisu, 1986a); this technique is called the bipolytropic self-consistent field or the BSCF method for convenience (Kadam *et al.*, 2016). The core and envelope can have different polytropic indices and the composition difference between them can be represented as a ratio of the average molecular weights. We confirm the validity of this method by comparing the results with known analytical as well as numerical results. The bipolytropic models obtained can have a high degree of flatness or a high $T/|W|$, where T is the kinetic energy and W is the gravitational energy of the system. Although real stars rotate differentially (Zeipel, 1925), only uniform rotation is considered because this is a good first order estimate of the rotational properties and we are ultimately interested in tidally locked close binaries. The v-constant (constant rotational velocity) or j-constant (constant angular momentum per unit mass) configurations could be obtained by following Hachisu (1986a). Onion-like composite polytropic structures may also be possible, however, this study is restricted to only bipolytropes.

The reliability of the equilibrium configurations is tested by comparing them with well-known analytical as well as numerical results. We describe cases where the bipolytropic structure obtained can give us insight into the internal structure of astrophysical objects. The implementation of the BSCF method is then discussed in the case of close, tidally locked binaries. There are no analytical or numerical solutions to make direct comparisons of such a binary system. We discuss the numerical simulations of these bipolytropic binaries in the next sections.

4.1 Rapidly Rotating Bipolytropes

In this section we discuss the construction of rapidly rotating, single, bipolytropic spheroidal as well as toroidal structures with the BSCF method. We make the following two assumptions while using the BSCF technique. The star (spheroid) or torus is assumed to be rotating axisymmetrically and the angular velocity (Ω) throughout the structure is uniform. In a frame of reference that is spinning with the star, the vector equation of motion of a self-gravitating body in equilibrium is

given by,

$$\frac{1}{\rho}\nabla P + \nabla(\Phi + \Omega^2\Psi) = 0, \tag{4.1}$$

where Ψ is the coordinate-dependent part of the centrifugal potential

$$\Psi = -\frac{R^2}{2}, \tag{4.2}$$

and Φ is the gravitational potential. With the specific enthalpy of the gas given by

$$H = \int_0^{\mathrm{P}} \frac{\mathrm{d}P}{\rho}, \tag{4.3}$$

Equation 4.1 can be integrated to obtain

$$H + \Phi + \Omega^2\Psi = \mathrm{C_B} \tag{4.4}$$

where $\mathrm{C_B}$ is the integration constant – analogous to the Bernoulli constant in classical fluid flows. The outer boundary condition is that the density is zero at the stellar surface. Integrating Equation 4.3 with a polytropic EoS gives the enthalpy as a function of density

$$H = (1+n)\kappa\rho^{\frac{1}{n}}, \tag{4.5}$$

hence the enthalpy is also zero at the outer boundary.

In order to determine a bipolytropic equilibrium structure uniquely, a possible pair of parameters are the axis ratio (the ratio of the equatorial to the polar radius) and core radius fraction (the ratio of the equatorial radius of the core to the radius of the whole star). Figure 4.1 shows a schematic diagram of a meridional cross section of a star (top panel) and of a toroidal configuration (bottom panel). Just like the HSCF method, the rotation rate (or the core mass fraction, in the case of a bipolytrope) cannot be specified a priori. We can only input the location of the outer boundary points A and B which in turn determine the rotation rate. The lower the axis ratio, the faster the resulting configuration rotates, hence the angular velocity is controlled by means of points A and B. As implemented here, the location of the core-envelope interface can be determined using point C or by specifying the density at which the transition between core and envelope takes place. For a torus, the points A and B specify an inner and an outer radius in the equatorial plane.

In order to get an equilibrium solution, Poisson's equation

$$\nabla^2\Phi = -4\pi\mathrm{G}\rho \tag{4.6}$$

and the hydrostatic equation (Equation 4.4) are solved iteratively as follows. We have to assume or "guess" an initial density distribution satisfying the outer boundary conditions. The BSCF method is not sensitive to this initial distribution. A typical choice for the initial guess for a spheroid is a constant density cone, which would look like a right triangle joining points A and B in a meridional cross section. For a toroid, the cross section of initial density would look like

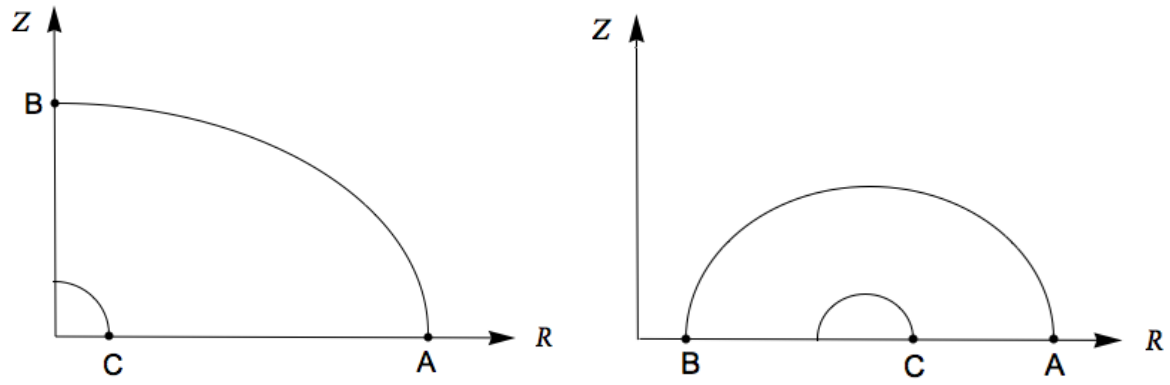

(a) Spheroid (b) Toroid

FIGURE 4.1: A schematic of the meridional cross section of rotating figures in cylindrical coordinates, showing the outer boundary points A, B and the core interface, C, in the case of a spheroidal and a toroidal bipolytropic structure.

a box. The potential field (Φ) throughout the grid is calculated from this density distribution by solving Poisson's equation.

The integration constant for the core ($\mathrm{C_c}$) is different from that for the envelope ($\mathrm{C_e}$) in general. Hence for the stellar core, Equation 4.4 becomes

$$H + \Phi + \Omega^2\Psi = \mathrm{C_c} \quad \text{when} \quad \rho \geq \rho_{\mathrm{ci}} \tag{4.7}$$

and the same equation for the envelope is

$$H + \Phi + \Omega^2\Psi = \mathrm{C_e} \quad \text{when} \quad \rho < \rho_{\mathrm{ci}}. \tag{4.8}$$

Since $H = 0$ at points A and B,

$$H_{\mathrm{A}} = -\Phi_{\mathrm{A}} - \Omega^2\Psi_{\mathrm{A}} + \mathrm{C_e} = 0, \tag{4.9}$$

$$H_{\mathrm{B}} = -\Phi_{\mathrm{B}} - \Omega^2\Psi_{\mathrm{B}} + \mathrm{C_e} = 0. \tag{4.10}$$

Hence the angular velocity of the system can be obtained as

$$\Omega^2 = -\frac{\Phi_{\mathrm{A}} - \Phi_{\mathrm{B}}}{\Psi_{\mathrm{A}} - \Psi_{\mathrm{B}}}. \tag{4.11}$$

The integration constant for the envelope can now be calculated from Ω as

$$\mathrm{C_e} = \Phi_{\mathrm{A}} + \Omega^2\Psi_{\mathrm{A}} = \frac{\Phi_{\mathrm{A}}\Psi_{\mathrm{B}} - \Phi_{\mathrm{B}}\Psi_{\mathrm{A}}}{\Psi_{\mathrm{B}} - \Psi_{\mathrm{A}}}. \tag{4.12}$$

Now the continuity of pressure at the core-envelope interface implies

$$H_{\mathrm{ci}} = H_{\mathrm{ei}} \frac{(n_{\mathrm{c}} + 1)}{(n_{\mathrm{e}} + 1)} \frac{\rho_{\mathrm{ei}}}{\rho_{\mathrm{ci}}}, \tag{4.13}$$

where $H_{\rm ei}$ can be obtained from $\rm C_e$

$$H_{\rm ei} = -\Phi_{\rm i} - \Omega^2\Psi_{\rm i} + \rm C_e. \tag{4.14}$$

The integration constant for the core can be obtained from

$$\rm C_c = H_{ci} + \Phi_{ci} + \Omega^2\Psi_i, \tag{4.15}$$

and the enthalpy throughout the star can be calculated from Equations 4.7 and 4.8. Once the enthalpy is known, new density distributions of the core and the envelope can be calculated from Equation 4.5 as

$$\frac{\rho_{\rm c}}{\rho_{\rm c-max}} = \frac{\rho_{\rm c}}{\rho_0} = \left(\frac{H_{\rm c}}{H_{\rm c-max}}\right)^{n_{\rm c}} \tag{4.16}$$

and

$$\frac{\rho_{\rm e}}{\rho_{\rm e-max}} = \frac{\rho_{\rm e}}{\rho_{\rm ei}} = \left(\frac{H_{\rm e}}{H_{\rm e-max}}\right)^{n_{\rm e}}. \tag{4.17}$$

The $\rho_{\rm c-max}$, or the central density ρ_0 is chosen to be unity and the envelope density can be normalized with respect to this central density,

$$\frac{\rho_{\rm e}}{\rho_0} = \frac{\rho_{\rm ei}}{\rho_0}\left(\frac{H_{\rm e}}{H_{\rm e-max}}\right)^{n_{\rm e}} = \frac{\rho_{\rm ci}}{\rho_0}\frac{\mu_{\rm e}}{\mu_{\rm c}}\left(\frac{H_{\rm e}}{H_{\rm e-max}}\right)^{n_{\rm e}}, \tag{4.18}$$

and

$$\frac{\rho_{\rm e}}{\rho_0} = \frac{\mu_{\rm e}}{\mu_{\rm c}}\left(\frac{H_{\rm ci}}{H_{\rm c-max}}\right)^{n_{\rm c}}\left(\frac{H_{\rm e}}{H_{\rm e-max}}\right)^{n_{\rm e}}. \tag{4.19}$$

This new density distribution is used for the next iteration cycle. The iteration process is repeated until the relative changes in $\rm C_c$, $\rm C_e$ and Ω^2 are smaller than the prescribed convergence criterion, δ. Here, we use $\delta = 1 \times 10^{-3}$ for all our calculations, unless stated otherwise.

Using the BSCF method as described above, the fractional core radius q, essentially becomes the control parameter. The analytical relationship between fractional core mass, ν, and fractional core radius, q, becomes double valued as the ratio of molecular weights, α, increases and eventually at $\alpha = 3$, there cannot be equilibrium solutions above a certain value of ν. This is the aforementioned SC limit for the core mass fraction (see Figure 4.7 on page 38). Since only point $\rm C$ and hence the value of q is specified with the BSCF method, we cannot directly control the fractional core mass, ν. For a given value of q, if there exist two equilibrium values of ν, we observe that the method always converges to the solution with the lower ν. In order to overcome this drawback, the BSCF method can be modified to use the ratio of the density at the core side of the interface and the central density, ρ_{ci}/ρ_0, as the control parameter instead of point $\rm C$, which uniquely determines the configuration. The equations involved are exactly the same as mentioned so far and the radius of the core (q) is calculated from the converged model. The implications of this modification to the BSCF method are discussed later in this chapter.

4.2 Numerical Tests of Rotating Bipolytropes

We began by using a cylindrical geometry for the computational grid because a rotating body is naturally described in cylindrical coordinates. See section 5.1 below. The Poisson solver with this geometry was already available to our research group from our previous numerical work (Motl *et al.*, 2002). This not only minimized the time for development of the BSCF method significantly, but also provided a well-tested, reliable and accurate method for the investigations. The normalization convention used is the same as described in Hachisu (1986a), mainly for ease of comparison. The basis set of dimensionless quantities is the maximum density (ρ_0), equatorial radius of the star (R), and the gravitational constant (G). All computations are performed in the dimensionless form of the variables.

The most compute-intensive section in the BSCF method is the Poisson solver, which is used for obtaining the gravitational potential from the specified density distribution at each iteration. For an assumed isolated density distribution, the boundary condition for the potential is that it goes to zero at infinity. In practice, since the grid is always finite, we have to calculate the potential at the edge of the grid which is outside the mass distribution. This boundary potential is constructed using a compact expression for the Green's function in cylindrical coordinates. As described in Cohl & Tohline (1999), we get an analytical expression for the gravitational potential in terms of half-integer degree Legendre functions of the second kind. This means that a very accurate boundary solution for our discretized mass distribution can be obtained. This technique is particularly useful for studying systems which conform well to azimuthal symmetry because it can be applied to very flattened or elongated bodies without suffering penalties in either accuracy or computation time.

We use an effective two dimensional version of the Poisson solver by setting the number of azimuthal modes supported in the Green's functions to one, thereby enforcing axial symmetry. In order to obtain the interior solution for the potential, an alternating direction implicit (ADI) scheme (Peaceman & Rachford, 1955) is used. The computational grid geometry is cylindrical with azimuthal symmetry. The resolution of the grid is denoted by $\mathrm{NUMR} \times \mathrm{NUMZ}$, where NUMR is the number of cells in the R-direction and NUMZ is the number of cells in the vertical or z-direction. All physical quantities are calculated at the cell centers. The first cell in both the R and z-direction is a boundary cell and the unit distance between consecutive cells in both directions is equal, i.e. $\mathrm{d}z = \mathrm{d}R$.

The quality of a converged solution is quantified using the virial error (VE), which is a global measure of the accuracy of the equilibrium of a non-linear dynamical system.

$$VE = \frac{\mid 2T + W + 3\Pi \mid}{\mid W \mid} \tag{4.20}$$

where Π is the volume integral of the pressure,

$$\Pi = \int_V P \, \mathrm{d}V \tag{4.21}$$

This expression is derived from the scalar virial equation, hence the virial error should ideally be zero for a system in equilibrium. A typical value for virial error with a resolution of 130×130 is

10^{-4}. This value can be pushed lower by increasing the resolution, while simultaneously decreasing δ by an appropriate amount.

4.2.1 Polytropes, Maclaurin and Dyson-Wong Sequences

We construct continuous polytropic structures by setting the polytropic index of the core equal to that of the envelope and the ratio of molecular weights to unity. These models should be identical to single polytropes and satisfy all the associated properties.

Maclaurin spheroids (MS) correspond to the equilibrium sequence of self-gravitating and uniformly rotating incompressible spheroids (Tassoul, 1978). This sequence transitions in a continuous fashion into Dyson-Wong (DW) toroids (or the one-ring sequence) through the Eriguchi-Sugimoto (ES) sequence, as the configurations rotate with increasing angular momentum (Eriguchi & Sugimoto, 1981). This transition from axisymmetric spheroids to toroids is depicted in Figure 4.2. As a numerical test of the BSCF method, the MS, ES and DW sequences are reproduced for an incompressible fluid with $n = 0$. The results are plotted in Figure 4.3. The ratio of the kinetic to the potential energy, $T/|W|$, is a rough indicator of the stability of the rotating system, as the original SCF proposed by Ostriker & Mark (1968) failed to produce solutions for a high degree of flatness ($T/|W| > 0.25$). The smooth curves are obtained with the BSCF method as the boundary point B moves along the z-axis (generating flatter spheroids by decreasing the axis ratio) and then along the R-axis (generating thinner toroidal structures) as depicted in Figure 4.1.

Similar sequences are also constructed for polytropic indices $n = 0.1,\ 0.5,\ 1.5,\ 3.0$ and 4.0. The results, in excellent agreement with the calculations done by Hachisu (1986a), are plotted in Figure 4.4. Although the sequences for toroids show more scatter than those for the spheroids, they are consistent with the expected curves.

4.2.2 Spherically Symmetric Bipolytropes

As an additional test of the validity of the BSCF method, we constructed non-rotating bipolytropic models by setting the axis ratio to one. The properties of these structures were compared to analytical solutions.

The analytical case of spherically symmetric $(n_{\rm c}, n_{\rm e}) = (5, 1)$ bipolytropes was first investigated by Eggleton *et al.* (1998). They demonstrate that these bipolytropes exhibit an upper core mass fraction limit analogous to the SC limit. The analytical solutions to these bipolytropes are reproduced with the BSCF method. In Figures 4.5 and 4.6, respectively, we plot the core mass fraction (ν) and the logarithm of the inverse of core radius fraction (q) as a function of the logarithm of the core density contrast, defined as $\rho_0/\rho_{\rm ci}$. The points which are obtained from the BSCF models match the analytical sequences very well.

The aforementioned SC limit is better understood with the help of the ν-q curve. As depicted in Figure 4.7, for a high enough ratio of average molecular weight ($\alpha \geq 3$), the fractional mass shows an upper limit above which no equilibrium configurations exist. All configurations up to this SC limit can be obtained with the BSCF method. The open circles in Figure 4.7 denote the switch in the BSCF method from using point $\rm C$ in Figure 4.1 to using the ratio of the value of the density at the core side of the interface and the central density (ρ_{ci}/ρ_0, also equal to the

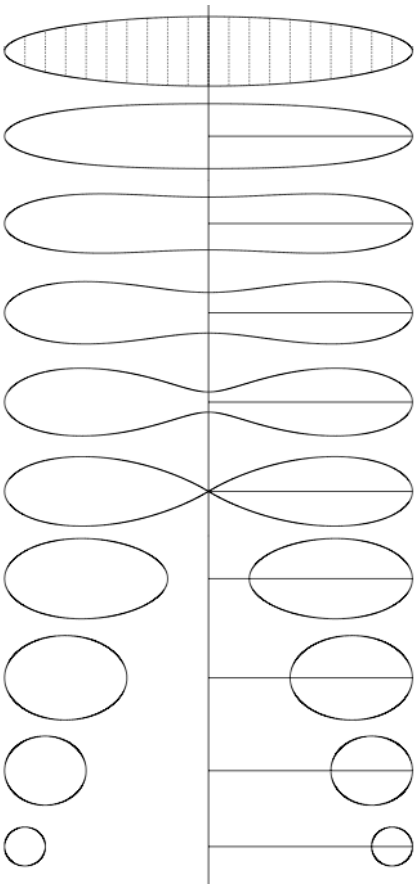

FIGURE 4.2: The meridional cross section of the density profile of uniformly rotating incompressible fluids as the Maclaurin spheroid (denoted by hatching) transitions into Dyson-Wong toroidal configurations (Ansorg *et al.*, 2003).

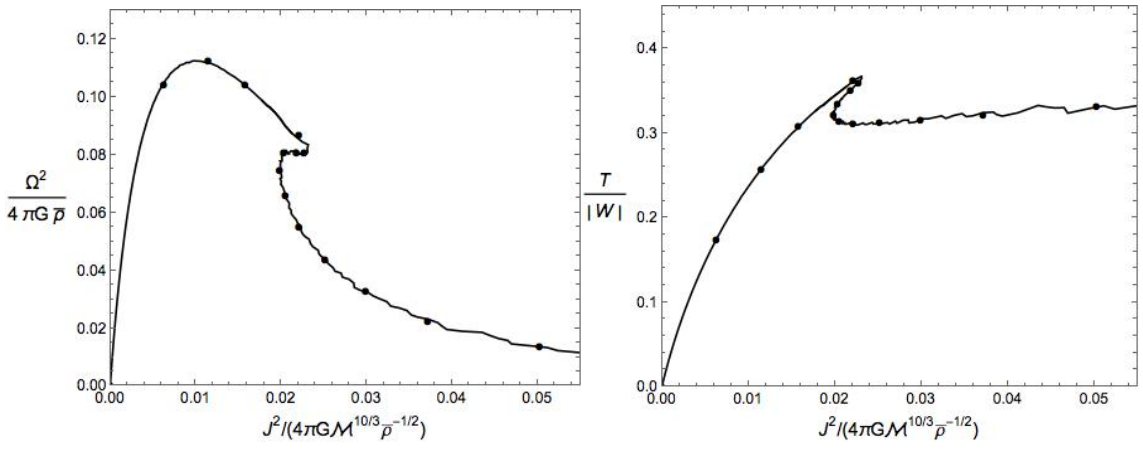

(a) Ω^2 vs. J^2 (b) $T/|W|$ vs. J^2

FIGURE 4.3: Dimensionless squared angular velocity ($\Omega^2/4\pi\mathrm{G}\bar{\rho}$), and rough stability indicator ($T/|W|$) versus dimensionless squared angular momentum ($J^2/4\pi\mathrm{G}M^{10/3}\bar{\rho}^{-1/2}$) for the Maclaurin, Eriguchi-Sugimoto and Dyson-Wong sequences. The solid lines correspond to the models obtained using the BSCF method and the points are previously calculated values (Hachisu, 1986a).

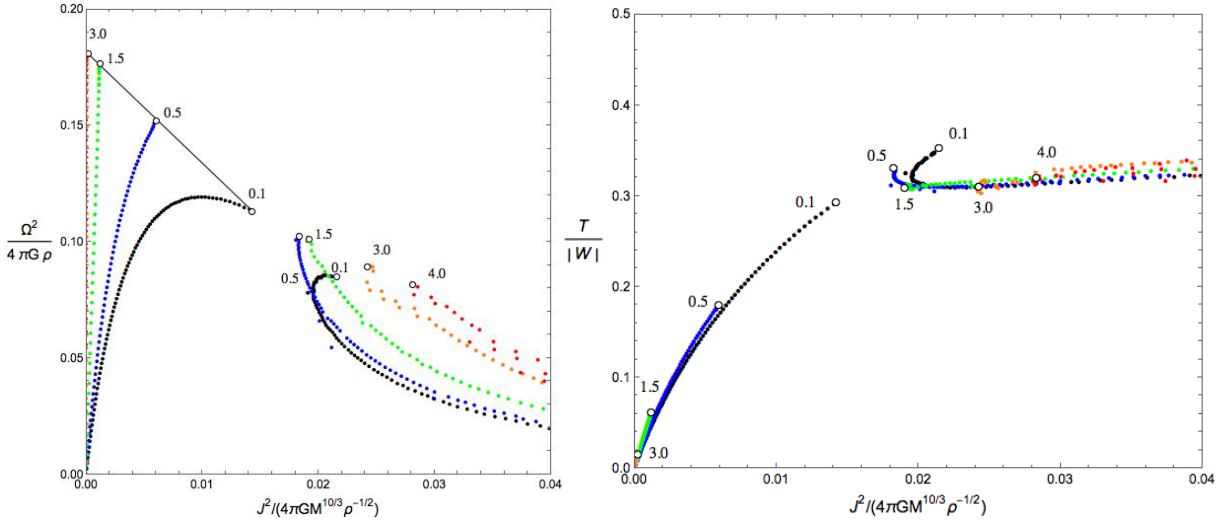

(a) Ω^2 vs. J^2 (b) $T/|W|$ vs. J^2

FIGURE 4.4: Dimensionless squared angular velocity ($\Omega^2/4\pi\mathrm{G}\bar{\rho}$), and rough stability indicator ($T/|W|$) versus dimensionless squared angular momentum ($J^2/4\pi\mathrm{G}M^{10/3}\bar{\rho}^{-1/2}$) for $n = 0.1$ (black), 0.5 (blue), 1.5 (green), 3.0 (yellow) and 4.0 (red). Open circles denote critical rotation, joined by a straight line for spheroids.

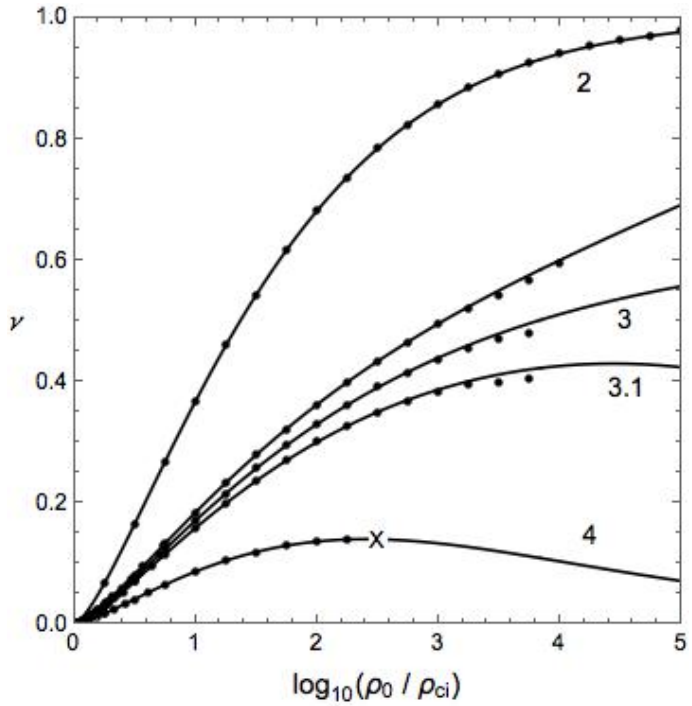

FIGURE 4.5: Fractional core mass (ν) versus logarithm of core density contrast ($\rho_0/\rho_{\mathrm{ci}}$) for a $(n_{\mathrm{c}}, n_{\mathrm{e}}) = (5, 1)$ bipolytrope with $\alpha = 2,\ 2.9,\ 3,\ 3.1$ and 4. Points are BSCF results and the smooth curves are analytically determined (Eggleton *et al.*, 1998). The cross denotes termination of the sequence at the SC limit.

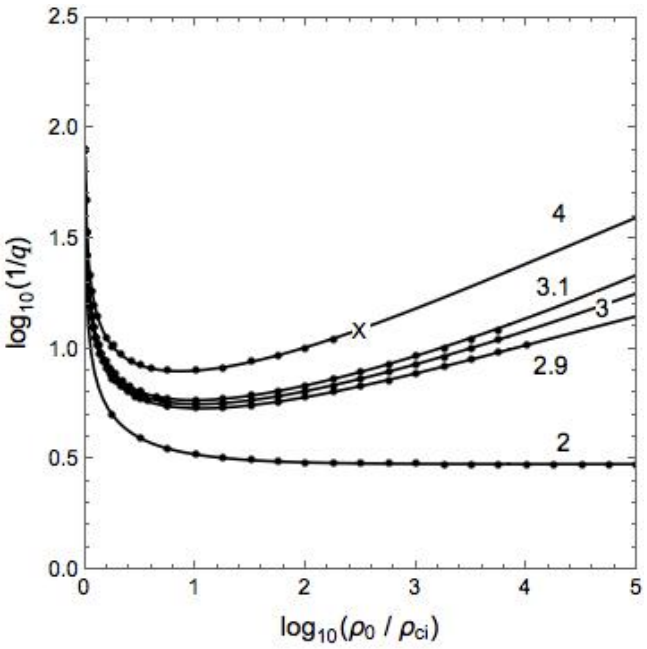

FIGURE 4.6: Logarithm of the inverse of fractional core radius $(1/q)$ versus logarithm of core density contrast $(\rho_0/\rho_{\rm ci})$ for a $(n_{\rm c}, n_{\rm e}) = (5, 1)$ bipolytrope with $\alpha = 2$, 2.9, 3, 3.1 and 4. Points are BSCF results and the smooth curves are analytically determined (Eggleton *et al.*, 1998). The cross denotes termination of the sequence at the SC limit.

inverse of the density contrast) as the control parameter, in determining the size of the core. The exact location of the core interface or q is now calculated using the enthalpy field.

As the density contrast increases or $\rho_{\rm ci}/\rho_0$ gets progressively smaller, the core gets more centrally condensed. This results in an equilibrium structure with a tenuous envelope and a core resembling a delta function, which contains fewer and fewer points. In order to calculate parameters ν and q accurately, we need to resolve this core with a high resolution model. We implemented Richardson extrapolation (Richardson, 1911) at two different resolutions (total equatorial resolution of 120 and 240 cells) in order to get better estimates of ν and q in Figures 4.5, 4.6 and 4.7. This is because higher resolution models which could resolve the core were prohibitive in computing time without parallelizing the code. This approach is also ultimately limited by the resolution. This can be seen in Figures 4.5 and 4.7 for $\alpha = 2.9$, 3 and 3.1. For these curves, the BSCF results match the analytical sequences only up to certain points. Obtaining these full curves may require higher resolution and higher order Richardson extrapolations.

4.3 Applications of Rotating Bipolytropes

4.3.1 Schönberg-Chandrasekhar Limit

As a star evolves along the main sequence, it burns the hydrogen in the central region into helium. Near the end of the main sequence phase, an inert helium core is formed at the center and the hydrogen continues to burn around this core in a shell. This core is essentially isothermal in order for it to be in thermal equilibrium. If the gas is assumed ideal, because of the interplay between internal pressure and self gravity, the surface pressure of such a core decreases strongly with the core mass fraction. Schönberg & Chandrasekhar (1942) calculated that for a star with an

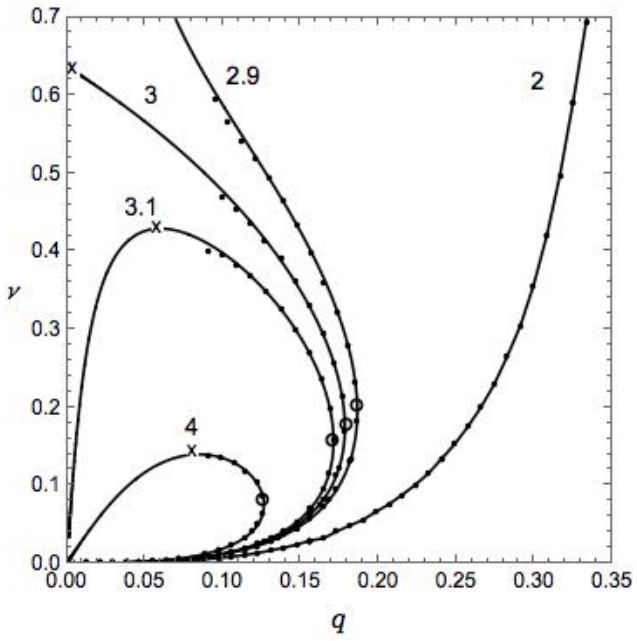

FIGURE 4.7: Plot of fractional core mass ν versus fractional core radius q for a bipolytrope with $(n_{\rm c}, n_{\rm e}) = (5, 1)$ for different values of α. The smooth curves are analytically determined and the points denote the sequences obtained using the BSCF method. The crosses are SC limits for a given α and open circles denote the switch from point $\rm C$ (see Figure 4.1) to ρ_{ci}/ρ_0 as the free parameter in determining the mass of the core.

isothermal core, a radiative envelope and a large enough molecular weight difference between the two, this core mass fraction has an upper limit above which the core cannot support the envelope. When this SC limit is reached, the star must respond by readjusting itself on a Kelvin-Helmholtz timescale by contraction of the core. The resultant liberation of the gravitational energy causes an increase in the luminosity. Applegate (1988) argues that this exceeds the maximum luminosity that the radiative envelope can carry and the envelope density is forced down. This causes the envelope to expand and we get evolution along the red giant branch. This would be a first order approximate answer to the question "Why stars become red giants". In real stars the process is much more complicated and non-linear, with nuclear burning, opacities, convection, chemical composition and various other quantities affecting the structure of the star (e.g. see Sugimoto & Fujimoto (2000)).

Maeder (1971) was the first to discuss the effects of rotation on the SC limit. He used first order perturbation analysis on the virial expression for a star with an isothermal core and a radiative envelope. In conclusion, rotation could increase or decrease the SC limit, depending on the actual rotational profile in the stellar interior. For a uniform rotation, the SC limit decreases but even at the maximum rotation the decrease is only about 3%.

As seen in the section 4.2.2, analytical bipolytropes also show an analogous SC limit above a certain jump in the average molecular weight. Here the effect of rotation on the SC limit on a bipolytrope with an $(n_{\rm c}, n_{\rm e}) = (5, 1)$ and a molecular weight ratio of 4 are analyzed. Figure 4.8 shows the ν-q sequences of these bipolytropes at different axis ratios. We see that as a bipolytrope

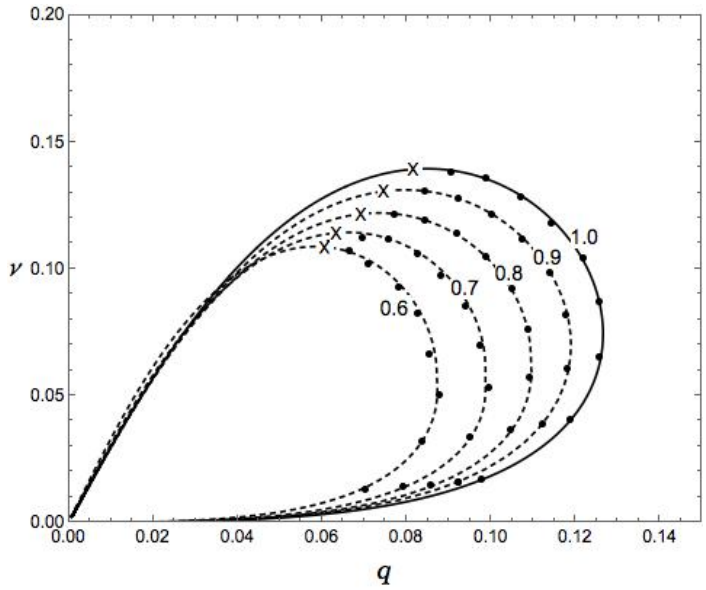

FIGURE 4.8: Plot of fractional core mass, ν, versus fractional core radius, q, for a bipolytrope with $(n_{\rm c}, n_{\rm e}) = (5, 1)$ and $\mu = 4$ for different axis ratios. The points denote the sequences obtained using the BSCF method. A cross denotes the SC limit and the dashed lines represent the trend for the corresponding sequence. The solid line is obtained from the non-rotating analytical solution.

rotates more rapidly, the maximum mass limit (denoted by a cross) decreases. A bipolytropic star rotating with an axis ratio of 0.6 would encounter the SC limit at a mass fraction more than 20% lower than its non-rotating counterpart. Note that these values are quantitatively true only in the case of a bipolytropic structure with $(n_{\rm c}, n_{\rm e}) = (5, 1)$, $\alpha = 4$ and uniform rotation. This decrease is about an order of magnitude larger than that predicted by Maeder (1971) for an isothermal core and a radiative envelope. An SCF technique incorporating more realistic EoS and rotational profiles may be necessary in order to obtain a better estimate of the effects of rotation on the SC limit of real stars.

The change in the SC limit with rotation can have significant consequences for our understanding of stellar evolution, particularly for high mass stars as they do not have a convective envelope to brake their rotation efficiently. These stars also live on the main sequence for a much shorter time so they can still be rotating rapidly as they evolve off the main sequence. The SC limit determines the fraction of the stellar mass that can be fused in nuclear reactions, thus affecting its lifetime spent on the main sequence. The effect due to rotation would be the next leading order of correction to the basic structure and evolution as would be dictated by the star's mass and chemical composition.

Dependance of the SC limit on rotation may also result in an observational test of the rotational profile in the stellar interior. The slight changes in the frequency or position of stars on the HR diagram due to the shift in the SC limit can relate to the rotation law. The SC limit should also be different in a close binary system as compared to an isolated star because of rotational flattening. Sophisticated stellar evolution codes like MESA (Paxton *et al.*, 2011) are required to estimate the consequences of these results.

4.3.2 Radii of gyration

Main sequence stars having masses between about 0.3-$1.3 M_{\odot}$ have a radiative core and a convective envelope. These low mass stars can be represented as a bipolytrope with $(n_{\rm c}, n_{\rm e}) = (3, 3/2)$ (Rappaport *et al.*, 1983; Beech, 1988). Rucinski (1988) computed sequences of fractional radii of gyration of such spherically symmetric and rigidly rotating bipolytropic models. The fractional radii of gyration for the core ($k_{\rm c}$) and envelope ($k_{\rm e}$) are defined such that the total angular momentum J is

$$J = MR^2\Omega({k_{\rm c}}^2 + {k_{\rm e}}^2) \tag{4.22}$$

where M and R are the total mass and equatorial radius of the star respectively. This also means that the total radius of gyration is ${k_{\rm t}}^2 = {k_{\rm c}}^2 + {k_{\rm e}}^2$. For an arbitrary stellar density distribution with the core-envelope interface located at i, we can calculate radii of gyration by integrating the moments of inertia,

$${k_{\rm c}}^2 = \frac{1}{MR^2}\int_0^{\rm i} r^2 \, {\rm d}m, \tag{4.23}$$

and

$${k_{\rm e}}^2 = \frac{1}{MR^2}\int_{\rm i}^{R} r^2 \, {\rm d}m. \tag{4.24}$$

We recreated the sequences of radii of gyration in Rucinski (1988) for the case of $(n_{\rm c}, n_{\rm e}) = (3, 3/2)$ as a function of the core radius fraction. The original sequences correspond to numerical integrations of the expressions for $k_{\rm c}$ and $k_{\rm e}$, which are derived from a bipolytropic solutions of the spherically symmetric Lane-Emden equation without a discontinuity. The BSCF models constructed also have no discontinuity in molecular weight and the axis ratio is unity, hence they are spherically symmetric. As depicted in Figure 4.9 the results of the BSCF method are indistinguishable from the previously calculated curves.

With the BSCF method, the effect of rotation on the radii of gyration can be explored. Figures 4.10, 4.11 and 4.12 summarize the results as the axis ratio is progressively decreased. As a star rotates faster at a given fractional core radius, the corresponding radius of gyration also decreases steadily. For the core, $k_{\rm c}^2$ shows a shift in the maximum value as the rotation increases. The sequence with an axis ratio of 0.62 terminates at $q = 0.87$ (open circle in Figures 4.10, 4.12) because this is the mass shedding limit. This means that the star is rotating at the critical velocity and no equilibrium configurations are possible above this value of q.

The dependence of the fractional radii of gyration on rotation can have implications for the rotational evolution of low-mass main sequence stars. A star can lose angular momentum through the process of magnetic braking as its wind is magnetically coupled to the rotation (Mestel, 1968). This is an efficient mechanism for the loss of angular momentum for a star possessing a magnetic field. Skumanich (1972) observed that G-dwarf stars in open clusters spin down following the empirical relation

$$v_{\rm e} \propto t^{-0.5} \tag{4.25}$$

where $v_{\rm e}$ is equatorial velocity and t is the age. Vilhu (1982) gives the semi-empirical law for magnetic braking

$$\frac{{\rm d}J}{{\rm d}t} \propto \Omega^N \tag{4.26}$$

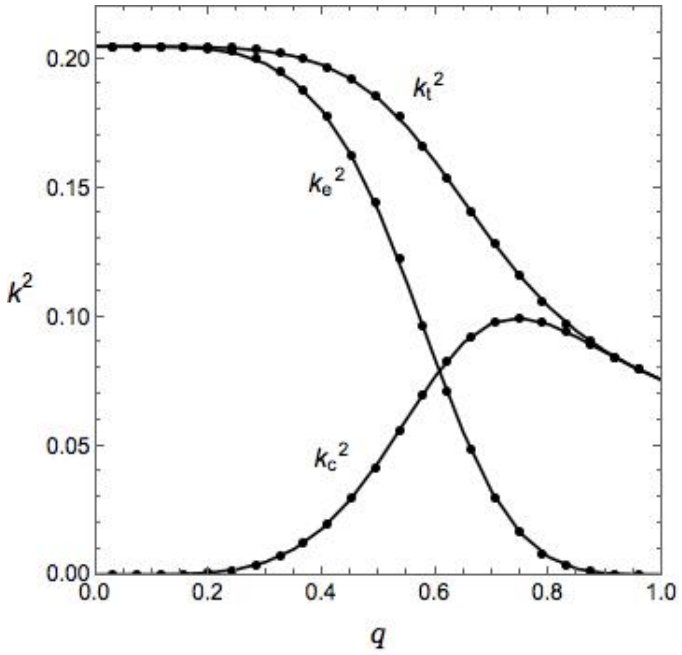

FIGURE 4.9: Fractional radii of gyration for a non-rotating polytrope with $(n_{\rm c}, n_{\rm e}) = (3, 3/2)$ and $\alpha = 1$. The points are BSCF results and the smooth curves are reproduced from Rucinski (1988). ${k_{\rm t}}^2$, ${k_{\rm c}}^2$ and ${k_{\rm e}}^2$ denote the curves for total, core, and envelope radii of gyration respectively.

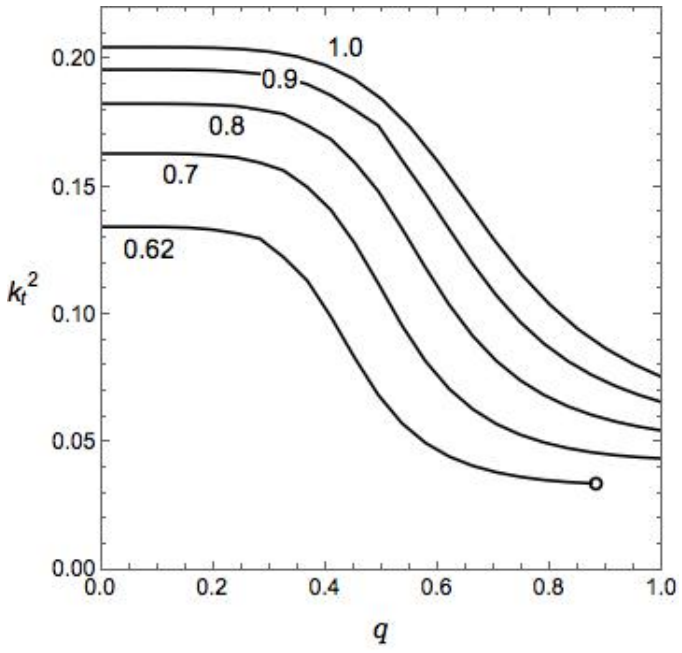

FIGURE 4.10: Total radii of gyration for rotating bipolytropes with $(n_{\rm c}, n_{\rm e}) = (3, 3/2)$ and $\alpha = 1$. The numbers denote the axis ratio of the models. The open circle denotes critical rotation or the mass shedding limit.

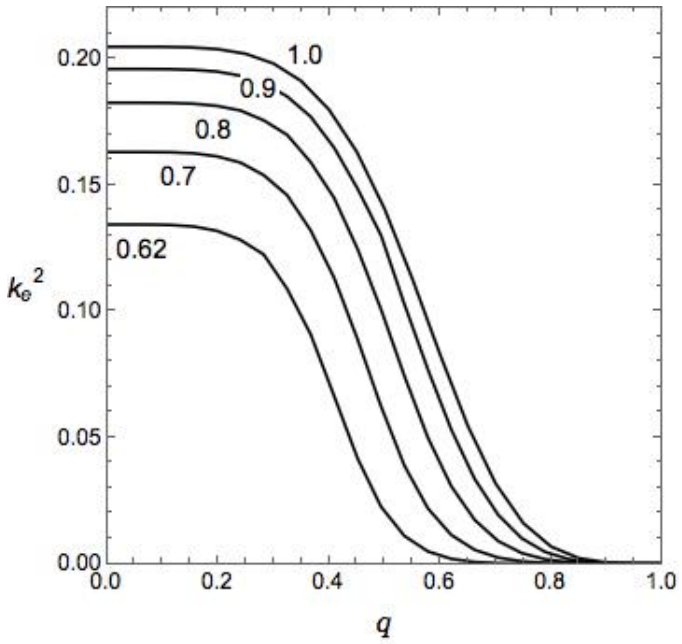

FIGURE 4.11: Fractional radii of gyration of the envelope for rotating bipolytropes with $(n_{\rm c}, n_{\rm e}) = (3, 3/2)$ and $\alpha = 1$. The numbers denote the axis ratio of the models.

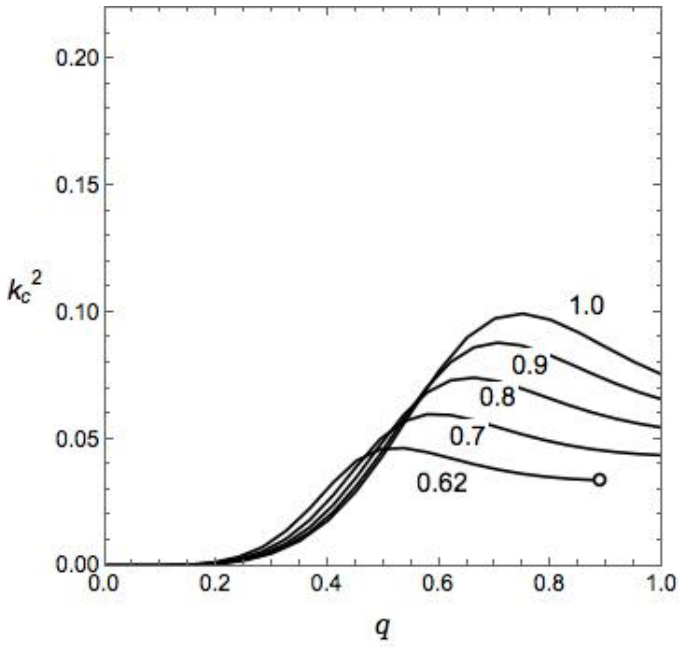

FIGURE 4.12: Fractional radii of gyration of the core for rotating bipolytropes with $(n_{\rm c}, n_{\rm e}) = (3, 3/2)$ and $\alpha = 1$. The numbers denote the axis ratio of the models. The open circle denotes critical rotation.

where N is the angular momentum loss parameter ($N = 3$ for the Skumanich Law). Here the underlying assumption is that the braking is not caused by the aging itself but the mechanism is directly related to the rotation of the star. Combining Equations 4.22 and 4.26, the characteristic timescale for magnetic braking can be given by

$$T_{\rm b} \approx J/\dot{J} \propto {k_{\rm t}}^2 M R^2 \Omega^{1-N}. \tag{4.27}$$

For low-mass stars it is possible that the convective envelope decouples from the radiative core and the measurements of the magnetic braking apply to the envelope only (Vilhu & Moss, 1986). The characteristic timescale for magnetic braking then depends on the radius of gyration of the envelope alone, hence

$$T_{\rm b} \ \propto {k_{\rm e}}^2 M R^2 \Omega^{1-N}. \tag{4.28}$$

In order to calculate the timescale of braking of the convective envelope as a function of stellar mass, we follow the same recipe as in Rucinski (1988). He used VandenBerg stellar models which have been calculated for a solar composition of $\rm Y = 0.27$ and $\rm Z = 0.0169$. The only input from these models that is used, apart from the overall mass-radius relationship, is the value of core mass fraction (ν) for a given stellar mass. The value of the angular momentum loss parameter decreases for more rapidly spinning stars (Vilhu, 1982) and we assume $N = 1$ for our calculations. Thus using the k_e values obtained from the BSCF method and Table V in Rucinski (1988) we can estimate the timescale for braking for the sequence of stars in the mass range $M = 0.5$-$1.2 M_{\odot}$.

Figure 4.13 summarizes the effects of rotation on the braking timescale of the convective envelope. For ease of comparison, the braking timescale is normalized to the value at $1 M_{\odot}$ for the Rucinski (1988) sequence (solid black line in Figure 4.13). The timescales for non-rotating bipolytropes calculated using the BSCF method are consistent with those estimated by Rucinski. Notice that the timescale plateaus and shows little variation below $0.9 M_{\odot}$ but in the mass range of 0.9-$1.2 M_{\odot}$, it drops precipitously. For rotating stars with an axis ratio of 0.7, this plateau below $0.9 M_{\odot}$ occurs at a significantly (about 25%) lower characteristic braking timescale. We chose an axis ratio of 0.7 in order to demonstrate the most extreme difference that rotation could reasonably make, since this axis ratio puts the rotational velocity of a star close to breakup. The sequences of braking timescales for axis ratios other than 0.7 will show trends similar to Figure 4.11.

This analysis may exaggerate the difference in braking time because as the stars slow down, the evolution of the fractional radius of gyration is not considered ($k_{\rm e}$ is assumed constant throughout the above exercise). The analysis also shows that the convective envelopes of these low-mass stars contain less initial angular momentum than previously estimated, when we take the distortion due to the rotation into account, irrespective of subsequent evolution. This should be reflected in the estimations of the braking time and previous calculations can be considered as upper limits. These results affect the observability of rapidly rotating stars in a given cluster as fast rotating stars brake on a shorter timescale. The results could also have implications for the evolution of short period binary systems, because the same braking scheme is generally used for estimating angular momentum loss in close binary systems (Vilhu, 1982).

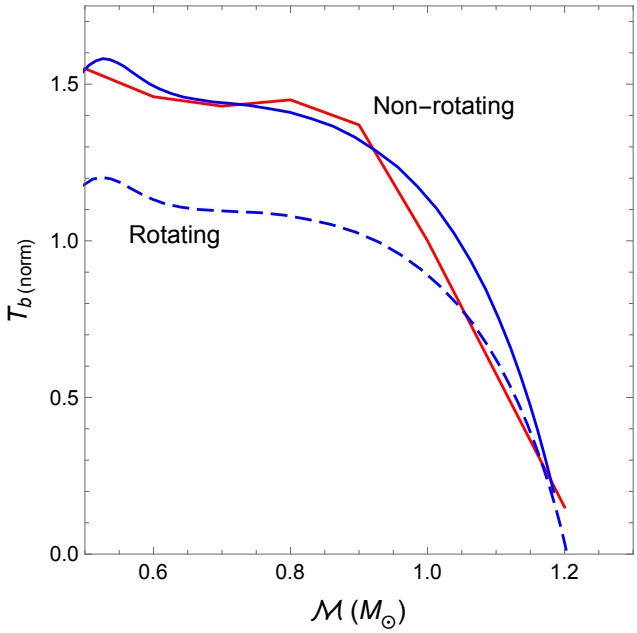

FIGURE 4.13: The timescale for braking of the convective envelope ($T_{\mathrm{b(norm)}}$) as a function of stellar mass (M). The red, solid line corresponds to the calculations performed by Rucinski (1988) using non-rotating VandenBerg models. The blue lines correspond to the bipolytropic sequences generated using the BSCF method for the same models. $T_{\mathrm{b(norm)}}$ is normalized to the value at $1M_\odot$ for the Rucinski sequence.

4.3.3 Interior of Jupiter

Rotating bipolytropes can be used to investigate the internal structure of gaseous planets or exoplanets. We present one such application for the planet Jupiter. A polytropic index of unity has often been assumed to represent Jupiter's internal structure (Stevenson 1982). In this exercise we consider one particular bipolytropic model of Jupiter proposed by Criss & Hofmeister (2015). We improve upon this by adding rotation, and observe the effects on various physical parameters. The hope is to not only reproduce the observed properties, but also to gain insight into the internal structure with minimum assumptions.

Criss & Hofmeister (2015) approximate the condensed metallic hydrogen core in Jupiter as an incompressible solid with $n_{\mathrm{c}} = 0$ and the gaseous envelope with $n_{\mathrm{e}} = 2.5$, which corresponds to a diatomic gas. They also have the core-envelope interface at $q = 0.8$ and a large discontinuity corresponding to $\alpha \approx 36.7$. Henceforth this model is called CH for convenience. The total radius of gyration (${k_{\mathrm{t}}}^2$) for a configuration is also called the normalized moment of inertia, $I_{\mathrm{norm}} = I/MR^2$, in conventional notation. Criss & Hofmeister (2015) show that I_{norm} for an $n = 1$ polytrope is inconsistent with the observed value of 0.254 for Jupiter (NASA, 2014), and the CH model is a better approximation. Since this model is one dimensional, it can be recreated with the BSCF method by using the same parameters ($n_{\mathrm{c}} = 0.0001$ instead of exactly zero, because $1/n_c$ is used explicitly) and setting the axis ratio to unity. The I_{norm} for this non-rotating model is only 2% off the value reported by Criss & Hofmeister (2015).

Apart from not incorporating rotation, the CH model has two major disadvantages. First, there is no justification for an abrupt and large jump ($\alpha \approx 36.7$) at the interface between core and the envelope. Nellis *et al.* (1998) showed that the transition between molecular to monoatomic metallic hydrogen is continuous so Jupiter has no distinct core-envelope boundary. The second drawback is the infinitesimal contribution of the envelope to the structural parameters. The gaseous envelope contributes only about 1.7% to the total $I_{\rm norm}$ and 0.6% to the total mass, essentially making the envelope fit irrelevant, as long as its contribution remains small enough (see CH model in Figure 4.14).

Both of these issues can be addressed with the models obtained with the BSCF method, by adding rotation and without assuming a jump in the molecular weight at the core-envelope interface. We use $(n_{\rm c}, n_{\rm e}) = (0.0001, 2.5)$ and $\alpha = 1$ in order to represent the same internal structure. With no rotation (call this model BN), the normalized moment of inertia equals 0.25 when the fractional core radius, $q = 0.34$. This size of the condensed core is much smaller than what is expected for Jupiter, as metallization of fluid hydrogen is supposed to occur much closer to the surface, possibly as high as 0.9 $R_{\rm J}$ (Nellis, 2000).

Jupiter is a fast rotating planet and the oblate shape is easily observed. Flattening, f, which is a measure of ellipticity of a rotating body, is defined as $f = ({\rm a} - {\rm b})/{\rm a}$ where ${\rm a}$ is the equatorial radius and ${\rm b}$ is the polar radius. Rotation is added to the BSCF model (call this model BR) by setting the axis ratio of 0.93, corresponding to the observed flattening value of 0.064 for Jupiter (NASA, 2014). With rotation, the core fractional radius goes back up to $q = 0.69$ in order to make the normalized moment of inertia 0.25 again. This implies that one cannot account for a large core and observed $I_{\rm norm}$ simultaneously without rotation, unless some ad hoc assumptions are also made. The density profiles for all three models (CH, BN and BR) are shown in Figure 4.14.

The external multipole moments or zonal harmonics coefficients J_l of an axisymmetric gravitational potential are defined by

$$U(r,\theta) = -\frac{GM}{r}\left(1 - \sum_{l=2}^{\infty} J_l \left(\frac{R}{r}\right)^l P_l(\cos\theta)\right), r \geq R \tag{4.29}$$

where U is the gravitational potential and $P_l(\cos\theta)$ are the Legendre functions. Inverting this equation, the gravitational coefficients are given by

$$J_l = -\frac{2\pi}{MR^l}\int_0^{\pi}\int_0^{r_{\rho=0}} \rho(r,\theta) P_l(\cos\theta) r^{l+2} \sin\theta {\rm d}r{\rm d}\theta. \tag{4.30}$$

So far, only the values of the first three even zonal coefficients J_2, J_4 and J_6 have been accurately measured for the gravitational field of Jupiter (Jacobson, 2003). These coefficients mainly reflect the rotational distortion of the density distribution of the planet. The first three zonal harmonic coefficients for the BR model are listed along with the percentage error as compared to the measurements in Table 4.1. Notice that the zonal harmonic coefficients match reasonably well to the observed values, given that the BR model is relatively crude with polytropic EoS and only two-layer structure. The work by Guillot (1999) used a detailed three-layer model which takes into account the gravitational as well as the evolution constraints, including atmospheric

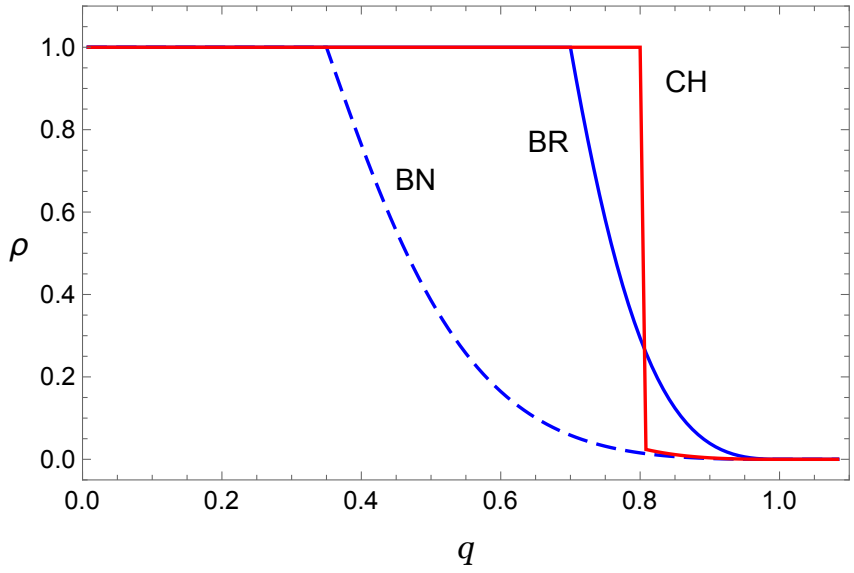

FIGURE 4.14: The normalized equatorial density profile of Jupiter as a bipolytrope. All models have $I_{\rm norm} = 0.25$.

TABLE 4.1: The calculated values of various parameters for the BR model

$I_{\rm norm}$	T (hour)	J_1	J_4	J_6
0.254	$8.21(16)$	$1.29 \times 10^{-2}(12.1)$	$-3.74 \times 10^{-4}(36.3)$	$1.36 \times 10^{-5}(73.9)$

The observed value of $I_{\rm norm}$ is assumed. The percentage errors in the parentheses are calculated with respect to the established values in Jacobson (2003).

abundances and a realistic plasma phase transition EoS. Accuracy in the calculations of gravitational coefficients becomes more important in light of the *Juno* Jupiter orbiter spacecraft, which will perform high precision measurements after arriving at the planet in July 2016 (Kaspi *et al.*, 2010). Although this is the case, the model obtained with the BSCF method attempts to strike a balance between complexity and intuitive understanding. The BSCF method could make better approximations if we take into account the rocky (or icy) core (either as a point mass or another polytrope) and differential rotation of the planet, both of which should affect all of the above calculated values.

The BR model makes a few independent predictions about the physical properties of the planet. For the average density of Jupiter to be $1.33{\rm g/cm^3}$ as observed, the maximum density needs to be $2.72{\rm g/cm^3}$. With this maximum density and the angular velocity obtained with the BSCF method, we calculate the rotational period to be 8.21 hours. This period is a lower limit as the actual central density will be greater than that of the condensed metallic hydrogen core, since the planet is assumed to have a much denser Earth-sized core composed of heavy metals (Guillot, 2005). Similar rotating models can be used to narrow down the possible internal structures of exoplanets. For example, β Pictoris b is a young, gas giant which is observed to be spinning faster than any planet in the Solar System (Snellen *et al.*, 2014). The shape, density distribution, and gravitational zonal coefficients have been calculated for this planet using an $n = 1$ polytropic model (Kong

et al., 2014). Using the BSCF method, better constraints can be put on the structure of this and many other exoplanets. This may also shed light on theories of planetary system formation.

4.4 Bipolytropic Binaries

In this section we consider implementation of the self consistent field method in order to obtain the equilibrium structure of close binary systems rotating synchronously. In the past, the HSCF technique has been used to construct the initial models of detached, close binary systems with a wide range of mass ratios and Roche lobe filling factors (Motl *et al.*, 2002; D'Souza *et al.*, 2006). All of these binary systems had either a polytropic or a zero-temperature white dwarf (ZTWD) EoS for both the stars. Once the rapidly rotating bipolytropic structures are obtained as described in section 4.1, it is relatively straightforward to implement a similar method to generate bipolytropic binary systems. The equations that govern the structure of each star are the same as the ones described in section 4.1 in the context of single bipolytropes. The implementation of the bipolytropic self consistent field method, called BSCF again, closely follows the recipe used in Motl *et al.* (2002).

The steady-state equation of motion (Equation 4.4) for each stellar component, i, in a binary configuration can be written as

$$H + \Phi + \Omega^2 \Psi = C_i. \tag{4.31}$$

The HSCF method required five boundary conditions in order to solve these two equations along with the Poisson's equation. These are $\rho_{max,1}$, $\rho_{max,2}$, the location of the inner boundary of star 1 (A), the location of the outer boundary of the same star (B) and the location of the inner boundary of star 2 (C). Here subscript 1 denotes the star on the right in Figure 4.15, so that two of its boundaries are specified, and 2 denotes the other star. The three points are collinear and lie along the line joining the center of mass of the two stars. In order to obtain a bipolytropic binary, the locations of the boundary points of the core for both the stars (points C and D) also need to be specified. The positions of all five boundary points are depicted in Figure 4.15.

An iterative scheme to solve Equation 4.31, along with Poisson's equation in the BSCF method works as follows. Note that the integration constants $\mathrm{C_i}$ are different for the core and the envelope of each star in general. An initial density distribution satisfying all the outer boundary conditions must be guessed for both the stars. The gravitational potential can be calculated by numerically solving Poisson's equation in the same manner as described in section 4.2. Since the density, and hence the enthalpy, at the surface is forced to vanish, the surface boundary conditions at point A, B and C are

$$H(A) = H(B) = H(C) = 0. \tag{4.32}$$

The envelope integration constant $\mathrm{C_{e1}}$ is the same at points A and B, which allows us to calculate the angular velocity of the binary,

$$\Omega^2 = -\frac{\Phi_\mathrm{A} - \Phi_\mathrm{B}}{\Psi_\mathrm{A} - \Psi_\mathrm{B}}. \tag{4.33}$$

When we put Equation 4.33 back in Equation 4.31 for points A and C, the envelope integration constants for both the stars, $\mathrm{C_{e1}}$ and $\mathrm{C_{e2}}$, can be found.

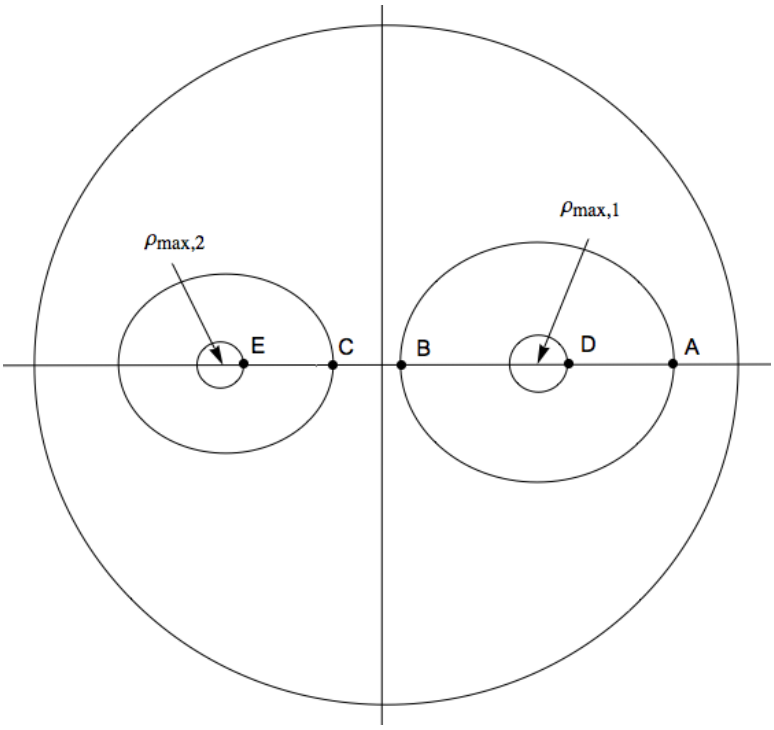

FIGURE 4.15: A schematic showing the boundary points in the equatorial plane that determine the structure of a bipolytropic binary system

Now we are at the same point as Equation 4.12 in section 4.1, where the rotational velocity and the envelope integration constant are known. The new density distribution for each star can be found by following similar steps. The average molecular weights for each core and envelope also need to be specified and these can be different for the two stars. In the next iteration cycle, the axis of rotation is allowed to move to the location of the center of mass of the system along the line joining the center of mass of each star. The centrifugal potential is calculated with respect to this new axis of rotation. The computation is performed for two non-overlapping regions for star 1 and 2, such that each star lies completely inside only one of the regions. The iteration procedure is repeated until the relative changes in $\mathrm{C_{e1}}$, $\mathrm{C_{e2}}$, $\mathrm{H_{max,1}}$, $\mathrm{H_{max,1}}$ and Ω are smaller than a prescribed convergence criterion, δ.

Similar to the HSCF method, the BSCF technique suffers from one major drawback. Although close binaries with a wide range of mass ratios and core mass fractions can be generated using the BSCF technique, physical quantities of interest such as the mass ratio, Roche lobe filling factors and the core mass fractions cannot be specified a priori or controlled precisely. The control parameters $\rho_{max,1}$, $\rho_{max,2}$ and locations of points A through E need to be adjusted through trial and error, to produce systems which have desired properties. There are no analytical solutions for binary bipolytropes (or polytropes) to compare the converged solutions with. However, one way to test the viability of the solutions obtained is to evolve these models in a suitable hydrodynamic code and compare the results with well known semi-analytical expectations.

Chapter 5
Hydrodynamic Evolution

5.1 The Flow-ER Code

Once the equilibrium binary system is generated using the BSCF method, this can be used as a quiet initial condition and can be evolved numerically using a suitable hydrodynamic code. Similar to the BSCF method, we use a grid-based (also known as Eulerian) approach for the hydrodynamic evolution. In simple terms, this implies that the region of interest is divided into a grid, while the fluid is allowed to flow through this grid. In another approach to the computational fluid dynamics, one breaks the fluid into parcels and follows the particles through space. The latter approach is called the Lagrangian method and the well-known Smooth Particle Hydrodynamics (SPH) technique uses a quasi-Lagrangian view. Both approaches have advantages and disadvantages. The Lagrangian method only tracks fluid particles so if the simulation evolves large volumes containing vacuum or very low density voids, no computational power is wasted for them, since there will be no particles at these locations. On the other hand, the Eulerian method can track and resolve low-density fluids better. This is useful if one wants to track low-density matter, for example, the material transferred between two stars in a binary system in order to achieve a lower mass transfer rate.

The hydrodynamic code that we initially use is an explicit, conservative, finite-volume three-dimensional Eulerian code Flow-ER. An elaborate description of the code can be found in Motl (2001) and D'Souza *et al.* (2006). The code is similar to the ZEUS code (Stone *et al.*, 1992) and is implemented on a uniform cylindrical grid. Scalar quantities are defined at cell centers and vector quantities are defined on cell faces. The code tracks the following fluid quantities: mass density (ρ), angular momentum density ($\mathrm{A_m}$), vertical momentum density ($\mathrm{T_m}$), radial momentum density ($\mathrm{S_m}$) and the entropy tracer (τ). The entropy tracer is defined as

$$\tau = (\epsilon\rho)^{1/\gamma}, \tag{5.1}$$

where ϵ is the internal energy per unit mass and γ is the ratio of specific heats. The set of differential equations solved correspond to the conservation laws of these five quantities. The principal equations used for the simulation are as follows. The equation of conservation of mass is

$$\frac{\partial\rho}{\partial t} + \nabla.(\rho\mathbf{v}) = 0, \tag{5.2}$$

where $\mathbf{v}$ is the velocity field. The equations for the conservation of the three components of momentum densities in a reference frame rotating with a constant angular velocity $\mathbf{\Omega}$ are written as

$$\frac{\partial S_m}{\partial t} + \nabla.(S_m\mathbf{v}) = -\frac{\partial P}{\partial R} + \frac{A_m^2}{\rho R^3} + 2\Omega\frac{A}{R}, \tag{5.3}$$

$$\frac{\partial T_m}{\partial t} + \nabla.(T_m\mathbf{v}) = -\frac{\partial P}{\partial z}, \tag{5.4}$$

and

$$\frac{\partial A_m}{\partial t} + \nabla.(A_m \mathbf{v}) = -\frac{\partial P}{\partial \phi} - 2\Omega S_m R, \tag{5.5}$$

where S_m, T_m and A_m are radial, vertical and azimuthal angular momentum densities respectively. The second source term in Equation 5.3 represents the curvature of cylindrical coordinates. The last terms in Equations 5.3 and 5.5 are because of the Coriolis force. The centrifugal force is included in the definition of the effective potential,

$$\Phi_{\rm eff} = \Phi - \frac{1}{2}\Omega^2 R^2. \tag{5.6}$$

For adiabatic flows, $\mathrm{d}s/\mathrm{d}t = 0$, so the entropy tracer, $\tau = (\epsilon\rho)^{1/\gamma}$, evolves according to

$$\frac{\partial \tau}{\partial t} + \nabla.(\tau \mathbf{v}) = 0. \tag{5.7}$$

The entropy tracer is used instead of evolving the internal energy explicitly, as tracking a conserved quantity such as τ is more accurate. The gravitational potential at each timestep is obtained by solving Poisson's equation in the same manner as described in section 4.2. Although the system is evolved adiabatically, the adiabatic EoS, $P = K\rho^{1+1/n}$, cannot be used directly, as the polytropic constant is different for the core and the envelope in general. Hence we use the ideal gas EoS to close the system of equations

$$P = (\gamma_{\rm evo} - 1)\tau^{\gamma_{\rm evo}} = (\gamma_{\rm evo} - 1)\rho\epsilon. \tag{5.8}$$

Here, $\gamma_{\rm evo}$ is the polytropic exponent, also known as the adiabatic exponent, used while evolving the system in time in the hydrodynamic code. This exponent is chosen such that the fluid is convectively stable. The condition for convective instability in terms of adiabatic thermodynamic derivative, $\nabla_{\rm ad}$ (Hansen *et al.*, 2004), is

$$\nabla = \frac{\mathrm{d}\ln T}{\mathrm{d}\ln P} \geq \nabla_{\rm ad} = \left(\frac{\mathrm{d}\ln T}{\mathrm{d}\ln P}\right)_{\rm ad}. \tag{5.9}$$

It is also possible to use scalar fields to calculate an effective adiabatic index at each timestep, however, all simulations in this dissertation are performed using a constant value, $\gamma_{\rm evo} = 1 + 1/1.5 = 5/3$. The outer boundary conditions are outflow and are implemented in such a way that the material is free to move out of the grid, but it is not allowed to move back in from the outermost cells. At the axis of the cylindrical grid, the innermost annulus of cells is averaged in the azimuthal direction at a given layer in the vertical direction. For a detailed description of the treatment of the advection terms, source terms, time centering and numerical tests, see Motl *et al.* (2002).

In general, the initial binary system is detached and the stars do not fill their Roche lobes. Mass transfer between them, however, only occurs when at least one component is in contact with its Roche lobe. A driving mechanism is incorporated in the Flow-ER code such that it artificially removes a certain fraction of specific angular momentum from the system per orbit. This causes a net loss of angular momentum which in turn reduces the separation and brings the components closer to filling their Roche lobe, hence eventually initiating mass transfer. This driving mechanism is turned off at the end of fourth orbit, when a steady mass transfer begins, in the simulations presented here. As we shall see in Chapter 6, in general, the ultimate behavior of the binary is not sensitive to this initial driving.

5.2 The AMR Code Octotiger

For reasons that will become clear in section 5.3, in addition to Flow-ER, we also perform simulations using the code Octotiger with adaptive mesh refinement (AMR). Octotiger is a state of the art, explicit, conservative, fully three-dimensional, Eulerian hydrodynamics code for modeling mass transfer in binary systems. The development of this numerical code is being led by Dr. Dominic Marcello in our research group at LSU. The AMR uses an octree data structure with each internal node having up to eight children, providing twice the resolution in each specific domain. The self-similarity in octree structures provides a relatively simple to implement AMR framework, as compared to other alternatives such as patch-based AMR.

To evolve a binary system over a large number of orbits and replicate realistic behavior, certain key quantities such as the total mass and momentum need to be conserved to high precision. If these quantities are not conserved, the binary system may evolve in an adverse way. Non-conservation of mass, for example, can mimic mass loss from the system, driving the two stars apart. The gravitational force on each element needs to be evaluated during the evolution at each timestep. Grid-based hydrodynamic codes using finite volume methods typically conserve linear momentum or angular momentum, but not both. The direct force method does conserve both linear and angular momentum, however, because of its $\mathcal{O}(N^2)$ complexity, this method is not practical. Octotiger solves Poisson's equation using a modified Fast Multipole Method (FMM) with complexity $\mathcal{O}(N)$ where the potential is computed as a multipole expansion. When implemented on a cartesian grid, numerical advection schemes do not always conserve angular momentum. This is because the symmetry of the stress tensor of the momentum is not conserved in general. Octotiger implements a new scheme (Després & Labourasse, 2014) which conserves linear momentum as well as angular momentum to high precision. The general equation for the conservation of momentum is

$$\frac{\partial \mathbf{s}}{\partial t} + [\nabla.\mathbf{u}]\mathbf{s} + \nabla p = -\rho\nabla\Phi + \mathbf{\Omega} \times \mathbf{s}, \tag{5.10}$$

where the momentum density $\mathbf{s} = \rho[\mathbf{u} + \mathbf{\Omega} \times \mathbf{x}]$, $\mathbf{x}$ is the distance from the axis of rotation, and $\mathbf{u}$ is the velocity field in the non-inertial frame rotating with angular velocity Ω. The code also implements conservation of energy explicitly. The equation for the conservation of total (kinetic, internal and potential) energy is

$$\frac{\partial}{\partial t}[\epsilon + \frac{1}{2}\rho\Phi] + \nabla.\mathbf{u}[\epsilon + p + \rho\Phi] = -\frac{1}{2}[\rho\frac{\partial\Phi}{\partial t} - \Phi\frac{\partial}{\partial t}\rho]. \tag{5.11}$$

The other conservation equations that are numerically solved in Octotiger, conservation of mass and an equation for the entropy tracer, are similar to those in Flow-ER. The treatment of the physical boundary is also similar and the material is allowed to flow out but not back into the grid from the outermost boundary points. Thus Octotiger is able to conserve mass, total energy as well as both linear and angular momenta to machine precision ($\approx 10^{-14}$). This is important for investigating long term, dynamical stability of an evolving binary system. For example, an AM Canum Venaticorum (AM CVn) binary with an initial mass ratio of 0.2 and undergoing stable mass transfer was evolved for over 500 orbits (Marcello et al. 2017, in preparation).

The ideal gas EoS used in Octotiger is identical to that implemented in the Flow-ER code. The major difference between the codes is the energy expression used for the treatment of shocks at high velocities or Mach numbers. There are many situations in astrophysics where due to the hypersonic motion of the gas, the kinetic energy dominates the internal energy of the fluid. In general, the specific internal energy, ϵ, is calculated as

$$\epsilon = E - \frac{1}{2}v^2, \tag{5.12}$$

where E is the specific total energy inside a cell and v is the velocity. In shocks, the very high velocities involved could make calculations of ϵ inaccurate, as $E >> \epsilon$. This does not affect the flow dynamics as the pressure is negligible, however, accurate predictions of temperature are impossible, since it is proportional to the internal energy. Octotiger uses a dual energy formalism to address this issue. The energy expression used iin the EoS is chosen as follows

$$P = \begin{cases} (\gamma_{\text{evo}} - 1)(E - \frac{1}{2}v^2), & \text{if } (E - \frac{1}{2}v^2)/E > \eta \\ (\gamma_{\text{evo}} - 1)\epsilon, & \text{otherwise,} \end{cases} \tag{5.13}$$

where η is a prescribed small parameter. In our simulations, this η equals 10^{-3}. The specific internal energy is calculated from evolving the entropy tracer, τ, similar to the implementation Flow-ER. Thus Flow-ER evolves adiabatically with an ideal gas EoS, while Octotiger takes shock heating into account and uses the dual energy formalism with an ideal gas EoS. Apart from the AMR, the calculation of the pressure is the only major difference between Flow-ER and Octotiger in terms of comparing the outcome of simulations from the two codes. The inclusion of shock heating will cause the outer regions of the envelope to expand in Octotiger simulations.

Octotiger is implemented in C++ and parallalized using the High Performance parallaX (HPX) runtime system developed in collaboration with the Ste||ar[1] (Systems Technology, Emergent Parallelism, and Algorithm Research) group at the Center for Computation & Technology (CCT) at the Louisiana State University. HPX allows efficient use of computational resources through better scaling and performance as compared to more conventional programming models such as MPI (Message Passing Interface). HPX enables scaling the code to thousands of cores without suffering from conventional computing bottlenecks. This allows us to take full advantage of the raw computing power of large supercomputers.

The use of AMR in Octotiger enables us to put resolution where it is needed. The total size of the computational domain that Octotiger can handle is also significantly larger than what we could previously achieve with Flow-ER, which uses a static cylindrical grid. For example, in order to simulate twice as much distance in each direction with a static grid, the number of cells required increases by a factor of 2^3. With AMR, however, as each additional level of refinement needs an addition of 8^4 more cells. Thus the increase in the computational requirements is linear, making simulations with large spatial ranges much more economical.

5.3 Test Simulations with Flow-ER and Motivation for using AMR

As described in section 4.2, we have several methods for verifying single bipolytropic models obtained using the BSCF method. However, there are no known analytical methods for testing

[1] http://stellar.cct.lsu.edu/about/

binary solutions obtained where each component is a bipolytrope. One way to address this issue is to perform benchmark simulations of non-interacting binary systems as a test of hydrostatic equilibrium using a suitable hydrodynamic code. We started our investigations with the Flow-ER code because this computational tool is extensively tested and produces reliable results for mass transfer scenarios involving polytropes (Motl *et al.*, 2002; D'Souza *et al.*, 2006). This section describes the limitations of the Flow-ER code while performing simulations involving bipolytropic stars and why we need an AMR capable code, such as Octotiger.

The first test that we conducted was to simulate a single bipolytropic star with the center of mass located at the center of the grid in Flow-ER. This is similar to the test performed in Motl *et al.* (2002) in order to confirm the coupled solution of Poisson's equation with the hydrodynamical equations. Here we use the same technique to test whether the configuration obtained via the BSCF method is in hydrostatic equilibrium. For dynamical stability, the configurations also needed to have convective stability as described by Equation 5.9, with higher-entropy fluid lying above lower-entropy fluid. With a polytropic EoS, this means that the polytropic index of the core needs to be higher than the envelope. We evolved a set of such configurations using Flow-ER, and in conclusion, all the bipolytropic stars were dynamically stable. For example, in one particular case, the biploytropic configuration chosen possessed $(n_c, n_e) = (3, 1)$ and $\alpha = 2$ on a grid with resolution of $\mathrm{NUMR} \times \mathrm{NUMZ} \times \mathrm{NUMPHI} = 130 \times 130 \times 256$. The core resolution was chosen to be 20 cells in R-direction, which is comparable to the core resolution in a binary simulation. The results are consistent with our expectations that the bipolytropic star remains near hydrostatic equilibrium, especially with respect to the central or the maximum density, $\rho_{\max}$. The maximum density on the grid remained near the initial value of unity over several dynamical times and the maximum amplitude of the variations in $\rho_{\max}$ was less than 1%.

The next step was to test the behavior of a non-interacting bipolytropic binary systems, in order to confirm the correct implementation of the BSCF method in a binary system. The time evolution in Flow-ER was carried out in a frame corotating with the initial angular velocity of the system. This minimized the effects of numerical diffusion due to the finite accuracy of the advection scheme. Although the BSCF method is carried out in a grid native to the hydrodynamic code, as explained in section 4.4, the center of mass is allowed to drift along the line joining the two stars. Hence if $q \neq 1$, the axis of rotation does not lie at the axis of the cylindrical grid. Motl *et al.* (2002) showed that if a system is evolved with the center of mass away from the axis of the grid, it drifts outwards as if acted upon by a constant, resolution-dependent force in the corotating frame. The solution is to transport the fields from the BSCF grid to the Flow-ER grid such that the initial axis of rotation obtained via the BSCF method coincides with the coordinate axis of the hydrodynamics code as closely as possible. This translation is performed using a bicubic interpolation scheme described in Press *et al.* (1986). We chose to use a mass ratio of unity for the purpose of testing the hydrodynamic stability of the bipolytropic binary systems. This eliminated the intermediate step of translating the initial density field and a converged model obtained through the BSCF method can be directly used in Flow-ER without further processing.

We conducted the first test simulation of a detached bipolytropic binary with each component being a bipolytrope with $(n_c, n_e) = (3, 1)$, $\alpha = 2$. The first anomaly that we noticed with this simulation is that the central densities of both the stars dropped by a large factor in the first few orbits (see blue curve in Figure 5.1). Although other important parameters such as angular

momenta, mass and total volume behave in an expected manner, this drop in the central density was alarming. This behavior could mean an incorrect implementation of the BSCF method in a binary or an unforeseen artifact due to the limitations of the numerical methods used in the Flow-ER hydrodynamic code, or both. In order to investigate this issue further, we decided to conduct a suite of simulations. The test runs, described in the remainder of this section with a mass ratio of unity, are called "Q1" simulations for convenience. The goal was to find a trend or correlation between the properties of the initial bipolytropic models and their dynamical behavior in Flow-ER. We varied the following model parameters which describe the physical attributes of the core of the initial bipolytropic models obtained through the BSCF method.

1. Core polytropic index, $n_{\rm c}$.

2. Molecular weight ratio, α.

3. Coresize in number of cells in the azimuthal direction.

In order to quantify the effects of model parameters on the time evolution, we measured certain properties of each initial BSCF model with a given combination of model parameters, i.e. $n_{\rm c}$, α and coresize. These are called indicator parameters.

1. Full width at half maximum (FWHM) of the core normalized with respect to the stellar radius. This is a measure of the relative width of the core.

2. Average slope of the core density normalized with respect to the initial stellar radius and initial maximum density on the grid. This is a measure of the average gradient of the density field in the core.

3. A resolution dependent peak parameter defined as

$$\text{peak parameter} = \frac{\left|\frac{\rho(i)-\rho(i-5)}{5}\right| + \left|\frac{\rho(i)-\rho(i+5)}{5}\right|}{2}, \tag{5.14}$$

   where i is the index of maximum density in the radial direction. This is the average value of the slope in both directions, towards and away from the axis, near the density maximum.

4. Virial error of the converged BSCF model. Defined by Equation 4.20, this is a global measure of the accuracy of the equilibrium of a non-linear dynamical system.

In order to quantify the temporal behavior, the maximum density was measured on the grid after the binary completed one orbit in the hydrodynamic code ($\rho_{\rm max,1}$). In the Q1 simulations, we did not distinguish between the central densities of the two stars, instead, we used the maximum density on the grid. This is because both the stars were initially identical and the numerical differences between the central densities were much smaller compared to the fall in $\rho_{\rm max,1}$. We measured the correlation between the indicator parameters and $\rho_{\rm max}$, as the binary systems with different model parameters evolved in the hydrodynamic code. Other properties of each bipolytrope in a binary were kept constant throughout the Q1 simulations.

Figures 5.1 to 5.3 show the time dependent behavior of the maximum density as we vary each of the three model parameters – $n_{\rm c}$, α and coresize, while keeping the other two fixed. Tables 5.1 to 5.3 report the values of the indicator parameters for the initial models used in these simulations as well as $\rho_{\rm max}$ after one orbit. We will describe these tables in detail later in this section. Consider Figure 5.1, which shows the evolution of $\rho_{\rm max}$ for different core polytropic indices. Note that the greater the core polytropic index, the more ρ_{max} diverges from the expected value of unity. The values of the indicator parameters are listed in Table 5.1. Other relevant parameters that were held constant for these runs are – $n_e = 3/2$, $\alpha = 2$, size of the core and envelope in R-direction (21 and 94 cells respectively) and $\gamma_{evo} = 5/3$.

Figure 5.2 shows the time dependent behavior of the maximum density for different ratios of the average molecular weights between the core and the envelope. Here we observe that the increase in α from 1 to 2 does not affect the evolution of ρ_{max} significantly, however, a further increase in α causes larger deviations from unity. The values of the indicator parameters are listed in Table 5.2. Other relevant parameters that were held constant for these runs are – $(n_c, n_e) = (3, 3/2)$, size of the core and envelope in R-direction (21 and 94 cells respectively) and $\gamma_{evo} = 5/3$.

Finally, Figure 5.3 shows the time dependent behavior of the maximum density for different coresizes. Here the coresize is reported as the number of cells the core occupies in the azimuthal direction. The values of the indicator parameters are listed in Table 5.3. Other relevant parameters that were held constant for these runs are – $(n_c, n_e) = (3, 3/2)$, $\alpha = 2$, size of the envelope in R-direction (94 cells) and $\gamma_{evo} = 5/3$.

In the case of continuous polytropes, Flow-ER can follow the hydrodynamic evolution of binary stars with high precision. Ideally there should be no detectable deviation of $\rho_{\rm max,1}$ from the initial value of unity, as the stars evolve in Flow-ER. For the Q1 simulations, however, there was a considerable fall of $\rho_{\rm max}$ after the first orbit for most of the test cases. In this analysis we assume that the properties of the initial bipolytropic models are responsible for this anomalous dynamical behavior of the binary. In Figure 5.4 we plot $\rho_{\rm max,1}$ versus indicator parameters from Tables 5.1 to 5.3. Note that the indicator parameters are normalized with respect to the maximum. The variability or the average size of the error bars for all of the data points is of the order of 2%, as can be concluded from the small amplitude oscillations in ρ_{max} in Figures 5.1 to 5.3. Consider the data for FWHM, which is the red curve in Figure 5.4. As the value of FWHM increased from the left to right, $\rho_{\rm max,1}$ did not increase monotonically, but showed large variations. Similarly the virial error and the average slope of the core also did not show a clear trend. We conclude that FWHM, VE or the average slope did not correlate well with $\rho_{\rm max,1}$ and they did not reflect the reason for the decrease in the maximum density. Consider next the case of the peak parameter, which is the black curve in Figure 5.4. As the peak parameter increased from left to right, the plot showed an ideal behavior of $\rho_{\rm max,1}$, but only up to a certain threshold of peak parameter. After this threshold, $\rho_{\rm max,1}$ started decreasing monotonically, and almost linearly, as the peak parameter increased. Note that as defined through Equation 5.14, the peak parameter is a measure of the absolute slope of the core near the maximum value, and it is not normalized with respect to a length scale. Thus we hypothesize that the fall in the central density is caused by a large gradient near the maximum in the density distribution, which is reflected in high values of peak parameter.

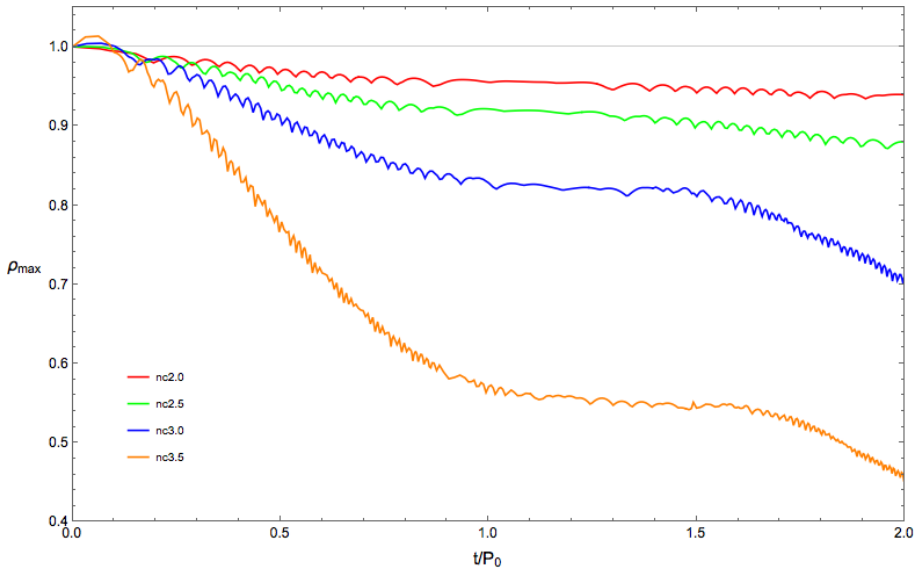

FIGURE 5.1: Effect of core polytropic index on the maximum density.

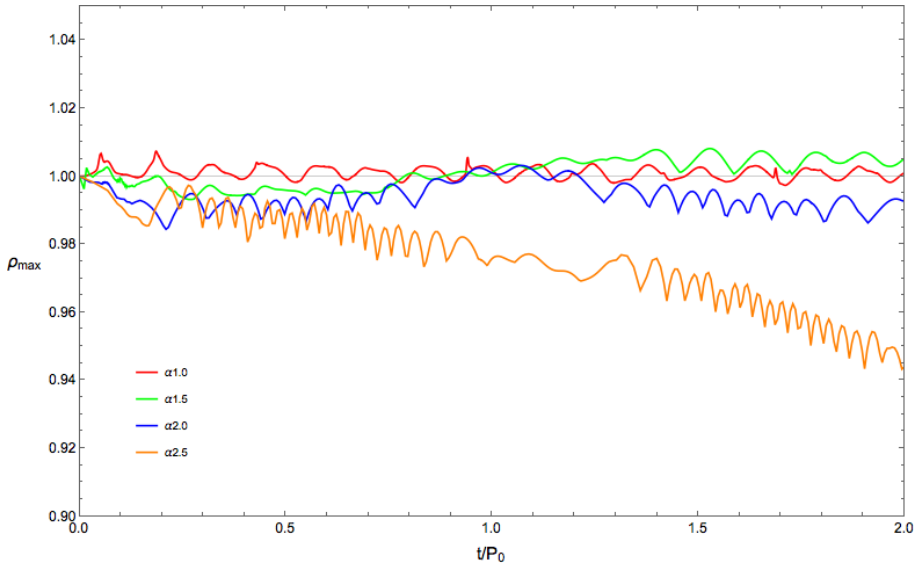

FIGURE 5.2: Effect of the jump in molecular weight on the maximum density.

TABLE 5.1: Effect of core polytropic index on the evolution of the maximum density.

Model ID	n_c	FWHM	Average slope of the core	Peak parameter	VE	$\rho_{\max,1}$
nc2.0	2.0	0.2989	2.8807	4.5592×10^{-2}	2.3866×10^{-3}	0.9551
nc2.5	2.5	0.2725	3.1863	6.1000×10^{-2}	2.6694×10^{-3}	0.9213
nc3.0	3.0	0.2396	3.4312	8.0696×10^{-2}	3.1221×10^{-3}	0.8280
nc3.5	3.5	0.1978	3.6215	1.0805×10^{-1}	3.6187×10^{-3}	0.5709

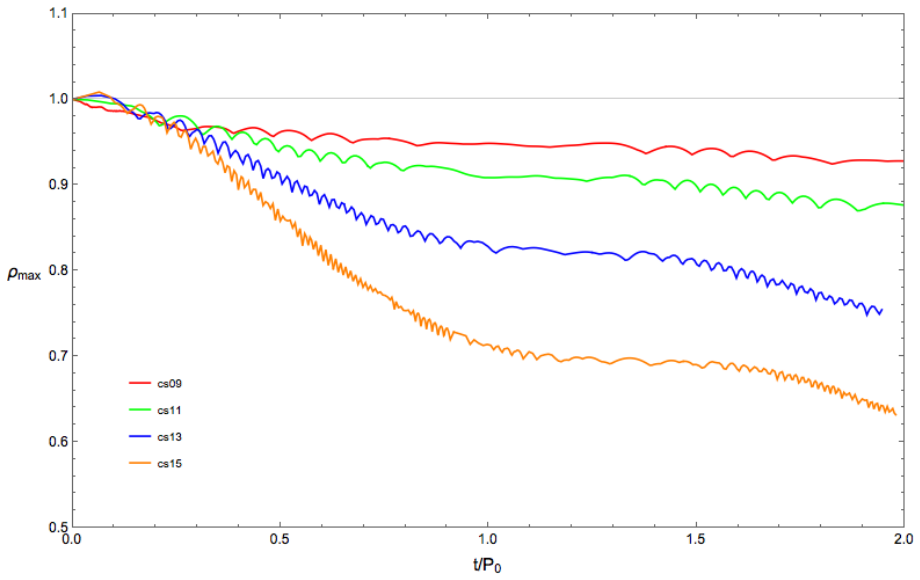

FIGURE 5.3: Effect of the core-size on the maximum density.

TABLE 5.2: Effect of the jump in the molecular weight on the evolution of the maximum density.

Model ID	α	FWHM	Average slope of the core	Peak parameter	VE	$\rho_{\max,1}$
α1.0	1.0	0.3604	0.8406	8.5018×10^{-3}	4.8933×10^{-4}	1.0018
α1.5	1.5	0.3472	1.6960	1.9205×10^{-2}	8.6940×10^{-4}	1.0012
α2.0	2.0	0.3275	2.4915	3.2689×10^{-2}	1.9414×10^{-3}	1.0009
α2.5	2.5	0.3099	3.0099	4.5041×10^{-2}	2.9816×10^{-3}	0.9759

Figure 5.5a depicts the equatorial cross section of density of a bipolytropic star placed in a cylindrical grid. As compared to a star placed at the center of the cylindrical grid, the effective resolution in the azimuthal direction of a star placed away from the axis decreases sharply and keeps getting worse as the star moves farther from the axis. The core in a bipolytropic star is especially affected by this degradation because of its relatively small size. The drop in central density is similar to the phenomenon of numerical diffusion wherein the simulated fluid exhibits higher diffusivity than a real gas. Numerical diffusion arises from the finite accuracy of Eulerian advection schemes and is not related to the initial models obtained via the BSCF method. The FWHM and average slope of the core density are not good indicators of this diffusion, since they are a measure of the extent of the entire core, and not just near the center. In conclusion, the results of the Q1 test simulations can be summarized as follows. Both the initial bipolytropic models obtained through the BSCF method, and the implementation of numerical techniques in Flow-ER are correct. The fall in the central densities of the components in a bipolytropic binary system is a result of the insufficient resolution of their core in the azimuthal direction.

The decrease in $\rho_{\max}$ previously did not occur in the Flow-ER simulations because all the initial models possessed a continuous polytropic structure. The continuity conditions at the core-

TABLE 5.3: Effect of core-size on the evolution of the maximum density.

Model ID	Core-size	FWHM	Average slope of the core	Peak parameter	VE	$\rho_{\max,1}$
cs09	9	0.2176	3.0994	5.6042×10^{-2}	1.4682×10^{-3}	0.9486
cs11	11	0.2330	3.5480	7.0452×10^{-2}	1.2866×10^{-3}	0.9086
cs13	13	0.2374	3.4312	8.0696×10^{-2}	3.1248×10^{-3}	0.8231
cs15	15	0.2417	3.0892	8.2481×10^{-2}	4.0073×10^{-3}	0.7128

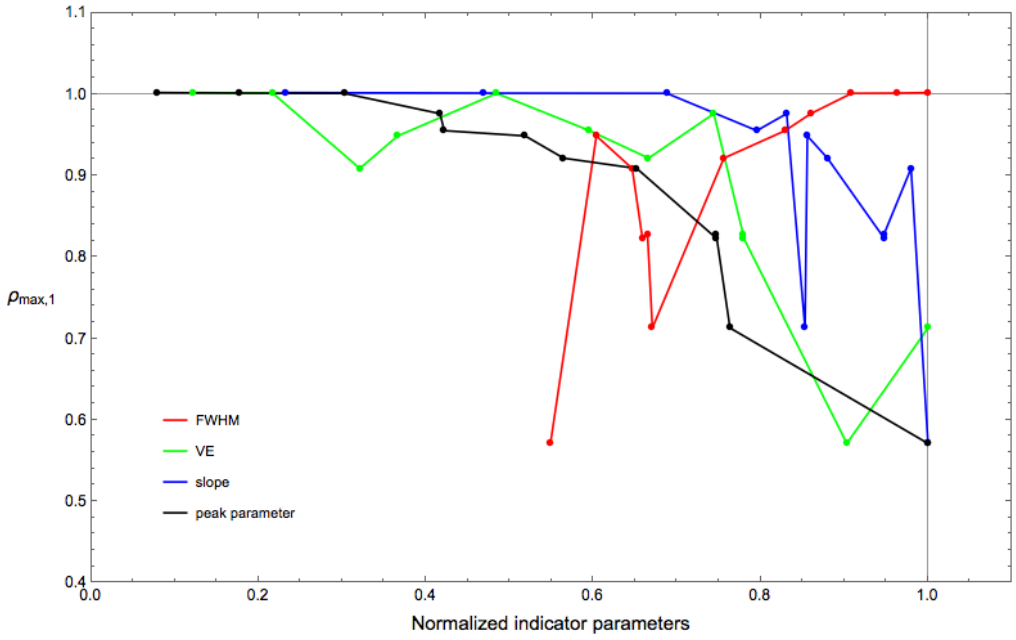

FIGURE 5.4: Maximum density after the first orbit vs normalized indicator parameters.

envelope boundary force the gradients in the core to be higher than a continuous polytrope, at a given stellar radius (compare the density profiles of polytropes in Figure 3.1 to that of a bipolytrope in Figure 3.3). This gradient is made even larger by the choice of a larger polytropic index. The cylindrical geometry, native to the Flow-ER code, worsens the situation in the azimuthal direction. It is possible to mitigate the adverse effect of the numerical diffusion by increasing the resolution, say, by doubling it in all three directions. As described in section 5.2, the computational cost of increasing resolution increases geometrically by a factor of $2^3 = 8$. In addition, the timestep during the advection scheme also decrease by a factor of 4. This is because with the cylindrical geometry, the timestep is proportional to both $\mathrm{d}\phi$ and $\mathrm{d}R$ near the axis. This means that doubling the resolution in all three directions in Flow-ER could be up to 32 times computationally more expensive. Thus an AMR capable code is a much better choice for simulating bipolytropic binary systems.

As an example, Figure 5.5 shows the improvement in core resolution after implementing one particular bipolytropic binary system in Octotiger (CylLR and OctLR simulations are described in section 6.2). The figure shows horizontal cross sections of the density field in the cylindrical as

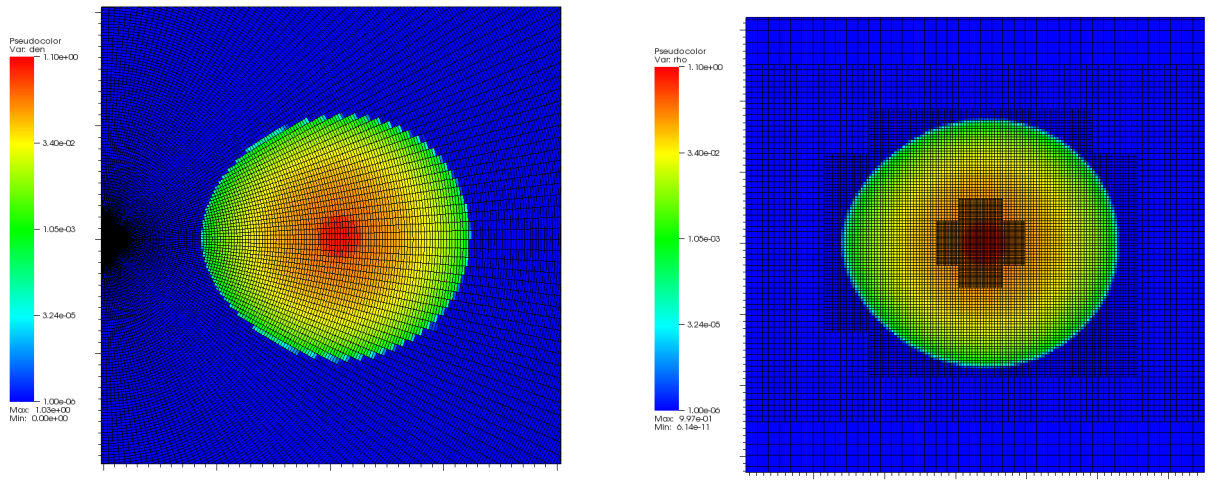

(a) CylLR (b) OctLR

FIGURE 5.5: The improvement in the resolution of the core of a bipolytropic star with the AMR grid as compared to static cylindrical grid.

well as the AMR grid. The core occupies only 9 cells in the azimuthal direction in the cylindrical geometry and 32 cells in the Cartesian AMR geometry. The AMR grid also allows us to put resolution where it is needed, making the computations much more efficient. We discuss the evolution of bipolytropic binaries across both codes, as well as at increased resolution in the next chapter.

Chapter 6

Mass Transfer Simulations of Bipolytropic Binaries

In this section we present the results from a suite of bipolytropic binary simulations conducted using the two codes – Flow-ER and Octotiger. This set of four benchmark simulations is called Q0.7, since all the simulations started with an initial mass ratio, $q_0 \approx 0.7$. The initial conditions of all four simulations were chosen to match as closely as possible. In section 6.1 we describe our choice of the initial bipolytropic models obtained using the BSCF technique, and in section 6.2 we examine the time evolution and interpret the results obtained from the simulations.

6.1 The Initial Model

Our initial bipolytropic binary models followed the conclusions from Stępień (2006), that W UMa type systems are old and and have experienced a previous Algol-like mass ratio reversal (see section 2.2.2). In the benchmark simulations presented in this chapter, we tried to match the observed and inferred properties of a contact binary system as closely as possible, while still working within the limitations of the Flow-ER code. The Q0.7 simulations were carried out with both the codes, Flow-ER and Octotiger, at two different resolutions (see Table 6.1, explained later in this section). We tried to match the properties of the initial binary model for both codes, and at high and low resolutions. In this section we justify our choice for selecting this particular binary model with a specific mass ratio, initial period and internal structure.

Table 6.1 lists the resolutions used to carry out the Q0.7 simulations. The prefix "cyl" or "oct" denotes the code used (Flow-ER or Octotiger respectively) and postfix "LR" or "HR" denotes the use of low or high resolution respectively. The cylLR model had a grid resolution of $\mathrm{NUMR} \times \mathrm{NUMZ} \times \mathrm{NUMPHI} = 258 \times 130 \times 256$. In the cylHR model, the resolution of the stars was doubled by doubling the location of the five boundary points specified for the BSCF method. The total resolution of cylHR model was $\mathrm{NUMR} \times \mathrm{NUMZ} \times \mathrm{NUMPHI} = 386 \times 258 \times 512$. The AMR grid changes dynamically in Octotiger according to the matter distribution, hence we specify only the initial effective resolution of each simulation. The AMR implemented in Octotiger is based on octree data structure, where each node is divided into 8^3 subgrids. Thus as shown in Table 6.1, the initial effective resolution for an Octotiger simulation is obtained by multiplying the total number of nodes by 8^3, which equals the total number of cells on the grid. The model in octHR had two more levels of refinement as compared to octLR, while the total computational grid was also increased by a factor of two. This effectively doubled the resolution of the cores of both the donor and the accretor. For comparison, the core resolutions are listed in Table 6.1. In the case of the Flow-ER code, the core resolution is specified as the number of cells in the radial and the azimuthal direction, and in the case of Octotiger, the core resolution is specified as the number of cells in the X and Y direction. The relative sizes of the computational domains of the grids for all four simulations are visualized in Figures 6.1 and 6.2.

The initial values of the bipolytropic binary system parameters are listed in Table 6.2. Here a subscript D denotes the donor, A denotes the accretor, c denotes the core and e denotes the

TABLE 6.1: Simulation Resolutions

Model ID	Resolution[1]	Core Resolution[2]		Notes
		Donor	Accretor	
cylLR	$258 \times 130 \times 256 \approx 8.6$ M	15×11	17×7	
cylHR	$386 \times 258 \times 512 \approx 51$ M	30×14	34×22	
octLR	$7721 \times 8^3 \approx 3.9$ M	32×32	34×35	8 levels of refinement
octHR	$32841 \times 8^3 \approx 17$ M	64×64	68×68	10 levels of refinement

[1]The resolution in the cylindrical grid is specified as $\mathrm{NUMR} \times \mathrm{NUMZ} \times \mathrm{NUMPHI}$. The initial resolution in the AMR grid is specified as total number of grid cells obtained by multiplying the total number of nodes by 8^3 subgrids.
[2]The core resolution for cylindrical grid is in terms of the number of cells in R and ϕ direction, and that for AMR grid is the number of cells in X and Y direction.

envelope. The quantities listed in this table are– mass (M), radius (R), maximum density ($\rho_{\max}$), core mass fraction ($M_{\rm c}/M$), polytropic constant of the core ($K_{\rm c}$) and the envelope ($K_{\rm e}$) for each of the components, along with the mass ratio (q), the Roche lobe filling factor (Rlff), separation (a), period (P), virial error (VE) and the minimum density on the grid at the beginning of simulation ($\rho_{\min}$). The Rlff is defined in terms of the ratio of the volume of the component above a density threshold of 10^{-5} to the volume of its Roche lobe. The calculations were performed in dimensionless "code units", normalized with respect to the maximum density, radius of the cylindrical grid used in the BSCF method, and the gravitational constant. In the case of the Q0.7 simulations, all three normalizing quantities were assigned a value of unity. Assuming a primary with solar mass and radius, the properties of the initial binary can be calculated in solar units, which are listed in Table 6.3. We constructed initial binary models that closely match each other, however, one may notice that they are not identical. Although it is possible to precisely control the input parameters via the locations of the five boundary points specified in the BSCF method, the slight difference in the initial models should not affect the results. The initial models were also different because the accuracy of the converged solution depends on the resolution. The departure from equilibrium tends to converge to zero with the increase in resolution.

We conducted the benchmark simulations with a mass ratio, $q_0 \approx 0.7$, because if the initial mass ratio at the start of the mass transfer is between certain critical values (the case 2 as explained later in section 6.2.2) the outcome of the simulation may depend on the degree of initial contact between the donor and its Roche lobe (Motl *et al.*, 2017a). We do not accurately control this degree of contact at the end of the driving phase. Hence in order to ensure agreement of the qualitative outcome across all four simulations, we chose $q_0 \approx 0.7$. Another reason for our choice is that this particular mass ratio was well studied in our research group with polytropic EoS. Thus we can compare the results of this study with existing simulations.

The initial mass of the primary as well as the secondary component was consistent with a low-mass zero-age main sequence (ZAMS) star, below about $1.3\mathrm{M}_{\odot}$. Such a star possesses a convective envelope, which allows magnetic braking to remove angular momentum and form a contact configuration. Figure 6.3 shows the mass-radius relation for contact binaries for a total

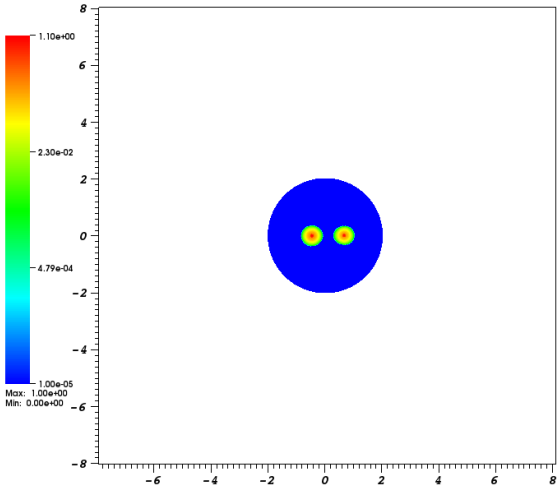

(a) cylLR

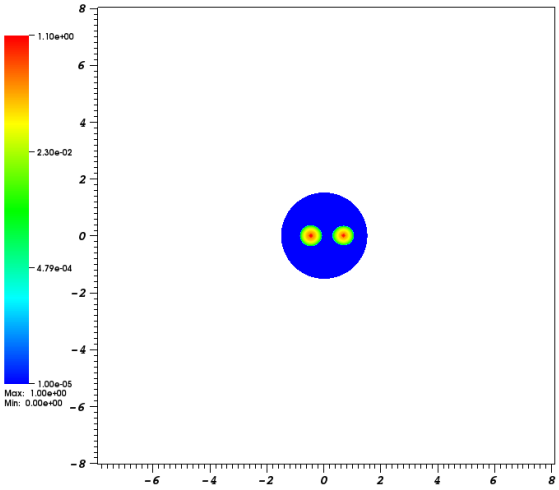

(b) cylHR

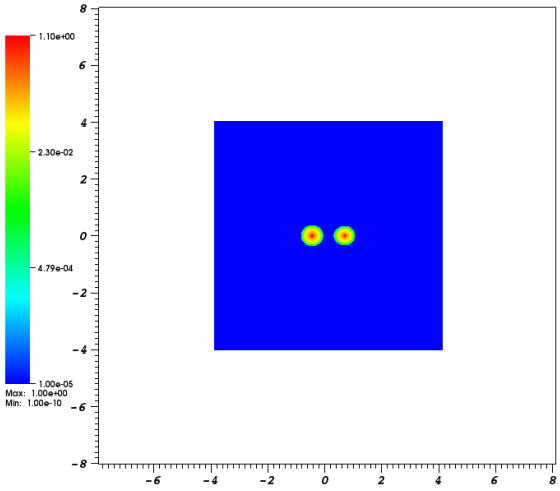

(c) octLR

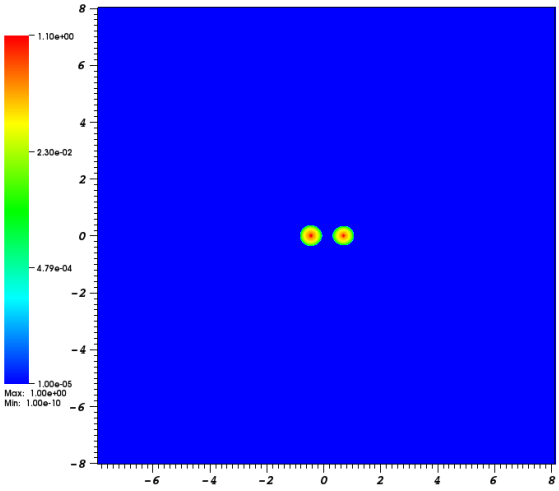

(d) octHR

FIGURE 6.1: Equatorial cross section of the initial density field in the four Q0.7 simulations. The blue section represents the size of the computational domain.

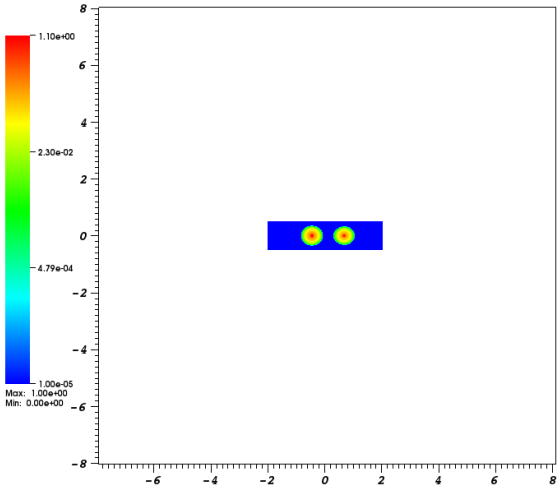

(a) cylLR

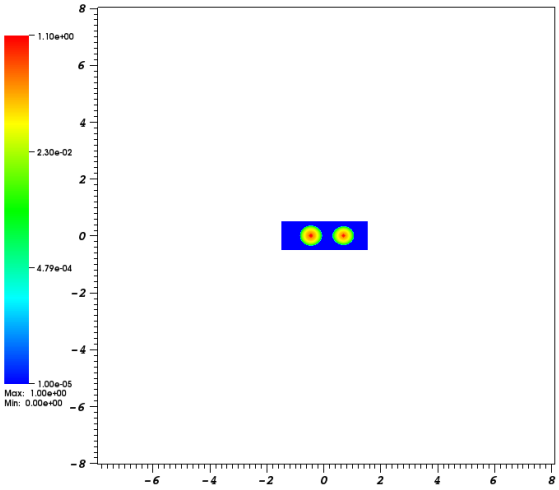

(b) cylHR

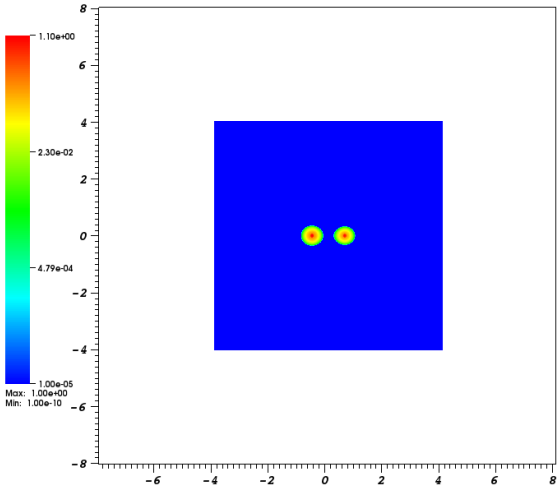

(c) octLR

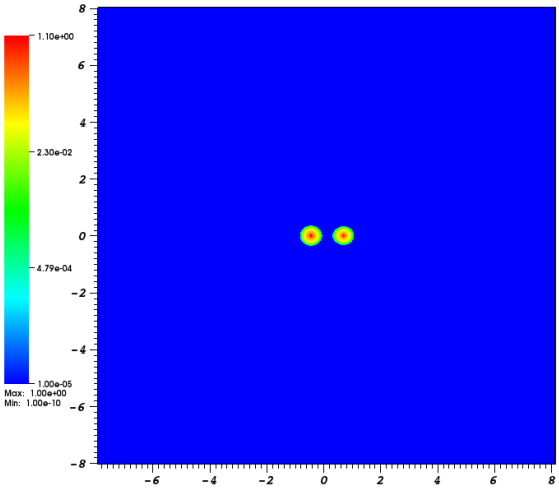

(d) octHR

FIGURE 6.2: Meridional cross section of the initial density field in the four Q0.7 simulations. The blue section represents the size of the computational domain.

TABLE 6.2: Initial bipolytropic binary system parameters in code units

Parameter[1] / Model ID	cylLR	cylHR	octLR	octHR
q	0.7022	0.6971	0.6765	0.6936
$M_{\rm D}$	5.702×10^{-3}	5.485×10^{-3}	5.468×10^{-3}	5.456×10^{-3}
$R_{\rm D}$	0.3493	0.3502	0.3496	0.3492
$\rho_{\rm max,D}$	0.8140	0.8360	0.8140	0.8140
$(M_{\rm c}/M)_{\rm D}$	0.08263	0.09784	0.09920	0.09857
$K_{\rm c,D}$	6.595×10^{-3}	6.519×10^{-3}	6.476×10^{-3}	6.621×10^{-3}
$K_{\rm e,D}$	2.807×10^{-2}	2.814×10^{-2}	2.798×10^{-3}	2.860×10^{-3}
$\rm Rlff_D$	0.6981	0.6947	0.8684	0.6887
$M_{\rm A}$	8.121×10^{-3}	7.868×10^{-3}	8.082×10^{-3}	7.866×10^{-3}
$R_{\rm A}$	0.3706	0.3714	0.3739	0.3705
$\rho_{\rm max,A}$	1.000	1.000	1.000	1.000
$(M_{\rm c}/M)_{\rm A}$	0.09001	0.09850	0.09913	0.09843
$K_{\rm c,A}$	8.418×10^{-3}	8.310×10^{-3}	8.538×10^{-3}	8.320×10^{-3}
$K_{\rm e,A}$	3.384×10^{-2}	3.381×10^{-2}	3.473×10^{-3}	3.384×10^{-3}
$\rm Rlff_A$	0.5146	0.5079	0.6394	0.4941
a	1.134	1.141	1.140	1.141
P	64.15	66.00	65.51	66.15
VE	1.729×10^{-3}	4.968×10^{-4}	2.081×10^{-4}	2.698×10^{-4}
$\rho_{\rm min}$	1.000×10^{-10}	1.000×10^{-10}	1.000×10^{-10}	1.000×10^{-10}

[1]The subscripts D, A, c and e stand for donor, accretor, core and envelope respectively.

mass below $2\rm M_\odot$, observed by Maceroni & van 't Veer (1996). The primary and the secondary components approximately follow the ZAMS and terminal-age main sequence (TAMS) relationships respectively. Assuming the more massive accretor possessed a mass of $1\rm M_\odot$ and a radius of $1\rm R_\odot$, the initial models in the Q0.7 systems were consistent with the observed relations. The initial period for all of the Q0.7 binary systems was between 11.3 and 11.5 hours. Figure 6.4 shows the period of the Q0.7 binaries, along with the period distribution of 11,076 eclipsing binary systems discovered via the All Sky Automated Survey (ASAS) project (Li *et al.*, 2007). Note that the Q0.7 binary systems lie at the tail end of detached binaries and closer to the peak corresponding to the distribution for the contact binary systems, about 8.4 hours. When the binary system is driven closer, the period will decrease at the beginning of the mass transfer. As we shall see in the next section, these binaries do not form a contact configuration and end up merging. This is consistent with our theoretical expectations for the given internal structure and mass ratio, which are explained in detail in section 6.2.2.

Each of the components in the initial Q0.7 models were far from filling their Roche lobes. The initial Roche lobe filling factors (Rlff) for the primary and secondary components are about 50% and 70% respectively. This is because with the BSCF method as discussed in section 4.4 with five spatial boundary points specified, we cannot precisely control the Roche lobe filling factors. The binary is essentially generated using a trial and error method to produce a system which is reasonably close to what we desire. We artificially remove angular momentum which causes the

TABLE 6.3: Initial bipolytropic binary system parameters in solar units

Model ID	cylLR	cylHR	octLR	octHR
$M_{\rm tot}$	1.702	1.697	1.676	1.694
$M_{\rm A}$	1.000	1.000	1.000	1.000
$R_{\rm A}$	1.000	1.000	1.000	1.000
$M_{\rm D}$	0.7022	0.6971	0.6765	0.6936
$R_{\rm D}$	0.9425	0.9430	0.9351	0.9426
a	3.060	3.073	2.687	3.082
P(hour)	11.34	11.45	11.41	11.52

binary separation to shrink. Eventually the component with the higher Rlff, in the case of Q0.7 simulations the lower mass star, makes contact with its Roche lobe thus beginning the mass transfer.

In the case of V1309 Sco, in the final stages both the components possessed a small hydrogen depleted core with a mass of about 10% of the total mass (Stępień, 2011). Both the components in the Q0.7 models also had a core mass fraction of about 9% (Table 6.3), so that we can investigate the dynamical behavior of the core of the donor as the two stars interact. The choice of the EoS or the polytropic indices for the Q0.7 models is affected by the limitations of the code Flow-ER. The helium core of a star near TAMS is expected to be isothermal, hence a softer EoS with a large polytropic index is more suitable. This, however, would make the density gradients near the center larger. As discussed in section 5.3, steep gradients of the density near the maximum result in the fall of the central density (e.g. see Figure 5.1). Thus we made a moderate choice of $(n_c, n_e) = (3, 3/2)$, which is more suitable for a radiative core and a convective envelope. The gradient of the central density also increases with increasing ratio of average molecular weights, α, at the core-envelope interface. Although in the case of the Flow-ER code, Figure 5.2 suggests a marginal effect on the fall in the central density with α, the actual behavior depends on the choices of the polytropic indices. For a fully ionized helium core and a solar composition envelope, the ratio of average molecular weights equals 2.22. Given our choices of $(n_c, n_e) = (3, 3/2)$, the $\alpha = 2.22$ model behaved significantly worse as compared to $\alpha = 2$ in terms of the central density, hence we selected the latter value for the Q0.7 simulations.

6.2 The Hydrodynamic Evolution of Q0.7 Binaries

After obtaining the initial binary systems through the BSCF method, we used these models as quiet initial conditions for the hydrodynamic codes. The subsequent evolution of the binary was treated without any special assumptions or symmetries. We carried out four simulations of bipolytropic binaries – two simulations are conducted using the code Flow-ER (cylLR, cylHR) and the other two are conducted using Octotiger (octLR, octHR). The initial conditions were chosen to match closely, so that we can expect an agreement in the dynamical behavior of these systems as well as the ultimate outcome. As explained in section 5.2, Flow-ER evolves adiabatically with an ideal gas EoS, while Octotiger takes into account shock-heating and uses the dual energy formalism with an ideal gas EoS. The flow dynamics of the binary systems during mass transfer are not expected to be affected by these differences, however, as we shall also confirm in this section, the two codes did show subtle differences in the dynamical evolution.

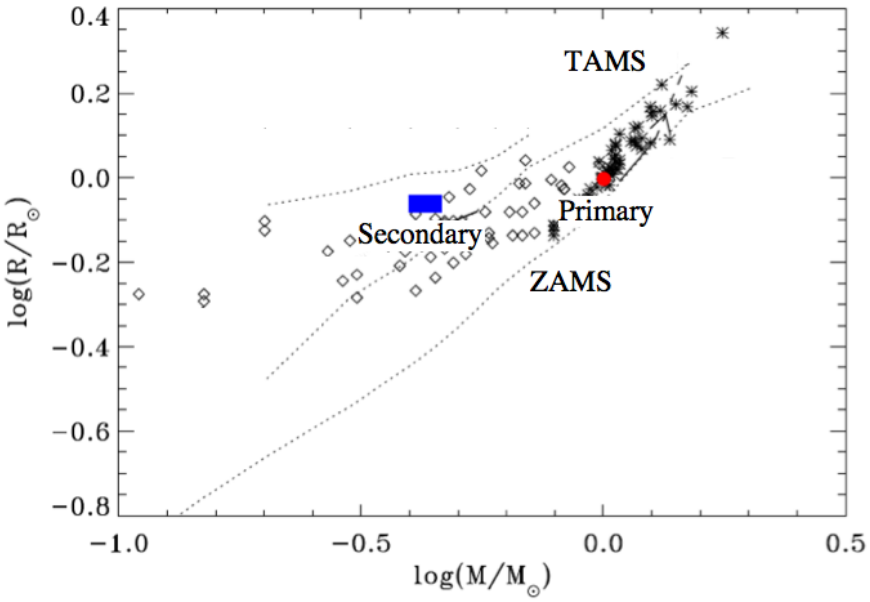

FIGURE 6.3: The observed mass-radius relation of W UMa type binaries (Stępień, 2006). Asterisks correspond to more massive primary component and diamonds correspond to the secondary. The red circle denotes the primary component in all Q0.7 simulations, assuming solar mass and radii. The secondaries are confined to the blue rectangle.

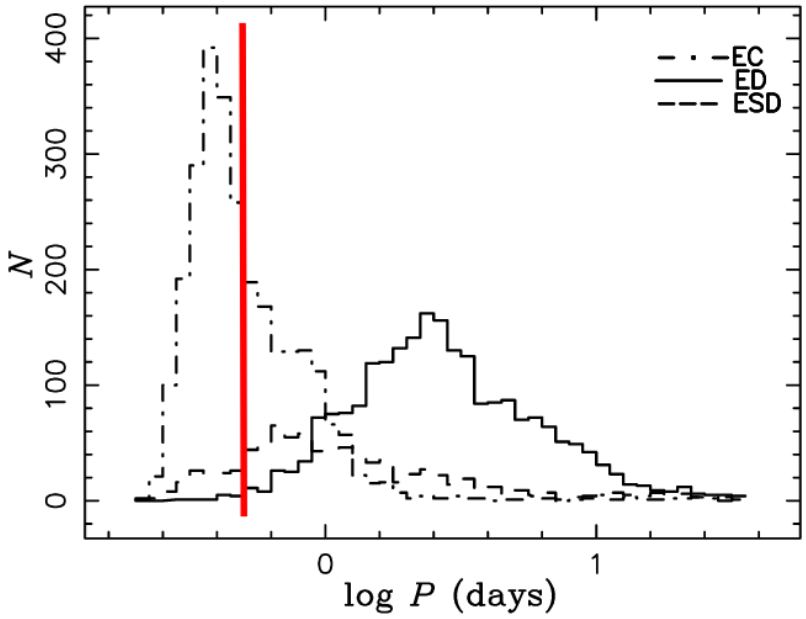

FIGURE 6.4: The period distribution of eclipsing binaries discovered by the All Sky Automated Survey (Li *et al.*, 2007). EC, ED and ESD stands for eclipsing contact, detached and semi-detached binaries respectively. The red line marks the period range of all four binaries in the $\mathrm{Q}0.7$ simulations.

6.2.1 Diagnostics

In order to study the evolution of the binaries in the Q0.7 simulations, we analyzed the temporal evolution of the following global parameters, called "diagnostic quantities":

1. Maximum density of the donor and accretor, $\rho_{\rm max,D}$ and $\rho_{\rm max,A}$
2. Binary separation, a
3. Mass ratio, $\rm q = M_D/M_A$ and normalized mass ratio, $\rm q/q_0$
4. Mass transfer rate normalized to the initial mass and period, $\frac{|\dot{\rm M}|}{\rm M_0} = \frac{\rm dM/dt}{\rm M_0/P_0}$, for both donor and accretor
5. Normalized orbital angular momentum, $\rm J_{orb}/J_{orb,0}$
6. Normalized spin angular momentum of the donor and accretor, $\rm J_D/J_{D,0}$, $\rm J_A/J_{A,0}$

Here a subscript "0" denotes the initial value, "D" denotes the donor and "A" denotes the accretor. The donor and accretor material were separated by a plane normal to the line joining the maximum density of the two stars near the $\rm L_1$ point. We terminated the diagnostic plots at a point in time when the tools could no longer distinguish between the two stars. In addition to the above diagnostic quantities, we studied the evolution of the density distribution in the equatorial plane. A data file containing the density field, called a "frame", was written 120 times per initial orbit in Flow-ER and 100 times per initial orbit in Octotiger.

The time in our discussions was always normalized with respect to the initial orbital period, $\rm P_0$, for the respective model. Similar to Motl *et al.* (2017a), we decided to synchronize the simulations with respect to a single event during the evolution, the merger of the binary occuring at time $t_{\rm merge}$. In Motl *et al.* (2017a), the $t_{\rm merge}$ was determined by examining the evolution of the density by eye, such that only one density distribution could be identified. However, in the bipolytropic Q0.7 simulations, the core of the donor gets wrapped around the accretor during the merger and there was no clear point in time when we could be certain that the binary has "fully merged" with a single density distribution. Hence for the Q0.7 simulations, we defined $t_{\rm merge}$ for the octHR simulation such that the the accretor spin angular momentum achieves the maximum value during the merger phase (Figure 6.18). We then compare the frame corresponding to $t_{\rm merge}$ for the octHR to the other simulations, by eye. The time corresponding to this closest matching frame is identified as $t_{\rm merge}$ for that particular simulation. Once $t_{\rm merge}$ has been identified for each simulation, we could synchronize all the time-dependent plots for the Q0.7 simulations. The particular choice of the accretor spin angular momentum is discussed later in section 6.2.3. The choice of the temporal "zero point" is somewhat arbitrary and we chose the beginning of cylHR simulation as this point. Hence we shifted the diagnostic plots for the rest of the simulations such that the $t_{\rm merge}$ for each of them coincides. This shifted time was given by

$$t_{\rm shift} = t + t_{\rm zpt} \tag{6.1}$$

where

$$t_{\rm zpt} = t_{\rm merge,\ cylHR} - t_{\rm merge}. \tag{6.2}$$

The time of merger depends on the mass transfer rate, which in turn depends on the depth of initial contact as well as the resolution. We also cannot exactly match the depth of contact that

the Roche lobe makes with the stellar surface at the end of the driving phase. With the increase in resolution, the simulations can resolve lower mass transfer rates thus resulting in longer $t_{\rm merge}$. This results in different $t_{\rm merge}$ for each simulation, in general (see Table 6.4), which is expected. This difference in $t_{\rm merge}$ did not affect the dynamics of the Q0.7 simulations during the merger phase. However, in certain cases it is possible that at relatively low mass transfer rates, two different numerical techniques can produce quantitatively different results. Motl *et al.* (2017a), for example, show that for $q < q_{\rm crit}$, the outcome differs between grid based and SPH codes, and it depends on the initial depth of contact.

6.2.2 Expectations

Before analyzing the results, let us consider the outcome that we may expect from the simulations. The mass ratio of the initial model in each of the Q0.7 simulations was about 0.7. As discussed in section 3.3, there are two critical mass ratios which may determine the ultimate outcome of a mass transfer event. The first critical mass ratio is $q_a = 1$ for the separation; below this value the separation increases on mass transfer and above this value it decreases (Equation 3.30). The next critical mass ratio is $q_{\rm crit}$, arising from the adiabatic response of the donor to mass loss. This also incorporates the response of the Roche lobe to the mass transfer (Equation 3.36). For a continuous polytrope with $n = 3/2$, $q_{\rm crit} = 2/3$. The donor in the Q0.7 bipolytropic binaries consists of about 90% envelope by mass, which has polytropic index, $n_{\rm e} = 3/2$. Hence we assume $q_{\rm crit} \approx 2/3$ for this discussion. Depending on where the initial mass ratio, q_0, lies at the beginning of mass transfer, we can have the following three possibilities.

1. $q_0 < q_{\rm crit} < q_a$
   In this case, the separation increases, the Roche lobe of the donor expands and the donor shrinks on mass transfer. Thus, this is the most stable case and further mass transfer proceeds on the secular timescale of the angular momentum loss. Motl *et al.* (2017a) found that the ultimate outcome may depend on the initial depth of contact achieved at the end of driving.

2. $q_{\rm crit} < q_0 < q_a$
   In this case, the separation increases, however, the depth of contact also increases on mass transfer. The Q0.7 models lie in this region. The outcome depends on the adiabatic response of the donor for the particular bipolytropic configuration. For a continuous $n = 3/2$ polytrope, the binary ends up merging with a tidal instability, as the donor material gets tidally wrapped around the accretor. Note that for the case of $n = 3/2$, the donor expands on mass loss according to Equation 3.35.

3. $q_{\rm crit} < q_a < q_0$
   In this case, the separation decreases and the depth of contact increases on mass transfer. These conspire to increase the mass transfer rate monotonically, ultimately leading to a merger. The donor gets tidally disrupted with a more head-on impact between the two stellar cores.

Note that the critical values for the binary systems in our simulations, and in real stars, may be different from the above, especially $q_{\rm crit}$. This is because Q0.7 models are not continuous polytropes, in addition to the non-linear effects such as development of a disk-like structure

around the accretor which can feed angular momentum back in to the orbit. The actual value may lie in the range $0.22 < q_0 < 2/3$. Furthermore, non-conservative mass transfer with a net angular momentum loss makes the binary more unstable and prone to merger.

6.2.3 Evolution

In this section we describe the evolution of the Q0.7 binaries and discuss the similarities and differences between the four simulations. We find that the end states as well as the intermediate behavior agree very well with the theoretical expectations and also between the simulations. There are a few key differences between the simulations, all of which can be accounted for by our current understanding of the numerical codes.

Table 6.4 describes the summary of the Q0.7 simulations along with some quantities of interest. The equation of state for the two simulations is described in detail earlier in section 5. All Q0.7 simulations were driven for 4 initial orbits at the rate of 2% per orbit. In other words, 2% of the angular momentum was systematically removed from the system per orbit for a time which is equal to 4 times the initial orbital period. One can notice in Table 6.4, that the time taken from the beginning of the simulation to the merger, $t_{\rm merge}$, varied by a large factor across the simulations. The table also lists the cost of performing each simulation in terms of computational time. For the Flow-ER code, the cylHR simulation was about 21 times more expensive per orbit, as compared to the cylLR simulation. However, when we take into account the difference in the volumes (the cylHR domain is only about 58% of that of the cylLR simulation by volume), the cylHR simulation turns out to be about 36 times more expensive as compared to the cylLR. In the case of the Octotiger simulations, the octHR domain contains about 7.4 times more volume as compared to its low resolution counterpart. Thus when compensated for volume, the octHR simulation is about 10% cheaper to run per orbit, as compared to the octLR simulation. This is because with the AMR, the computational cost increases with the increased number of cells and not just the volume. Although the central region is more resolved, the low resolution, outer volume is much less expensive to compute in the octHR simulations. This comparison highlights the power of AMR for the numerical studies of binary systems.

As listed in Table 6.4, the time to merger was longer for the Flow-ER simulations as compared to the Octotiger ones and it was also longer at a higher resolution. We can explain the observed trend as follows. First consider the trend across the two codes. As described in Chapter 5, the two codes have a key difference – Octotiger uses the dual energy formalism for internal energy which allows for shock heating of the material. When the accretion stream impacts the accreting star, the supersonic velocities shock-heat the outer atmosphere of the stars, forming a puffed up CE-like structure. This condition is exacerbated by the fact that radiative transport is not implemented in the code, which prevents the material from cooling. With a hot atmosphere, the mass transfer rate should be higher in Octotiger simulations, as it should scale with the sound speed of the fluid near the $\rm L_1$ point. This CE can also possibly cause numerical drag on the binary, leading to a relatively rapid merger even at the same level of initial contact depth. The lack of shock-heating keeps the velocity near the $\rm L_1$ point at a consistent low value in the Flow-ER simulations, resulting in a slower mass transfer rate, taking longer time to merge. This numerical artifact can be minimized when the radiative transport equations are solved, taking into account the radiative cooling of the hot atmosphere. The puffed up atmosphere in Octotiger is demonstrated in Figure 6.5. The two

TABLE 6.4: Quantities of interest for Q0.7 simulations

Model ID	cylLR	cylHR	octLR	octHR
EoS[1]	Ideal gas	Ideal gas	Dual Energy Formalism	Dual Energy Formalism
$t_{\mathrm{drive}}(t/P_0)$[2]	4	4	4	4
$\dot{J}^3_{\mathrm{drive}}$ ($\%$ per t/P_0)	2	2	2	2
$t_{\mathrm{merge}}(t/P_0)$[4]	15.02	24.58	12.10	12.91
$t_{\mathrm{zpt}}(t/P_0)$[5]	9.83	0	12.75	11.94
Timesteps	~ 1.84 M	~ 7.02 M	~ 160 k	~ 525 k
$\mathrm{T}_{\mathrm{wall}}(\mathrm{d})$[6]	6	177	16	38
Number of processors	256	256	1280	4000
Cost (CPU-hr/orbit)	~ 2.07 k	~ 43.67 k	~ 39.67 k	~ 268 k
Cost (calc./orbit)	$\sim 1.74 \times 10^{13}$	$\sim 3.66 \times 10^{14}$	$\sim 4.00 \times 10^{14}$	$\sim 2.70 \times 10^{15}$
Machine	QueenBee (LONI)	QueenBee (LONI)	SuperMIC (LSU HPC)	SuperMIC (LSU HPC)
Processors	2.33GHz 4-Core Xeon 64-bit	2.33GHz 4-Core Xeon 64-bit	2.8GHz 10-Core Ivy Bridge-EP Xeon 64-bit	2.8GHz 10-Core Ivy Bridge-EP Xeon 64-bit

[1] Equation of state used in the simulation for determining the pressure [2] Time the system was initially driven by removal of angular momentum [3] The rate of driving [4] The time of merger (as determined in section 6.2.1) [5] The difference between $\mathrm{t}_{\mathrm{merge}}$ for cylHR simulation and the current one (Equation 6.2) [6] The time needed to complete the simulation

higher resolution simulations lasted longer because they resolve a lower mass transfer rate, in general. However, the cylHR simulation lasted significantly longer than its low resolution counterpart.

At this point we would like to mention an additional artifact of the finite difference methods that can be seen in the Flow-ER simulations. As shown in Figure 6.6, the low density material being ejected from the L_2 and L_3 points in Flow-ER simulations, even before the mass transfer begins, is called "numerical wind". Since this outflow is almost absent at a higher resolution, it is a clear sign of numerical error in the outer regions of a star due to its relatively poor resolution away from the center. Note that a real outflow of material may occur in mass transferring binaries from these outer Lagrangian points.

The time-dependent behavior of key diagnostic parameters are plotted in Figures 6.7 – 6.14. We conclude that all four binary models were unstable to mass transfer, resulting ultimately in a merger. Figures 6.7 and 6.8 show plots of the central density of the donor and accretor respectively as the Q0.7 binaries evolve. Consider the evolution of the central density of the Flow-ER

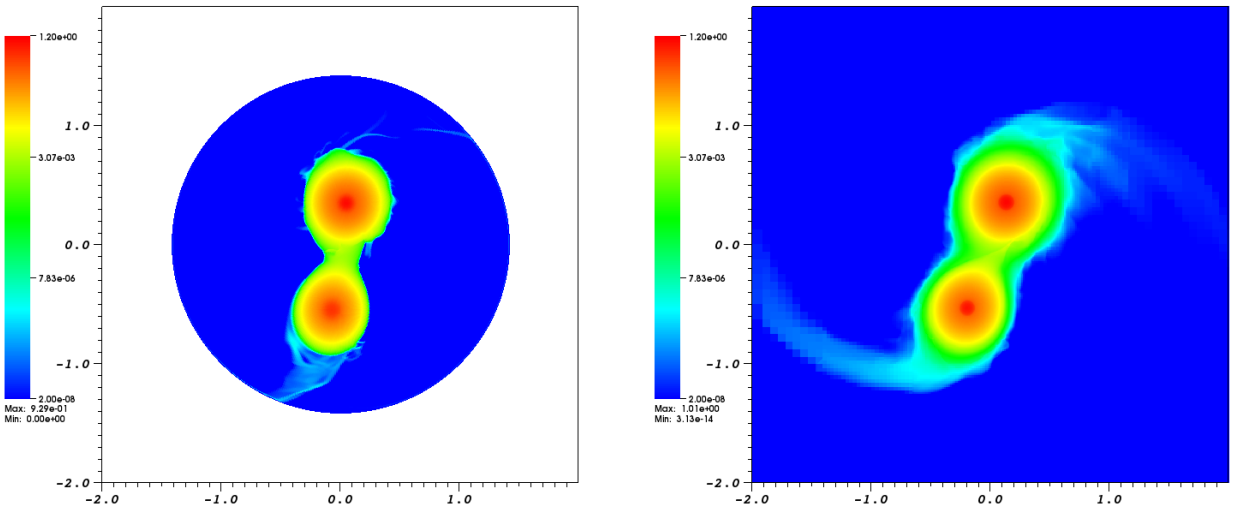

(a) CylHR

(b) OctHR

FIGURE 6.5: This equatorial cross section of the density field shows the puffed up outer atmosphere in the Octotiger simulation, caused by the shock heating and the lack of radiative cooling (right). This numerical artifact is absent in the Flow-ER simulation (left).

simulations first. As we expect from the analysis in section 5.3, the Flow-ER simulations showed a decrease in the central density of both the stars with time. It is possible to predict the initial fall in the central density of the Flow-ER simulations by calculating the peak parameter values of the initial models and using its trend in Figure 5.4. We expected this fall to be also a function of resolution, because increased resolution can better resolve the steep density gradients near the core. We confirmed this prediction by comparing the plots for cylLR and cylHR simulations. For both the donor and the accretor, as the resolution increased, the central density showed less deviation from the initial value of unity. Note that the mass transfer began just before the driving phase is stopped at the fourth orbit, after the start of a simulation. In Figures 6.7 and 6.8 we can observe that as soon as the mass transfer started, the behavior of the central density changed for both the donor and the accretor in the Flow-ER simulations, and the slope of the fall increased. A similar change in the central density of the donor or the accretor did not occur in the case of Octotiger simulations. For all four simulations, as the mass transfer continued, the central density of the donor decreased, while that of the accretor started to increase. This is because the central density is, in general, proportional to the stellar mass. Although the fall in the central density in the Flow-ER simulations was dramatic for both the components, we will see that this did not significantly affect the dynamical evolution of these binary systems.

Next consider the separation between the two components, plotted in Figure 6.9. Oscillations with an amplitude of $\sim 2\%$ can be noticed throughout the evolution up to merger for all four simulations. In general, an initial binary model obtained through the BSCF method is not in perfect equilibrium and the orbits are not perfect circles. The Q0.7 binaries were further perturbed by the artificial removal of the angular momentum during the initial driving phase, exacerbating

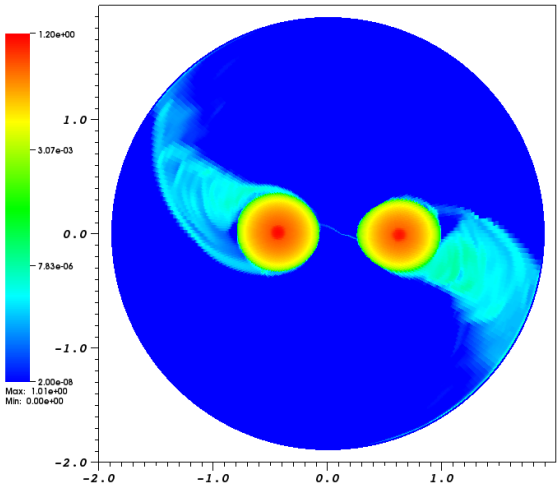

(a) cylLR

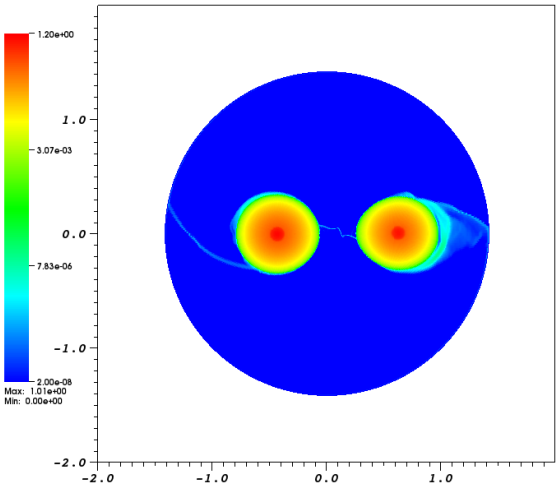

(b) cylHR

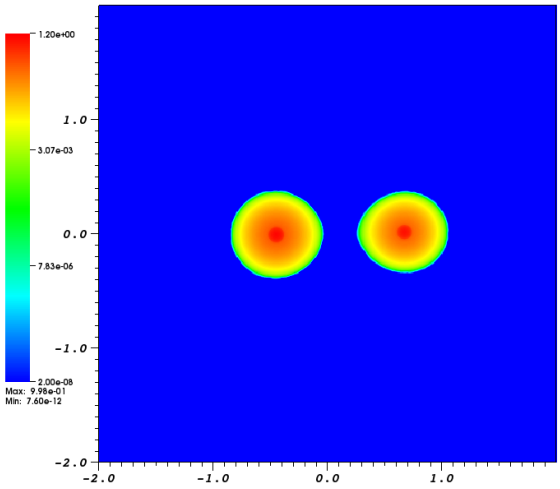

(c) octLR

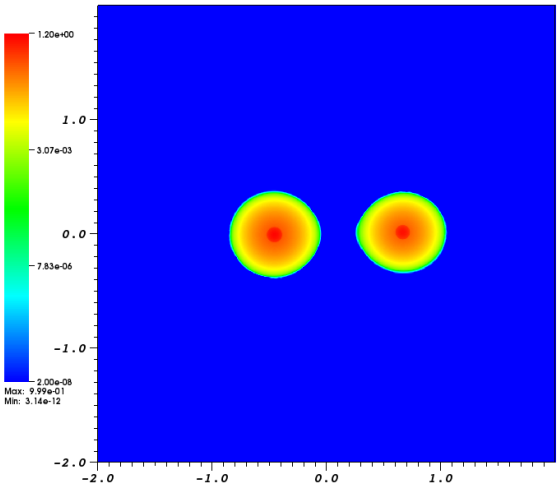

(d) octHR

FIGURE 6.6: The "numerical wind" caused by the numerical diffusion due to the poor resolution in Flow-ER can be easily noticed in the equatorial cross section of the density field. This numerical artifact depends on the resolution. Octotiger density fields are also shown at the bottom for comparison, where this effect is not present.

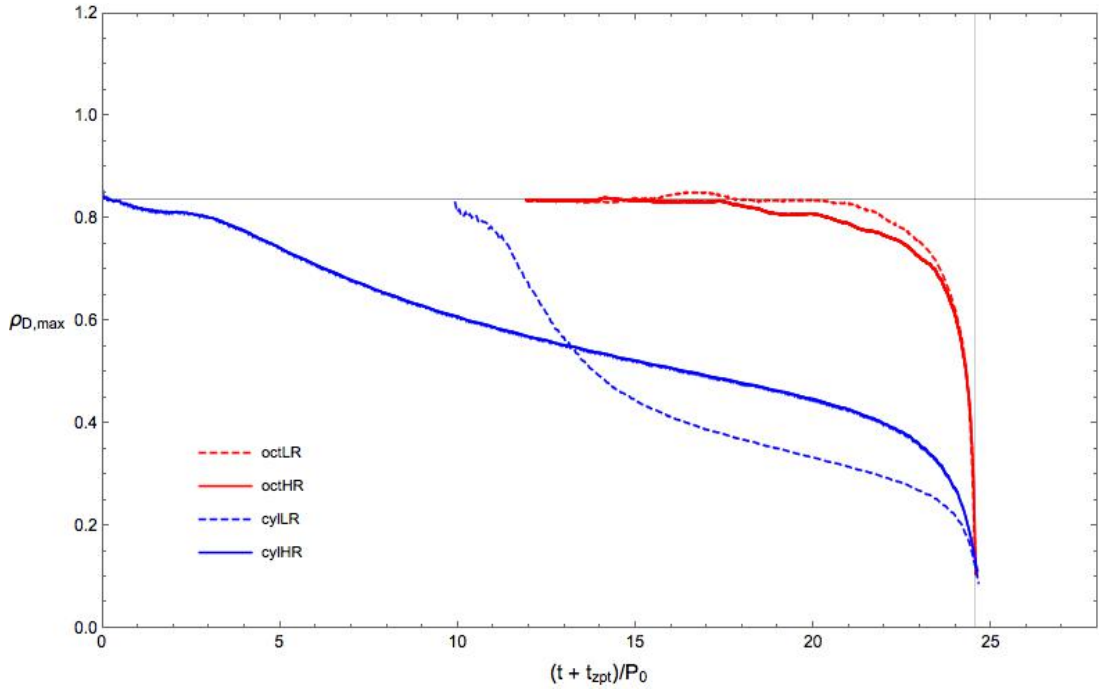

FIGURE 6.7: Time-dependent behavior of the donor maximum density for Q0.7 simulations. The vertical line marks $t_{\rm merge}$. The horizontal line marks the approximate value of the initial donor maximum density.

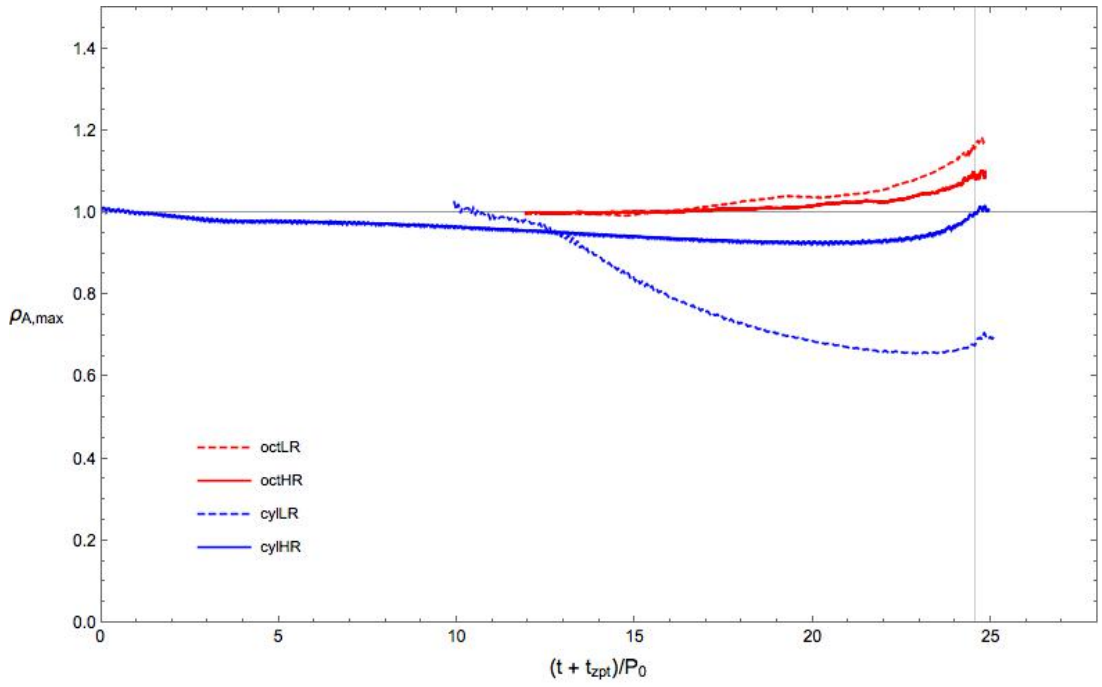

FIGURE 6.8: Time-dependent behavior of the accretor maximum density for Q0.7 simulations. The vertical line marks $t_{\rm merge}$. The horizontal line marks the approximate value of the initial accretor maximum density.

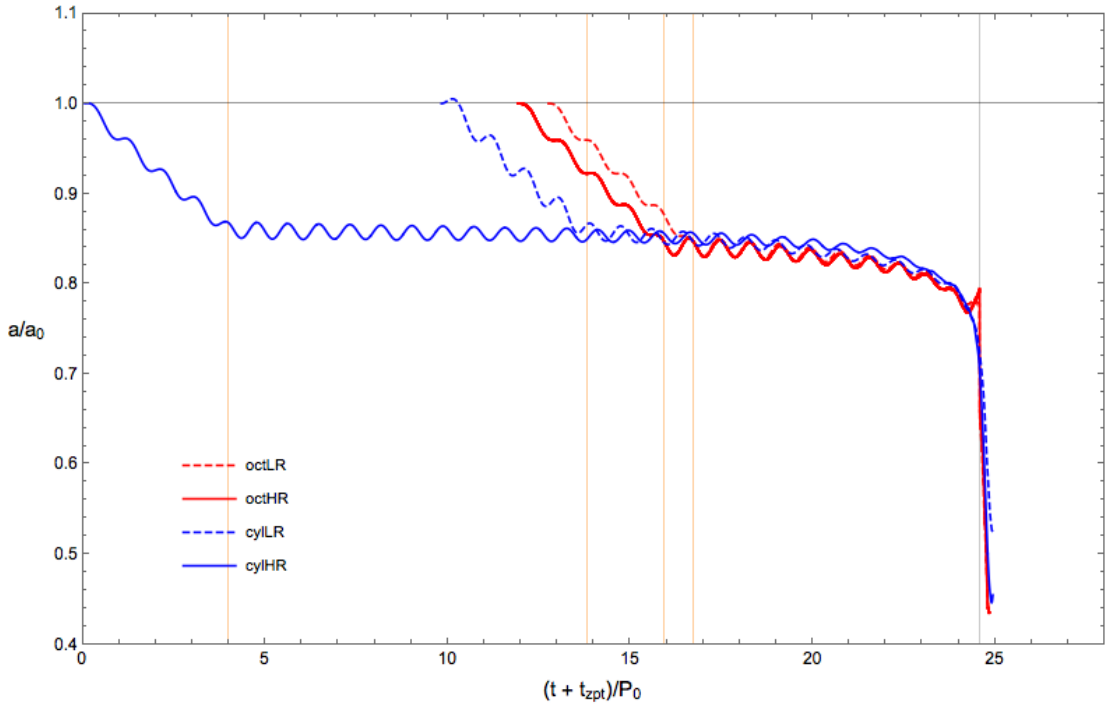

FIGURE 6.9: Time-dependent behavior of the normalized separation for Q0.7 simulations. The orange vertical lines mark the end of initial driving phase for cylHR, cylLR, octHR and octLR simulations respectively. The vertical grey line marks $t_{\rm merge}$.

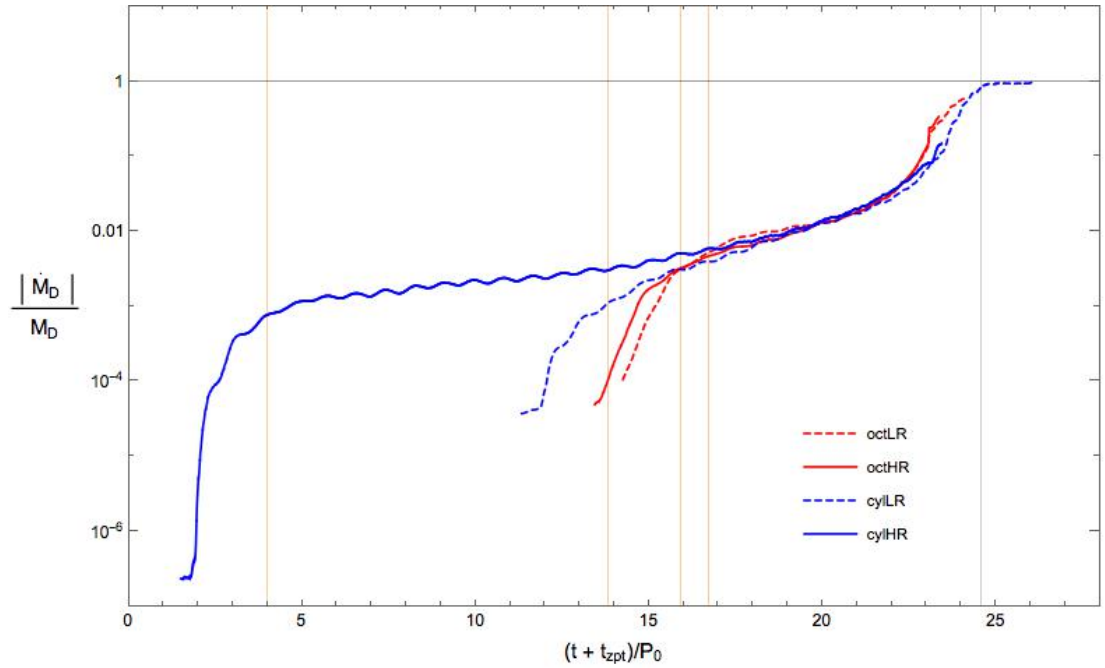

FIGURE 6.10: Time-dependent behavior of the smoothed mass loss rate of the donor for Q0.7 simulations. The orange vertical lines mark the end of initial driving phase for cylHR, cylLR, octHR and octLR simulations respectively. The vertical grey line marks $t_{\rm merge}$.

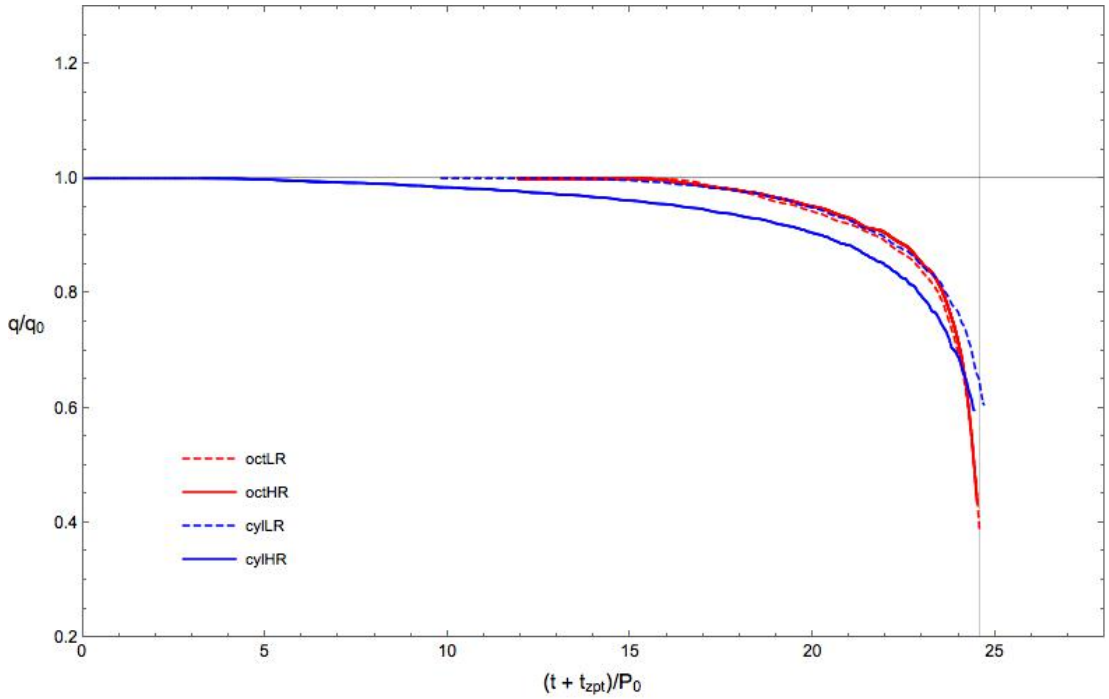

FIGURE 6.11: Time-dependent behavior of the normalized mass ratio for Q0.7 simulations. The vertical grey line marks $t_{\rm merge}$.

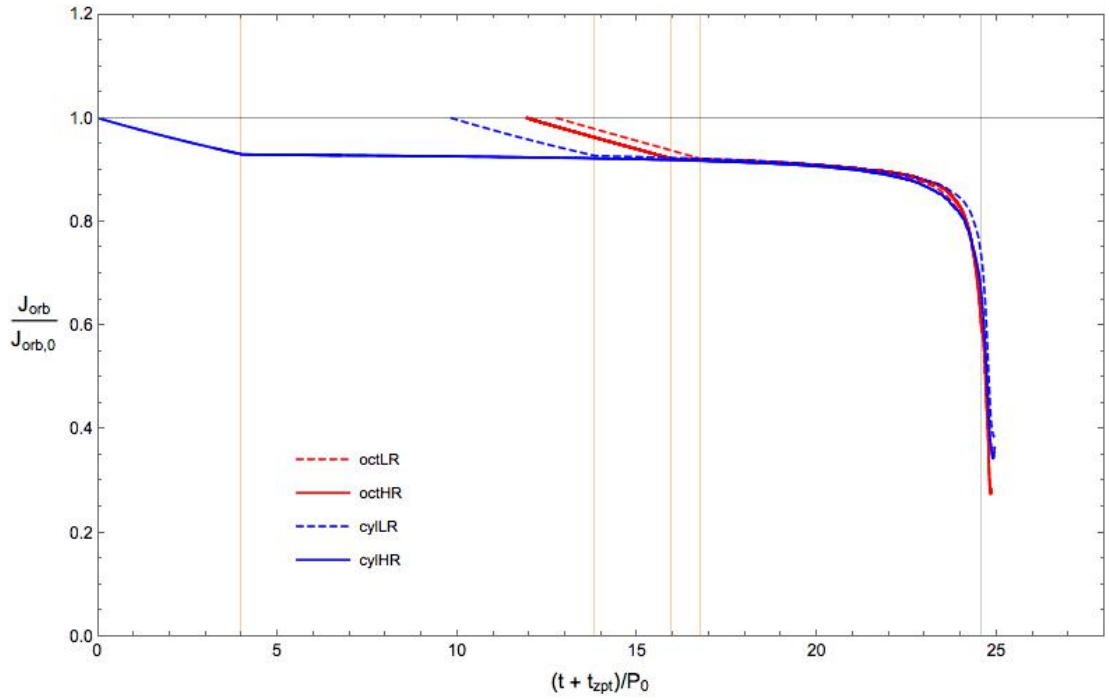

FIGURE 6.12: Time-dependent behavior of the orbital angular momentum for Q0.7 simulations. The orange vertical lines mark the end of initial driving phase for cylHR, cylLR, octHR and octLR simulations respectively. The vertical grey line marks $t_{\rm merge}$.

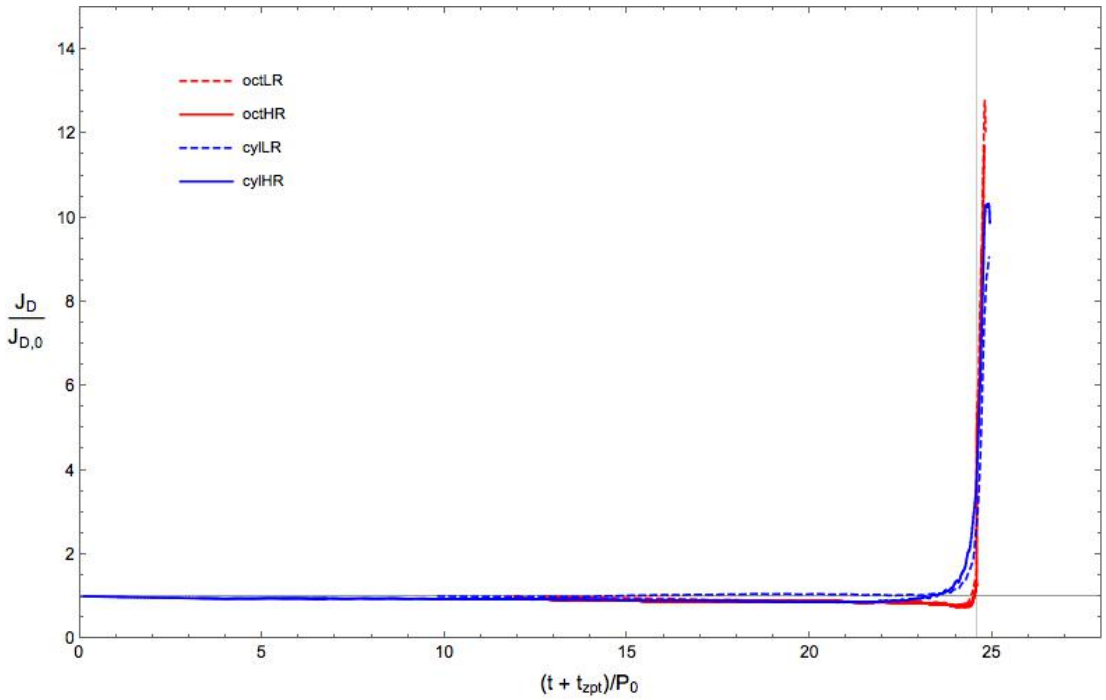

FIGURE 6.13: Time-dependent behavior of the normalized donor angular momentum for Q0.7 simulations. The vertical grey line marks $t_{\rm merge}$.

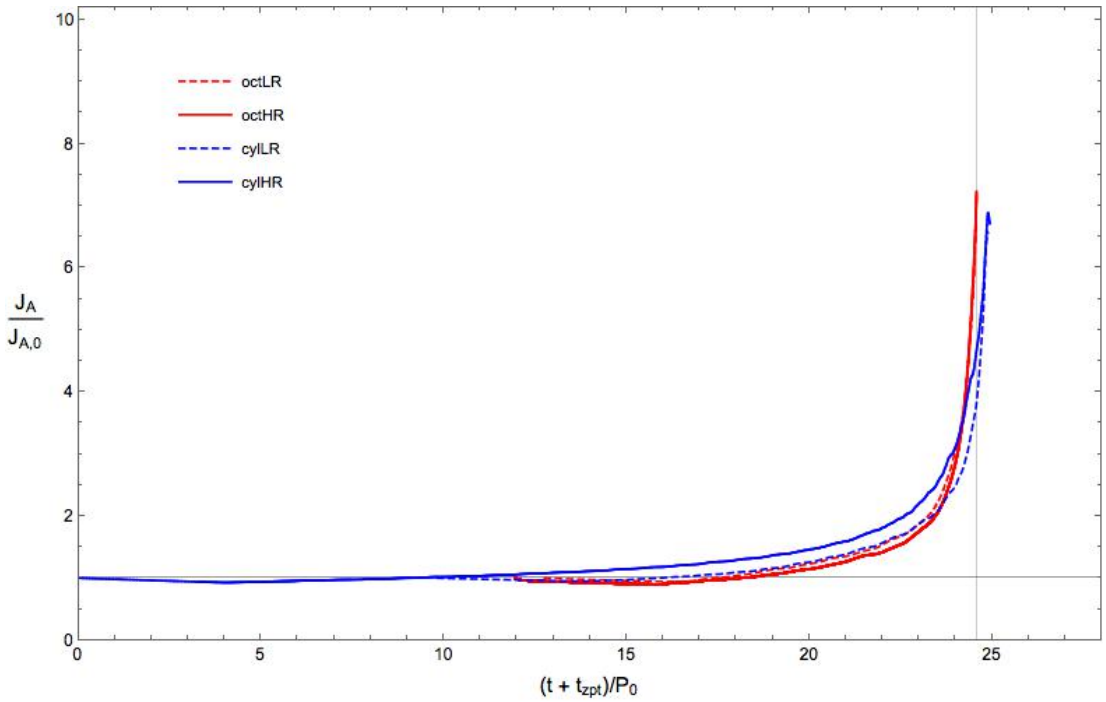

FIGURE 6.14: Time-dependent behavior of the normalized accretor angular momentum for Q0.7 simulations. The vertical grey line marks $t_{\rm merge}$.

the situation. The final amplitude of the oscillations also depends on their exact phase when the driving is stopped. The slight deviations from equilibrium resulted in the epicyclic oscillations of the binary components about the mean separation. The period of epicyclic oscillations thus closely matched the binary's orbital period at that time, but not the initial orbital period. The absolute phase of these oscillations should not be expected to match for any two simulations. The next prominent feature is an initial, roughly linear fall in the separation for the first 4 orbits, which was a direct result of the artificial removal of angular momentum, as each binary was driven together. As stated in Equation 3.27, the logarithmic derivative of the separation, $\dot{a}/a$, is proportional to twice that of the angular momentum, $\dot{J}/J$. A total of 8% decrease in the total angular momentum thus resulted in about 16% decrease in the separation, as observed in Figure 6.9. We made sure that a measurable mass transfer was established before the driving was stopped. The behavior of the Q0.7 systems agreed remarkably well after this point, $\mathrm{i.e.}$ after $(t + t_{\rm zpt})/P_0 \approx 16.5$. The separation decreased gradually over about six orbits, until the binary merges with a precipitous fall in the separation. The merger was rapid and occurred within only about two orbits.

Figure 6.10 shows the smoothed mass transfer rate of the donor, $|\dot{M}|/M_{\rm D,0}$, which is normalized with respect to its initial mass. The four curves in this plot essentially represent the history of mass transfer in the Q0.7 simulations. Note that the ordinate is in logarithmic scale. We needed to use the smoothed rates, since the plots for the instantaneous mass transfer rate turned out to be very noisy because of the subtraction of two nearly equal quantities both in the numerator as well as denominator. The smoothing was performed using a moving boxcar average with a width of three initial orbital periods. The relatively low amplitude oscillations in the $|\dot{M}|/M_{\rm D,0}$ before the final peak are caused by the change in the mass transfer rate due to the epicyclic oscillations in the orbital separation. Once the driving ended and a steady mass transfer began at $(t + t_{\rm zpt})/P_0 \approx 16.5$, $|\dot{M}|/M_{\rm D,0}$ increased steadily as the binaries evolved. The average rate of the normalized mass transfer after $(t + t_{\rm zpt})/P_0 \approx 16.5$ was of the order of 0.1 per orbit, which explains the lifetime of the binary with the merger occurring within about 8 orbits. The length of a simulation is determined by the initial depth of contact achieved at the end of the driving phase, which in turn determines the mass transfer rate. The cylHR simulation lasted the longest because at the end of its driving, $|\dot{M}|/M_{\rm D,0} \approx 10^{-5}$, while octLR simulation lasted the shortest time as the mass transfer rate at the end of its driving phase was the highest amongst the Q0.7 simulations, $\mathrm{M}_{\rm D,0} \approx 5 \times 10^{-3}$. The difference in the mass transfer rates between the Flow-ER and Octotiger simulations, as explained earlier, could also be attributed to the difference in the EoS. We did not precisely control the initial depth of contact, however, neither the ultimate outcome nor the intermediate behavior of the binary is sensitive to its precise value, in general. The shifted plots for $|\dot{M}|/M_{\rm D,0}$ matched very well for all simulations after the end of the initial driving phase at $(t + t_{\rm zpt})/P_0 \approx 16.5$, until about two orbits before the merger. All simulations showed a sharp increase in $|\dot{M}|/M_{\rm D,0}$ near the end, which indicates a rapid merger. However, during the final phase of the merger, there is a quantifiable difference between the Flow-ER and the Octotiger simulations. We conjecture that the higher mass transfer rate during the merger process in the Octotiger simulations was caused by the hotter atmosphere of the donor. This effect is absent in the Flow-ER simulations since the code does not take into account shock-heating. We will present more evidence later in this section, to support this hypothesis.

Figure 6.11 shows the normalized mass ratio of the Q0.7 simulations. As the binaries evolved, q decreased monotonically, and it continued to decrease even after driving was stopped, indicating a continuing mass transfer from the lower mass component to its companion. The q/q_0 plots for all Q0.7 simulations, except for the cylHR, show a high degree of agreement. The discrepancy between the evolution of the mass ratio of the cylHR simulation and the other simulations combined can be explained as follows. As a simulation progresses, the mass ratio depends on the initial masses of both the components in a binary, as well as the amount of mass is transferred from the donor to the accretor. Consider Figure 6.10 again, which shows that the mass transfer in the case of the cylHR simulation lasted almost twice as long as the other three simulations. Before we expect an agreement between the codes, i.e. before $(t + t_{\rm zpt})/P_0 \approx 16.5$, the donor in the cylHR simulation was already transferring mass for about 12.5 orbits. Over this period, the normalized mass transfer rate can be considered as approximately 2×10^{-3} per orbit. Thus the donor had transferred about 2.5 % of its mass before $(t + t_{\rm zpt})/P_0 \approx 16.5$, making the mass ratio smaller by the same factor, as observed in Figure 6.11. Notice that over the last two orbits, the Octotiger simulations show a steeper slope as compared to the Flow-ER simulations, indicating a larger rate of mass transfer, as we have already seen in Figure 6.10.

The normalized orbital angular momenta, $J_{\rm orb}/J_{\rm orb,0}$ are plotted in Figure 6.12, for the Q0.7 simulations. Since all binaries were driven for four orbits at the rate of 2% per orbit, the orbital angular momentum for each simulation initially showed a linear decline of a total of 8%. Figures 6.13 and 6.14 show the plots for the normalized spin angular momenta of the donor and accretor respectively. First consider the qualitative behavior of these plots during the mass transfer. For all Q0.7 simulations, $J_{\rm orb}/J_{\rm orb,0}$ decreased steadily even after the driving is stopped and just before the merger, it fell precipitously over the last two orbits. We see that as $J_{\rm orb}$ decreased right before the merger, both $J_{\rm D}$ and $J_{\rm A}$ peaked sharply, indicating that the orbital angular momentum was being used to spin up each of the binary components. This behavior of the angular momenta was a clear indication of tidal instability of the binary system. With this instability, each component tried to maintain synchronicity, which extracted angular momentum from the orbit, resulting in a merger. In certain cases the binary can develop a mass-transfer instability, wherein the donor keeps transferring mass to the accretor in a dynamically unstable manner, such that the separation decreases and the donor essentially ends up "falling" on the accretor. Thus the spin angular momentum of the donor remains relatively constant until the merger, unlike the Q0.7 simulations. We determined $t_{\rm merge}$ on the basis of $J_{\rm A}$ because in all cases, the accretor angular momentum grows rapidly during the final stages of binary merger.

All three angular momenta (orbital and spin for both the components) generally agree across the Q0.7 simulations, however, there are two differences. The accretor angular momentum of the cylHR simulation starts to deviate early on from the corresponding curves of the other simulations, and the two codes behave differently during the merger over the last two orbits before $t_{\rm merge}$. Consider the evolution of $J_{\rm D}$ in the cylHR simulation. As seen earlier, the donor had transferred about 2.5 % of its mass before $(t + t_{\rm zpt})/P_0 \approx 16.5$. This mass also carried angular momentum, which resulted in spinning up of the accretor. The component of the velocity of the accreting material at the $\rm L_1$ point, perpendicular to the line joining the two stars can be given as $v_\perp = R_{LA} \times \Omega$, where R_{LA} is the Roche lobe radius of the accretor. Using the values in Table 6.2, we can estimate that the $\approx 2.5\%$ mass lost by the donor transferred about 4.6%

of its angular momentum to the accretor before $(t + t_{\rm zpt})/P_0 \approx 16.5$. The accretor also had sufficient time to interact with, and gain angular momentum from, $J_{\rm orb}$. The combination of these two factors can explain the observed discrepancy of $J_{\rm A}$ in Figure 6.14. During the final two orbits before the merger, the behavior of the spin angular momentum of the donor as well as the accretor is different between the two codes. The sharper rise in the slope of both $J_{\rm D}$ and $J_{\rm A}$ in the case of the Octotiger simulations suggests that the orbital angular momentum was extracted more efficiently during the merger. This could be facilitated by a higher mass transfer rate near the end. Thus the difference in the spin angular momenta between the Flow-ER and Octotiger simulations is consistent with our previous analysis of the mass transfer rate.

Figures 6.15 – 6.19 show equatorial cross sections of the density fields during the evolution of the Q0.7 simulations. We used an open source visualization tool VisIt (Childs *et al.*, 2012) to render the cross sectional frames for the simulations. The distance scale used is the same for each simulation and each frame is 4 code length-units wide. The density field ranged from 2×10^{-8} to 1.2 in code units and is plotted on a logarithmic scale, with the intention of visualizing the low density accretion stream, while also depicting the core-envelope structure. Each figure corresponds to the same $(t + t_{\rm zpt})/P_0$ during the binary simulation, thus representing the same stage of the dynamical evolution. Figure 6.15 corresponds to $(t+t_{\rm zpt})/P_0 = 16.58$ when a steady, direct impact mass transfer stream was established. The time is close to the end of driving phase of the octLR simulation (see Figure 6.12). The behavior of the Q0.7 systems agreed remarkably well after this point, with the exceptions discussed above. The resolution-dependent numerical wind can be noticed in the Flow-ER simulations. This figure also shows the formation of a common envelope which is more prominent in the Octotiger simulations, due to the shock-heated atmosphere. Figure 6.16 corresponds to four orbits before the merger, at $(t + t_{\rm zpt})/P_0 = 20.58$. The material escaping from the $\rm L_2$ and $\rm L_3$ points at this time in a pinwheel formation can be considered a numerical artifact in both Flow-ER and Octotiger simulations. As discussed before, in the Flow-ER simulations the escaping material was the numerical wind and in the Octotiger simulations, the shock-heating of the outer atmosphere caused it to puff up and escape through the Lagrangian points. The outflow was clearly resolution dependent for a given code.

Figures 6.17 and 6.18 show inspiral of the Q0.7 binary systems before the merger. Consider the former frame where all four simulations showed the material lost through the $\rm L_2$ and $\rm L_3$ points, forming a double pinwheel pattern. At this point the mass loss can be considered "real", since mass lost through the outer Lagrangian points carries angular momentum and can result in a rapid merger, which did occur in the Q0.7 simulations. The contrast between the core and the envelope in the Flow-ER simulations was noticeably less sharp as compared to the Octotiger ones, especially in case of the donor star. This is because in the Flow-ER simulations, the contact discontinuity at the core-envelope boundary dissolved with time due to the poor resolution of the core. The density distribution in Figure 6.18 was used to determine $t_{\rm merge}$ for all simulations by matching as closely as possible with the octHR density. The $t_{\rm merge}$ for the octHR simulation was fixed, as explained earlier, as the point of time when the accretor angular momentum achieved the maximum value.

Figure 6.19 shows the density in the equatorial plane right after the merger when disruption of the donor is complete according to the diagnostic plots. However, the remnants of the former

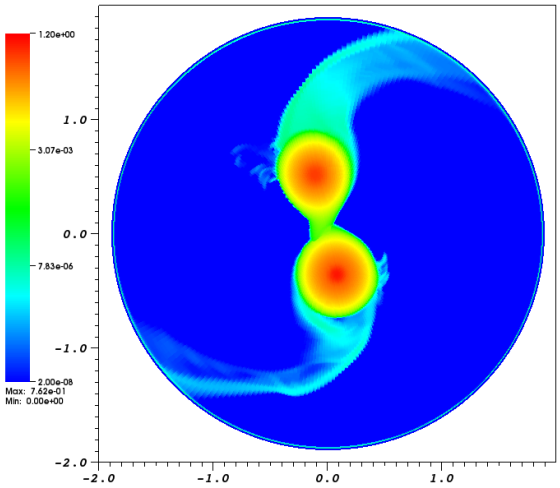

(a) cylLR

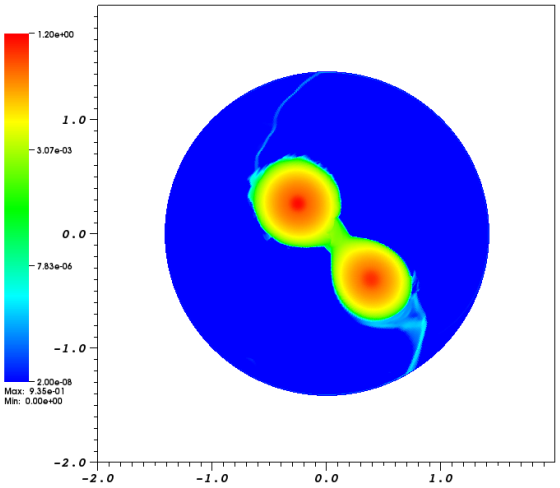

(b) cylHR

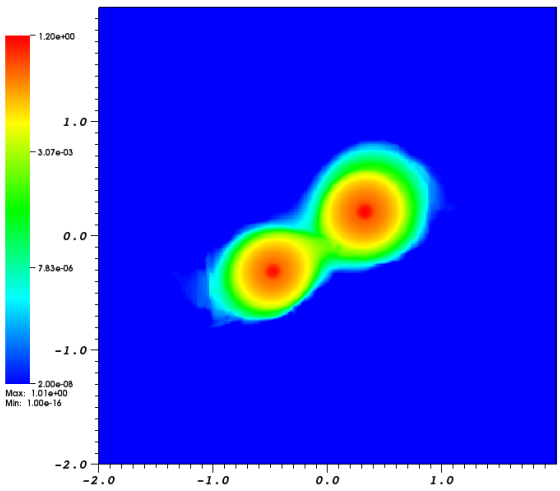

(c) octLR

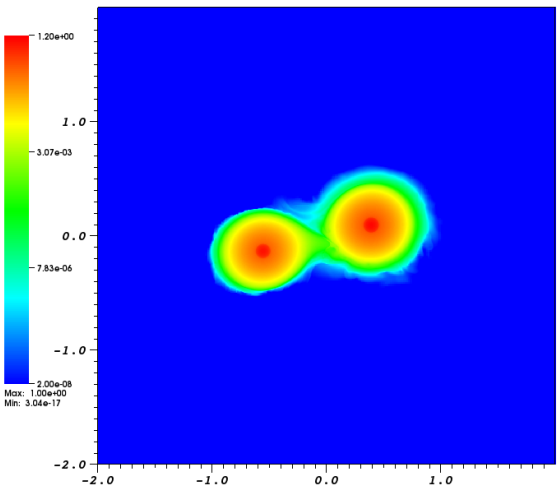

(d) octHR

FIGURE 6.15: Equatorial cross section of the density field at $\mathrm{t}_{\mathrm{merge}} - 8.0$ or $(t + t_{\mathrm{zpt}})/P_0 = 16.58$. The diagnostic quantities of the simulations agree after this point. This view also shows resolution dependent numerical wind in Flow-ER simulations and shock-heated atmosphere of the binary systems in the Octotiger simulations.

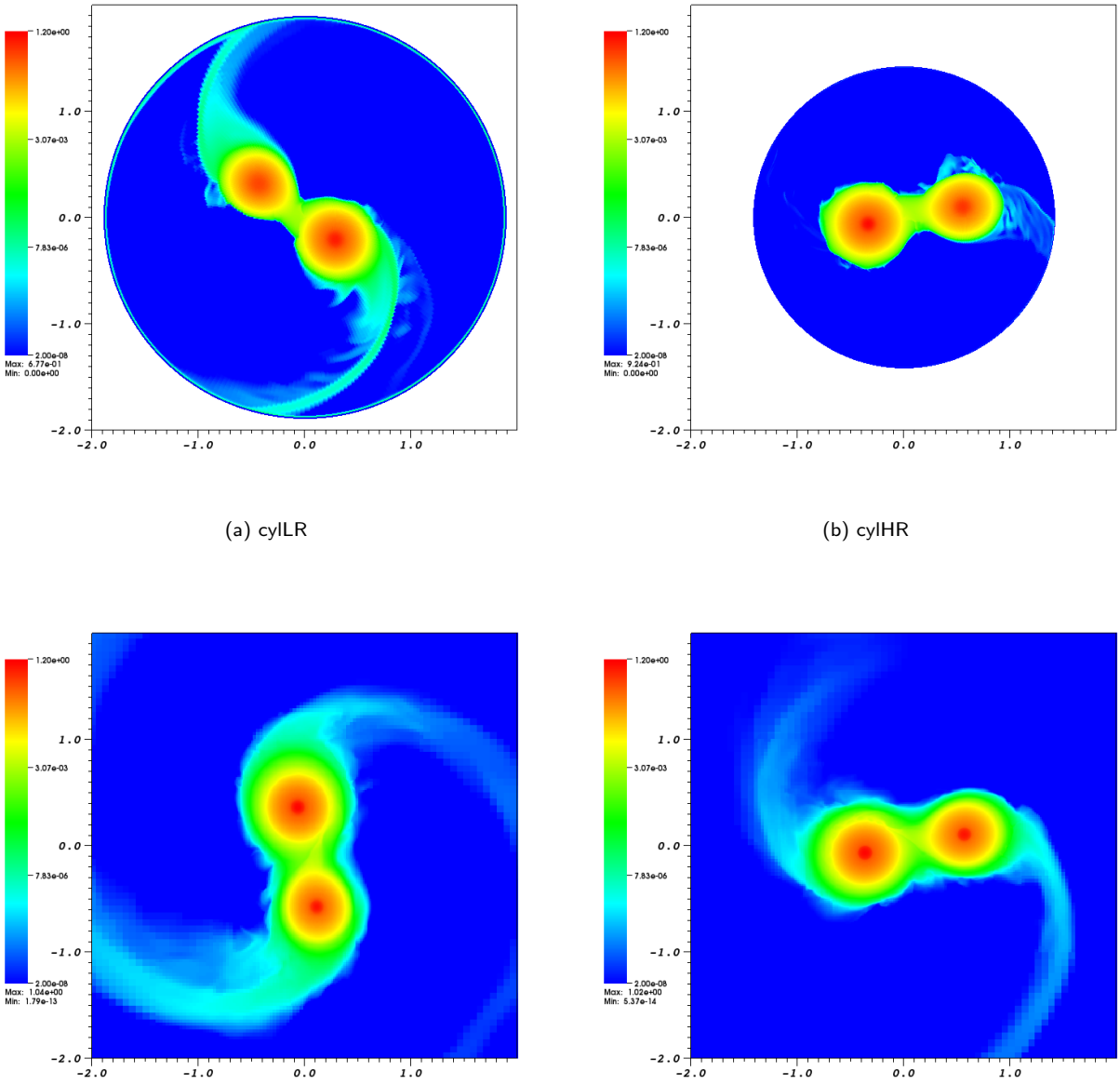

(a) cylLR

(b) cylHR

(c) octLR

(d) octHR

FIGURE 6.16: Equatorial cross section of the density field at $\mathrm{t}_{\mathrm{merge}} - 4.0$ or $(t + t_{\mathrm{zpt}})/P_0 = 20.58$. The mass loss through the L_2 and L_3 points is not "real", since it is not present in the cylHR simulation. The outflow is caused by numerical wind in the case of the cylLR, and in the case of Octotiger simulations it is a result of shock heating of the atmosphere, without radiative cooling.

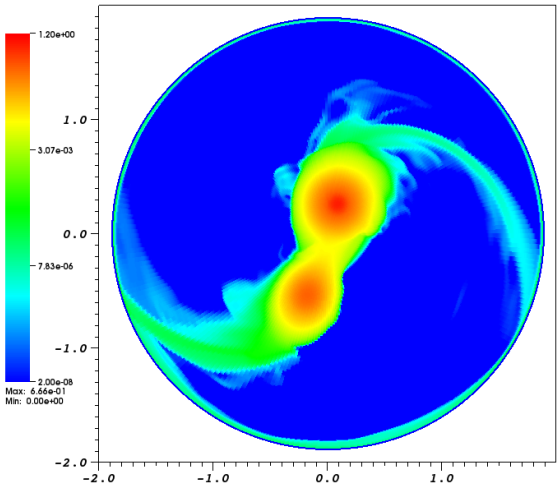

(a) cylLR

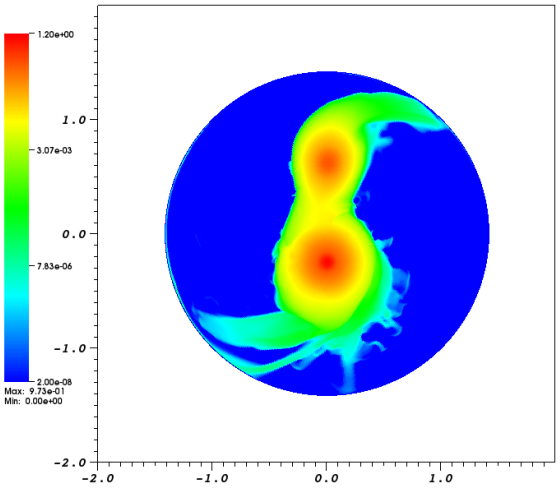

(b) cylHR

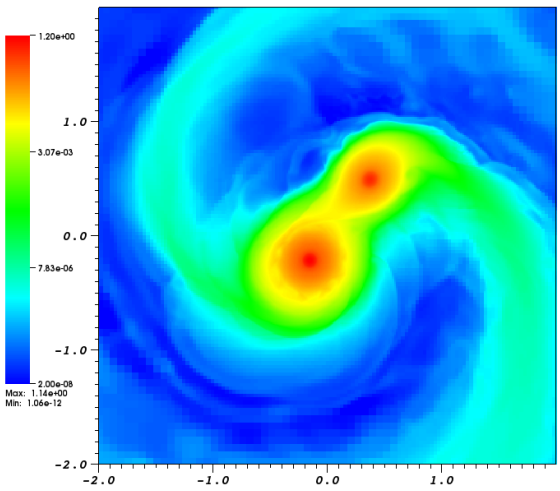

(c) octLR

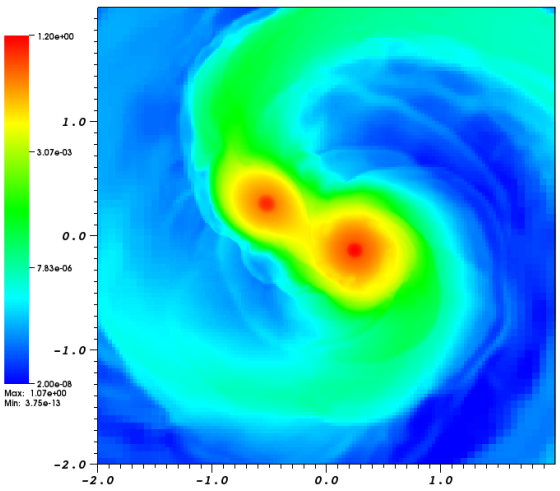

(d) octHR

FIGURE 6.17: Equatorial cross section of the density field at $\mathrm{t}_{\mathrm{merge}} - 0.4$ or $(t + t_{\mathrm{zpt}})/P_0 = 24.18$. All four simulations show a mass loss through the L_2 and L_3 points, indicating imminent merger. The core of the donor can be observed to be well-preserved in the Octotiger simulations and appears to be "dissolved" in the Flow-ER simulations.

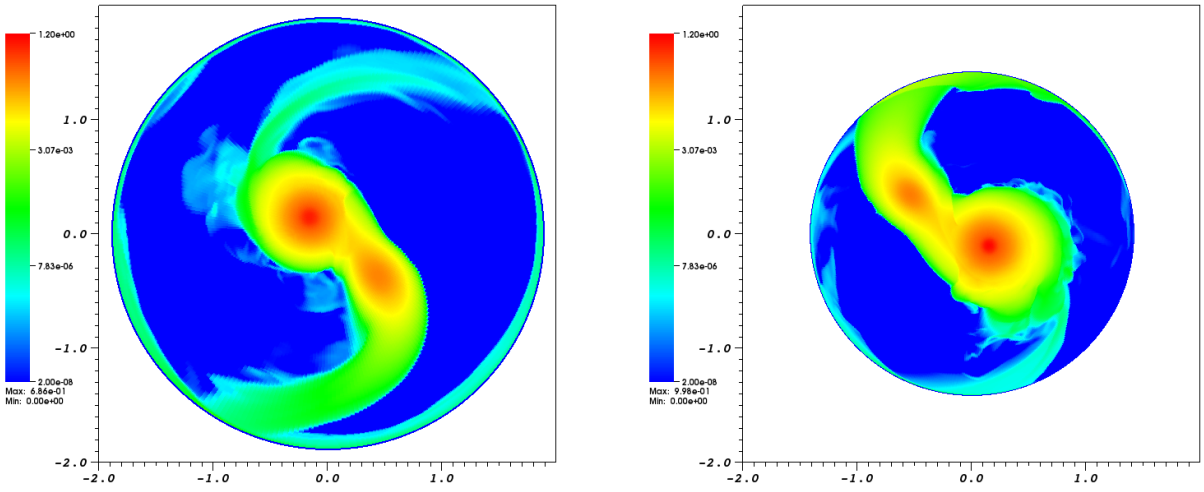

(a) cylLR

(b) cylHR

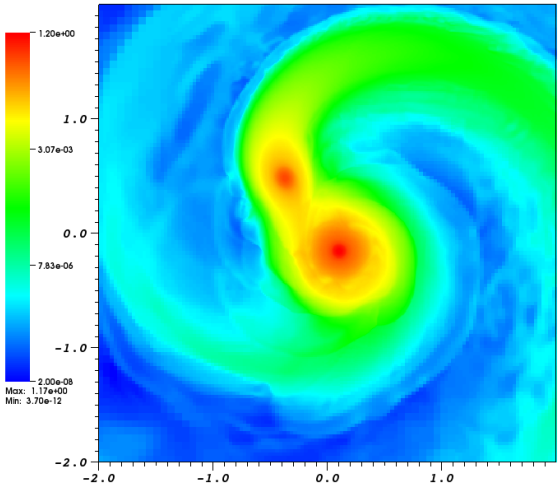

(c) octLR

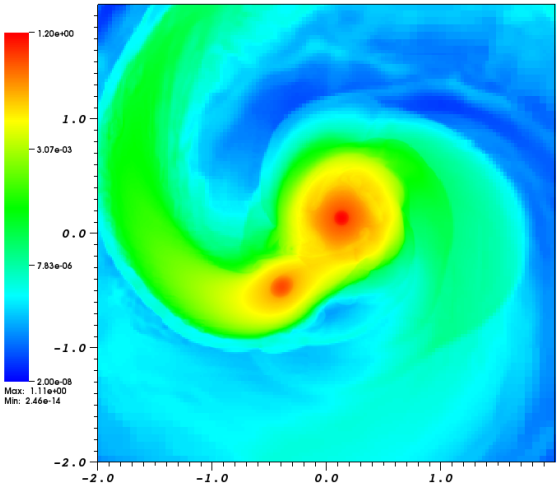

(d) octHR

FIGURE 6.18: Equatorial cross section of the density field at $\mathrm{t_{merge}}$ occurring at $(t + t_{\mathrm{zpt}})/P_0 = 24.58$, as determined in section 6.2.1.

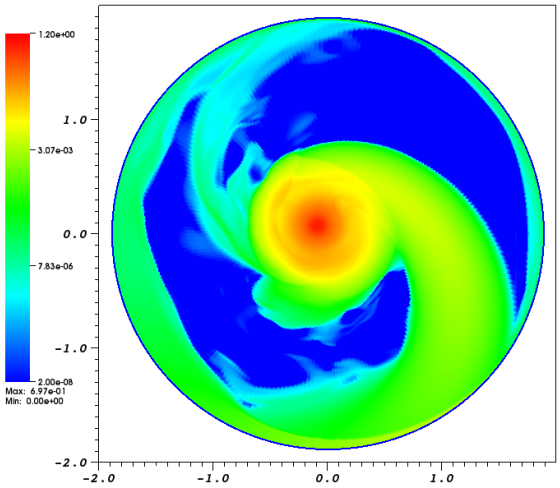

(a) cylLR

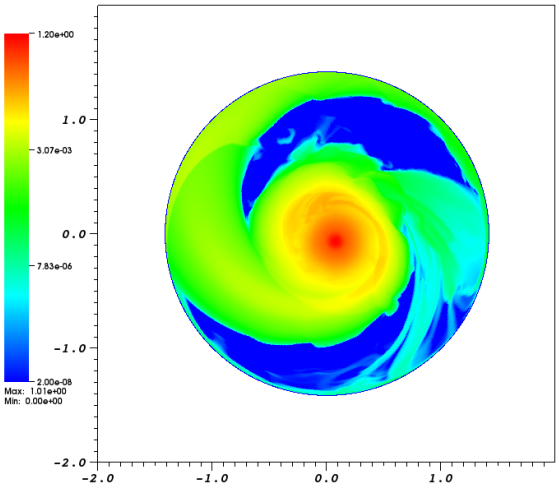

(b) cylHR

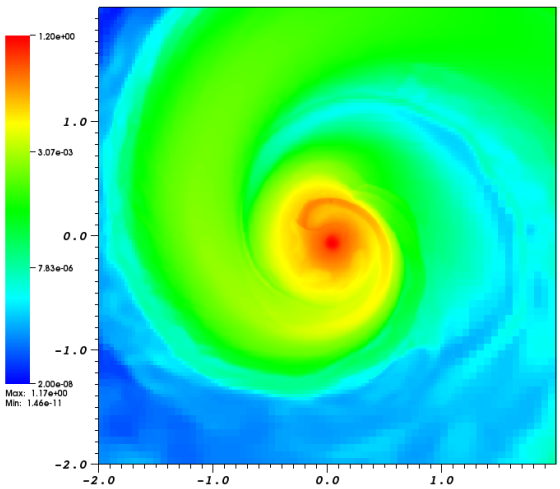

(c) octLR

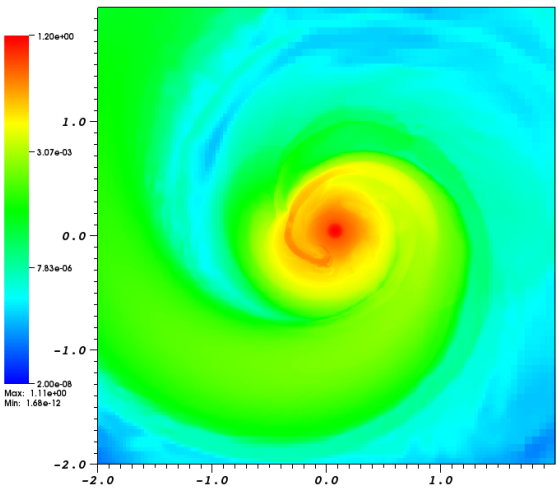

(d) octHR

FIGURE 6.19: Equatorial cross section of the density field at $\mathrm{t_{merge}} + 0.4$ or $(t + t_{\mathrm{zpt}})/P_0 = 24.98$, right after the merger. The disrupted core of the donor can be seen getting wrapped around the accretor as a part of a thick disk.

core of the donor can be seen being wrapped around the accretor as a long streak of inspiralling material. This former core material of the donor was poorly resolved in the Flow-ER simulations. The two cores did not collide head-on manner and instead the donor was tidally broken apart and its material dispersed by centrifugal force as an extended thick disk around the final merged object. Figure 6.20 shows the maridional cross section of the density. The central, non-spherical merged object has the same basic structure in all four simulations. The remnant of the secondary core can be seen in cross section of the octHR simulation, which was much more diffused or ill-resolved in the Flow-ER simulations. A difference between the Flow-ER and the Octotiger simulations is the thickness of the disk in the latter case, due to high temperatures caused by the shock heating during the merger. Notice that all the frames in Figures 6.15 – 6.20 qualitatively agree very well across all four Q0.7 simulations.

Figures 6.21 and 6.22 are identical to Figures 6.18 and 6.19, with the difference that the former pair of frames shows the density slices for the Q0.7 simulations at the length scale of the entire computational domain of the octHR model. The extended, spiral outflow structure, about an order of magnitude larger than the radius of the accretor, was formed in both the Octotiger simulations. A simulation with the Flow-ER code will be computationally very expensive if we achieve similar size of the grid which resolves the circumstellar disk in its entirety, while also trying to maintain enough resolution of the core. Figure 6.23 shows an maridional cross section of the density field right after the merger, again at the length scale of the octHR simulation. The full disk is visible in this view in the case of the OctHR simulation and most of the material remained in the equatorial plane. The shock-heated disk was almost twice as thick with Octotiger, as compared to the Flow-ER simulations. Since most of the material did not stray far from the equatorial plane, in the future we can use a rectangular grid with Octotiger, in order to save computational resources. These frames demonstrate the much better capability of Octotiger to resolve the circumbinary disk and the extended outflow structure using AMR.

After analyzing the diagnostic plots as well as the density frames for the Q0.7 simulations, we can conclude that both the hydrodynamic codes are convergent. In the case of the Flow-ER simulations, we see that there were significant differences in the time-dependent behavior of the central densities (Figures 6.7 and 6.8) and the mass transfer rate (Figure 6.10), at the two resolutions. The central densities started falling before the mass transfer began. In section 5.3 we concluded that this was due to the limited resolution of the cores. With the increase in the resolution from cylLR to the cylHR simulation, the central densities displayed evolution which is closer to the expected and "ideal" behavior. Hence given enough computing power, the differences can be made arbitrarily small. With increasing resolution, a hydrodynamic code can handle lower rates of mass transfer, in general. This was reflected in the longer $t_{\rm merge}$ of the cylHR simulation as compared to cylLR, as seen in Figure 6.10. The discontinuity at the core-envelope boundary was also relatively well-preserved the cylHR simulation as compared to its low resolution counterpart, as can be observed just before the merger in Figure 6.17. Despite these differences, the binary systems evolved with the Flow-ER simulations showed remarkable level of similarity with respect to remaining diagnostic quantities such as separation, mass ratio and angular momenta, as well as the cross sections of the density fields.

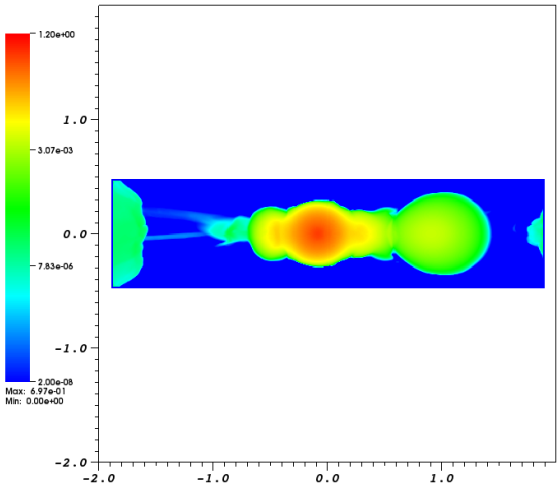

(a) cylLR

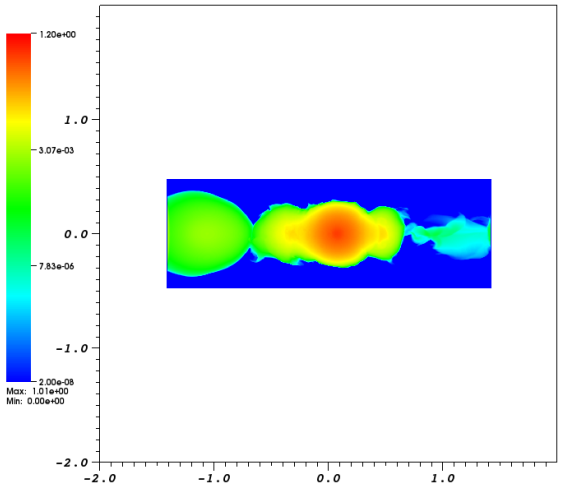

(b) cylHR

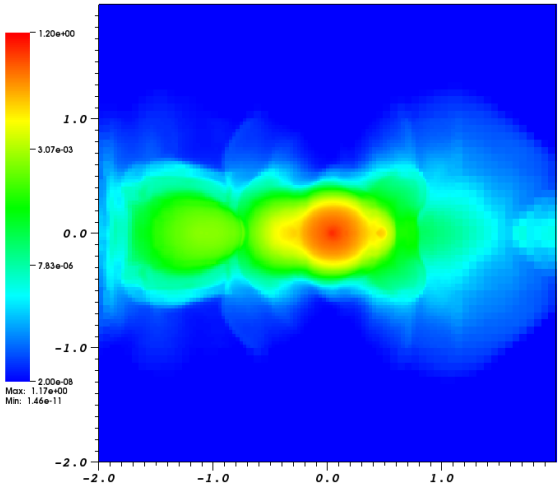

(c) octLR

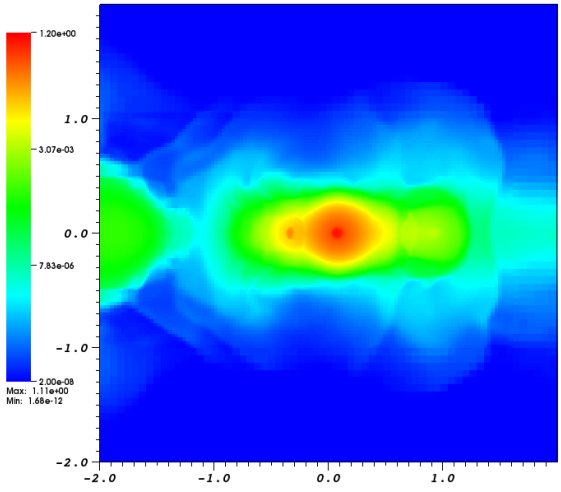

(d) octHR

FIGURE 6.20: Maridional cross section of the density field at $\mathrm{t}_{\mathrm{merge}} + 0.4$ or $(t+t_{\mathrm{zpt}})/P_0 = 24.98$, right after the merger. The heated outer atmosphere can be seen in the Octotiger simulations.

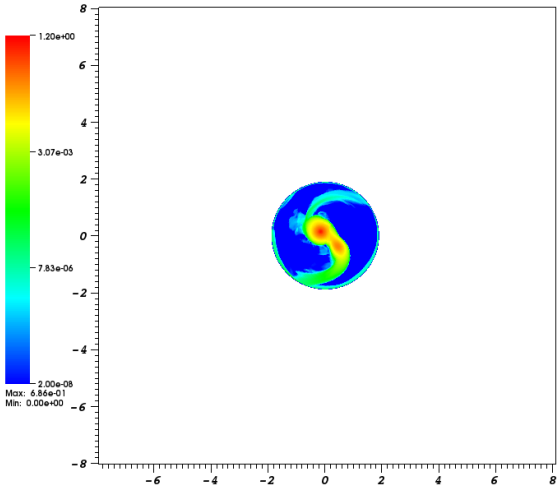

(a) cylLR

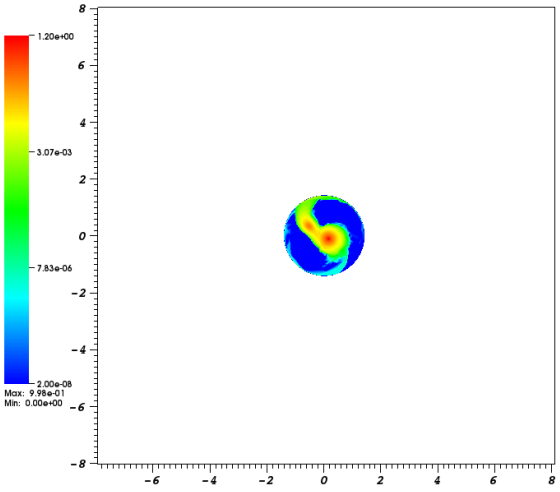

(b) cylHR

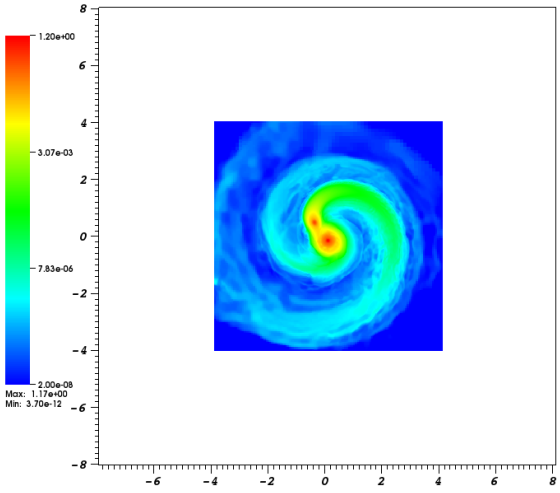

(c) octLR

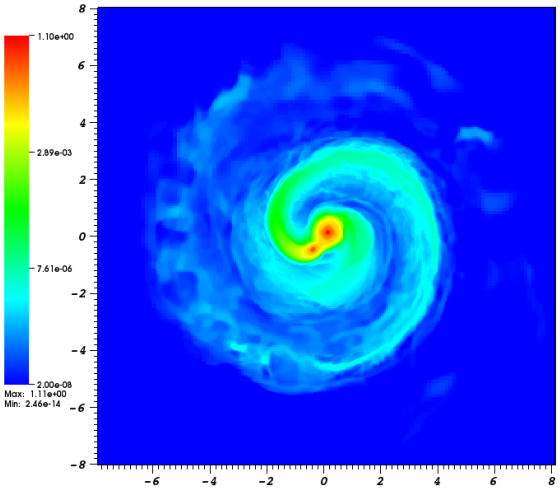

(d) octHR

FIGURE 6.21: Equatorial cross section of the density field at $\mathrm{t_{merge}}$ occurring at $(t + t_{\mathrm{zpt}})/P_0 = 24.58$, showing full octHR grid.

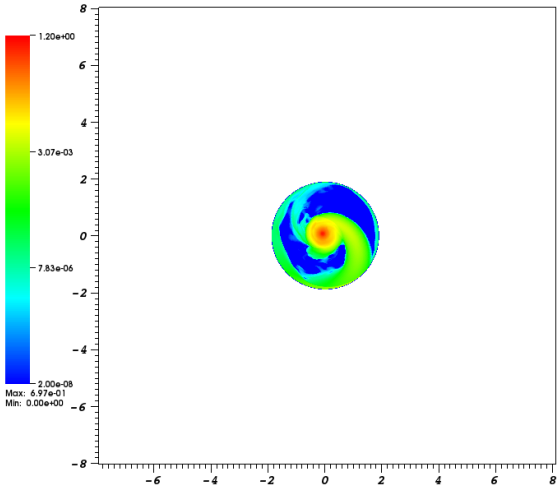

(a) cylLR

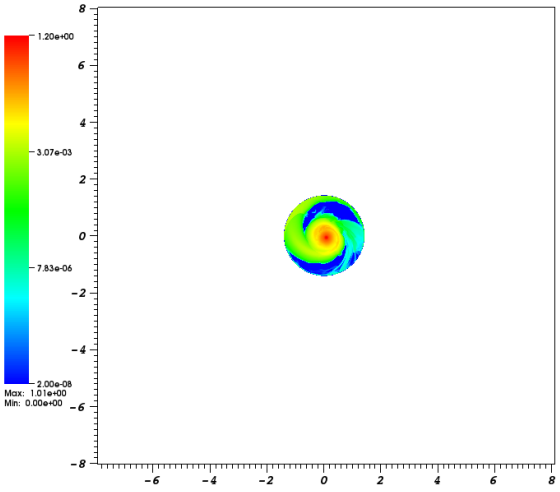

(b) cylHR

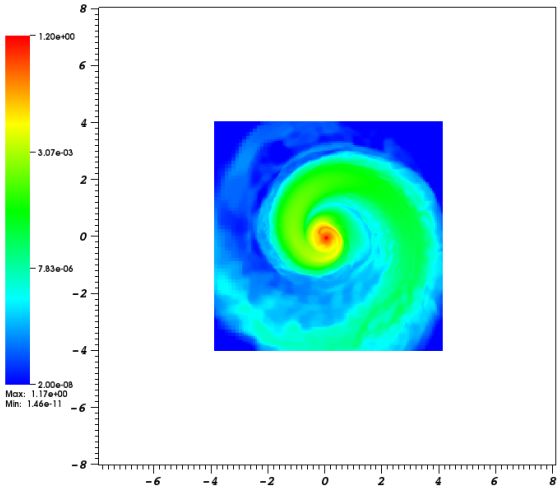

(c) octLR

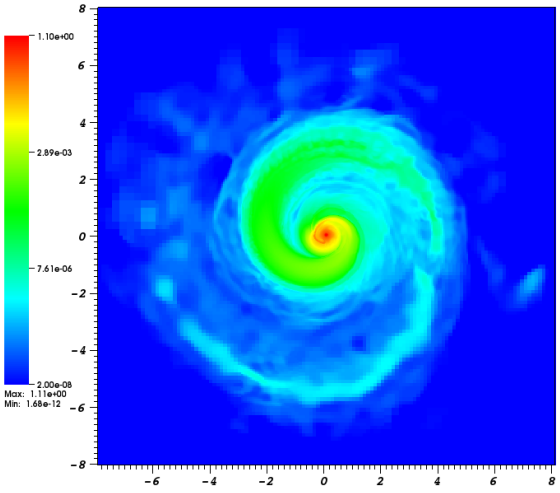

(d) octHR

FIGURE 6.22: Equatorial cross section of the density field at $\mathrm{t_{merge}} + 0.4$ or $(t + t_{\mathrm{zpt}})/P_0 = 24.98$, showing the extended disk and outflow structure.

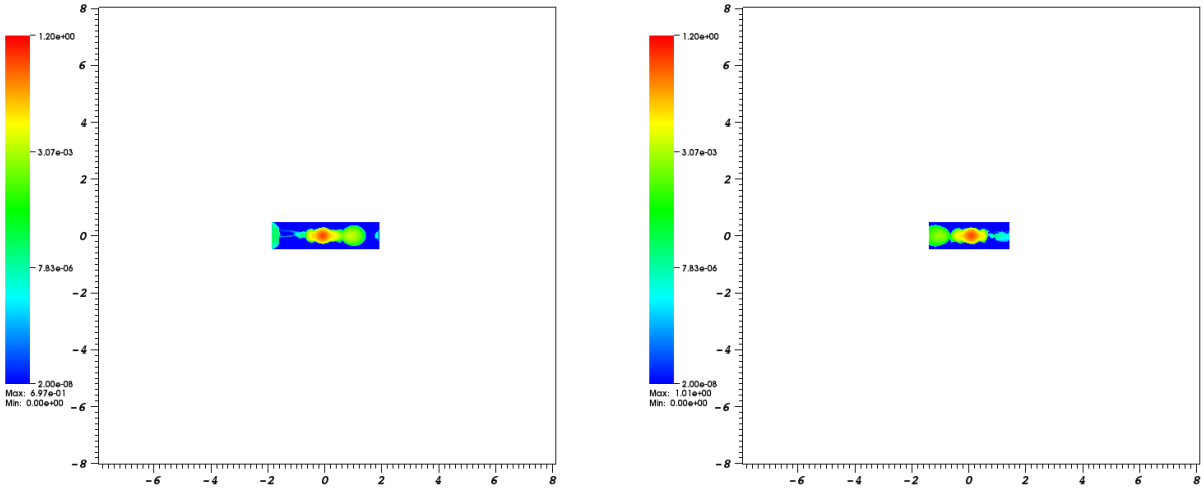

(a) cylLR (b) cylHR

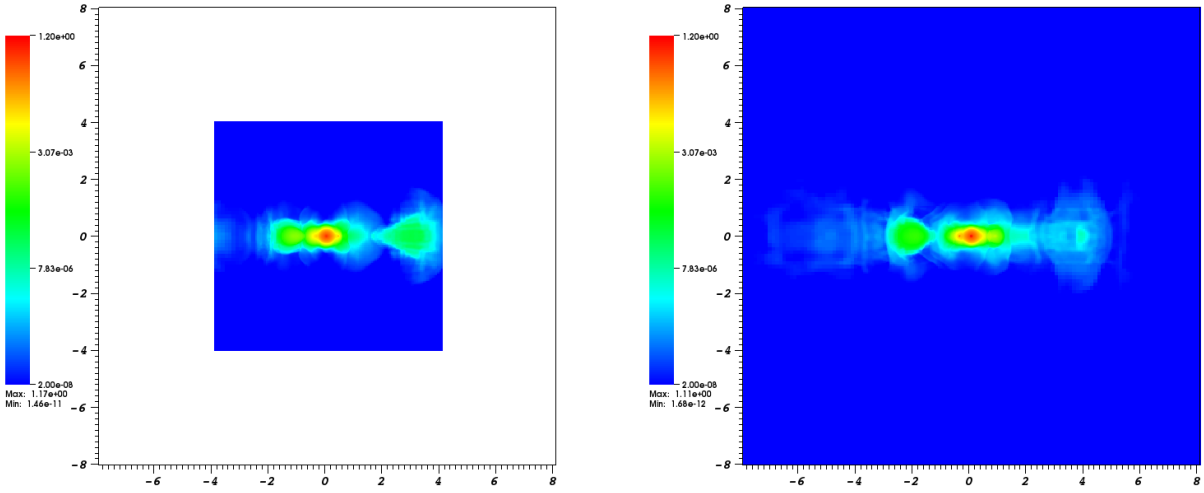

(c) octLR (d) octHR

FIGURE 6.23: Meridional cross section of the density field at $\mathrm{t_{merge}} + 0.4$ or $(t+t_{\mathrm{zpt}})/P_0 = 24.98$. The entire disk can be seen in the octHR simulation.

For the Octotiger simulations at the two resolutions, the differences lie, again, in the plots of the central densities and the mass transfer rate. Consider Figures 6.7 and 6.8. Starting at about $(t + t_{\rm zpt})/P_0 \approx 16.5$ when the steady mass transfer stream was established, the central densities for both the components showed small variations. Both Octotiger simulations show no systematic deviation of the central densities of either the donor or the accretor, before a significant amount of mass transfer had occurred. This indicates that the cores were sufficiently resolved at both the resolutions. The mass transfer rates plotted in Figure 6.10 show that the higher resolution simulation, octHR, lasts about an orbit longer as compared to the octLR simulation. However, this difference is relatively small, given that the resolution of each star is essentially doubled. All remaining diagnostic plots for the two Octotiger simulations lie virtually on top of each other. The cross sectional frames are also very similar at the two resolutions, indicating that Octotiger was also convergent.

In this section we presented and analyzed the results obtained from the Q0.7 simulations using two different codes, Flow-ER and Octotiger at two different resolutions. The initial binary models with a mass ratio of about 0.7 closely matched each other, and possessed a bipolytropic structure for both the stars. The masses of the components, period as well as composition of the initial models were consistent with observed contact binary systems as well as previously calculated evolutionary models. The choices of polytropic indices and the ratio of molecular weights were affected by the limited resolving capability of Flow-ER. The code Flow-ER evolved the binary adiabatically on a cylindrical mesh with an ideal gas EoS, while Octotiger used a dual energy formalism with shock heating to evolve the binary with an AMR grid. The binary components in Q0.7 simulations were driven together and the subsequent dynamical behavior was analyzed without any special assumptions. We summarize the results obtained from the Q0.7 simulations as follows.

1. We found that all models were unstable to mass transfer and the binaries merged with the tidal disruption of the donor.

2. The Flow-ER simulations showed a decrease in the central densities for both the donor and the accretor. Although this was a major numerical artifact, neither the overall behavior nor the ultimate fate of the binary systems were affected.

3. There were two subtle differences between the simulations carried out using the two codes. The first discrepancy was in the behavior of the cylHR simulation, which can be attributed to its longer t_{merge}. The second difference was between the behavior of the two codes, Flow-ER and Octotiger, just before the merger. This can be accounted for by the difference in the EoS, namely, the increased mass-transfer rate caused by the treatment of shock-heating in Octotiger.

4. The intermediate stages as well as final outcome, in terms of diagnostic plots and density cross sections, closely matched for all four simulations as well as to theoretical expectations.

Chapter 7
Conclusions and Future Work

Binary stellar systems are immensely important for understanding the local universe and various astronomical phenomena. With the exception of our sun, eclipsing binaries provide the only means of directly measuring both the mass and radius of a star, which allows us to quantitatively test the theories of stellar structure and evolution. When the stars in a binary are close enough, they transfer material between them. This gives rise to a plethora of interesting astronomical phenomena with periodic or aperiodic changes in the luminosity and spectral features of the system. The astrophysics community has made great progress in understanding single stars and their evolution. The mass of a star primarily determines its evolution, followed by its composition, with the rotation being the distant third. Thus most calculations can be performed sufficiently accurately with the assumption of spherical symmetry. In some cases, 1.5-dimensional calculations can be performed where the effect of the rotation on the effective potential is considered. The numerical models of a given mass and age closely match observations with respect to luminosity, size, surface temperature and composition, as well as in terms of the correlations between these measured parameters (Hansen *et al.*, 2004).

Binary interactions on the other hand are complicated and remain elusive as the problem is fundamentally 3-dimensional and non-linear. The evolution of close, mass-transferring binaries depends on factors which are difficult to determine a priori, such as mass loss from the system, loss of angular momentum through various mechanisms, mass ratio at the beginning of the mass transfer, the evolutionary status of the individual stars and tidal effects due to circumbinary discs. Nuclear reactions can also play an important role in binary systems involving a compact accreting object, which can significantly affect the energy budget of the event and the composition of the accretor. Thus we need to rely on numerical simulations in order to gain an insight into the evolution of binary systems. However, binary interactions are difficult to model on secular timescales from first principles for several reasons. First, there is a vast difference in the length scales that need to be resolved. For example, in the case of mass transfer due to Roche lobe overflow, the difference between the radius of the Roche lobe and stellar radius is several orders of magnitude smaller than the length scale of the binary. This situation is exacerbated if a circumbinary structure also needs to be resolved. The time steps involved in explicit numerical integration of the equations have to follow the Courant-Friedrichs-Lewy (CFL) condition for stability (Courant *et al.*, 1928). Thus the individual time step is many orders of magnitude shorter than even a single orbital period. Unlike in the case of single star evolution, the inherent asymmetry of a binary system requires multi-dimensional calculations. Thus we have to count on computationally feasible simulations on dynamical timescales. A semi-analytical approach ($\mathrm{e.g.}$ as described in section 3.3 for determining q_{crit}) works, but it is quantitatively less accurate as compared to a fully self-consistent treatment, since parameterization and simplifying assumptions are often made. This is useful in giving a general description of the behavior of the binary, although detailed or specialized calculations are often needed for solving specific issues.

We chose to address one subset of interacting binary systems, namely W UMa type systems or contact binaries. The initial motivation was the luminous red nova V1309 Sco, which was proved to be the merger of a contact binary system. The final eruption was assumed to be the disruption of the core of the secondary inside the primary star. There have been past attempts to simulate the merger of the V1309 Sco progenitor binary system. Most notably, Nandez *et al.* (2014) used the smooth particle hydrodynamics (SPH) code StarSmasher to simulate how the V1309 Sco binary evolved through the common envelope phase with a red giant primary and a degenerate as well as a main sequence secondary. However, the results of SPH investigations are not identical with the grid based approach. For example, Motl *et al.* (2016) compare the results of interactions between mass transferring double degenerate binaries with polytropic EoS. They use Flow-ER, which is the same grid based code used in this dissertation, and an SPH code called SNSPH for these simulations. They show that there can be quantifiable differences between the results obtained from SPH and grid-based codes at relatively low mass transfer rates, and each method can be biased in terms of certain physical processes because of the inherent nature of the numerical methods. Staff *et al.* (2017) show similar effects for the dredge up process in the case of double white dwarf mergers.

This dissertation developed a set of grid-based numerical tools that enable us to reliably simulate the evolution of contact binary systems on a dynamical scale, i.e. at least a few tens of orbits, with a general core-envelope structure for both the stars. Such an investigation could shed light on the complex evolutionary history of W UMa type systems and, in particular, on dynamical aspects that are not well-understood, such as their structure and stability criteria. We created the initial binary systems with the BSCF method with each component represented as a bipolytrope (the Q0.7 models), and used these systems as initial conditions for hydrodynamic evolutions. A bipolytrope represents the core-envelope structure in a single star. The internal structure of each star in the simulations was closely matched with that expected from the evolutionary models for a slightly evolved star with a heavy helium core. The masses of the components as well as the periods of the initial models were consistent with the observations. We used two distinct Eulerian hydrocodes for performing the numerical simulations. The first code was Flow-ER, which used a fixed cylindrical geometry and the other was Octotiger, which was a more advanced, AMR-capable code. As explained in section 6.1, the choices for the polytropic indices and the spatial extents of the cores for our initial models were restricted by the limitations of the code Flow-ER. The initial binary systems were chosen to match as closely as possible across the two codes, as well as at two different resolutions, so that the results could be compared directly and could be used as a benchmark for each code. Chapter 6 concludes that there was excellent agreement between theoretical expectations and the simulations, as well as across the simulations, with respect to the the ultimate outcome and also the intermediate behavior during the dynamical evolution of the binary systems. In the suite of simulations, we observed certain differences among the time dependent global quantities, i.e. the diagnostic parameters, as well as the evolution of the density distribution of the binaries. We can account for these differences in terms of the differences between the two codes, such as the EoS and the treatment of shock heating.

We did not recreate the particular case of the merger of the progenitor system of the V1309 Sco eruption, which would require simulating the evolution of a binary with the mass ratio of about 0.1 (Stępień, 2011). The initial scope of the project was limited to the Flow-ER code.

However, it turned out that the cylindrical geometry, such as implemented in the code Flow-ER, is not ideal for the simulations of bipolytropic binaries. This is mainly because of the following reasons:

- The effective resolution of a star is affected in the azimuthal direction, as each star is placed off-center in a binary configuration. Although the resolution is sufficient for evolving binaries having polytropic EoS, the effect on the core in a bipolytrope is much worse because of its small initial size. Since the grid is static, we cannot choose to put the resolution where it is needed.

- As shown in Chapter 5.3, for the evolution of bipolytropic binary systems in Flow-ER, the central densities of both the stars fall over dynamical timescale because the implemented numerical methods cannot preserve the steep density gradients near the center of the core. This puts a question on the interpretation of new results obtained through the simulations, without extensive testing. With the Q0.7 simulations, we conclude that increase in resolution mitigated the fall in the central density, and furthermore, the dynamical evolution of the binary system was not significantly affected by this fall.

- Simulations with increasing resolution are prohibitively expensive with Flow-ER. This is not only because of the increased size of the dataset, but also because the CFL condition near the axis of the grid forces reduction of timestep-size to maintain numerical stability.

For the V1309 Sco progenitor, we can assume an approximate mass-radius relationship of $R \propto M$ for near main sequence stars. With $q \approx 0.1$ the secondary is only one tenth the size of the more massive component, which has a further negative impact on its resolution. This study established the limitations of Flow-ER and due the issues outlined above, it would be difficult or impossible to reliably simulate the V1309 Sco progenitor binary using this code.

As described in sections 5.2 and 5.3, the numerical code Octotiger is well-fitted for investigating bipolytropic binary evolutions and can also be ideal for simulating various other astrophysical scenarios. The major advantages of Octotiger are as follows (Marcello at al. 2017, in preparation):

- The latest iteration of the BSCF method implemented in Octotiger can produce an initial binary system over a wide range of initial parameters which can be specified a priori. These include the mass ratio, core mass fractions and Roche lobe filling factors. This is a huge advantage, as we no longer need to adjust the boundary conditions (as described in section 4.4) in order to generate a quiet, low-noise, initial binary with desirable properties. The new method can also produce initial binaries in a contact configuration, thus eliminating the need for initial driving.

- The key quantities like the mass, linear momentum, angular momentum, and energy are conserved to machine precision ($\approx 10^{-14}$). This is important for investigating long term dynamical stability of an evolving binary system. For example, using Octotiger, an AM Canum Venticorum (AM CVn, in this case, a double white dwarf system) binary with an initial mass ratio of 0.2 and undergoing a stable mass transfer was evolved for over 500 orbits.

- The use of the HPX runtime system allows us to utilize the computational resources more efficiently. This is achieved through better scaling and performance, as compared to more conventional programming models such as MPI (Message Passing Interface), without suffering from conventional computing bottlenecks. Thus we can continue to conduct simulations on large supercomputers in the near future, as Octotiger has scaled well on up to 7200 cores with no theoretical upper limit.

This dissertation proved the viability and robustness of our numerical techniques and highlighted the suitability of Octotiger for investigating binary interactions with bipolytropic components. We have started exploring the dynamical evolution of the progenitor of V1309 Sco, and we will investigate this interesting object further in the near future. In the remainder of this section we will elaborate on some specific ideas that can be worked on as a continuation of this project. These include various binary scenarios which we can investigate with Octotiger in the future, either in the current form of the code or by including additional physics. These systems include contact binaries with the components on or near the main-sequence (similar to those studied in this dissertation), compact binary systems such as double white dwarfs, the short-lived common envelope (CE) phase of the binary evolution, and also cataclysmic variables.

The new BSCF method implemented in Octotiger is especially powerful for generating the initial binary systems with properties that can be precisely controlled. As a result we can achieve a contact binary configuration by generating an initial model with each component having the same Roche lobe filling factor, which can be chosen to be slightly less than unity. Thus while evolving in a hydrodynamic code, the binary will obtain a contact configuration instead of a semi-detached one, as both the stars will overflow their Roche lobes almost simultaneously. Previously, the HSCF method in Flow-ER could produce a binary configuration which was already in contact. However, the mass ratio always equaled unity due to the fact that both the envelopes, and hence both the stars, needed to have the same entropy (similar to Kuiper's paradox discussed in section 2.2). Using the new BSCF method in Octotiger, we can not only create close but separated binary systems, but also contact binaries with a wide range of mass ratios. This is achieved by making the envelope entropy of the secondary match that of the primary, thus determining the core-size of the secondary, which cannot be specified a priori. These models can be useful for investigating the redistribution of energy and the large-scale circulation patterns in contact binary systems. Motl *et al.* (2017b) presented the results of long-term dynamical evolution of a contact binary having a mass ratio of unity, and polytropic EoS with the code Flow-ER. The steady flow between the two stars is naturally established within a few dynamical timescales without any special assumptions. With Octotiger, we can study such flow patterns and stability criteria of contact binaries with a wide range of mass ratios and more realistic internal structure. In terms of particular cases, in addition to V1309 Sco, a very interesting case that we will study is KIC 9832227, which may be the first prediction of a luminous red nova (LRN) event. Molnar *et al.* (2017) showed that the lightcurve of this contact binary system is changing its orbital period in a similar way to that of the V1309 Sco progenitor. The current observed period of this contact binary is 0.458 d and the mass ratio is about 0.23. The estimated year of coalescence is 2022 ± 0.6. The Octotiger simulations can be used to investigate if the contact binary is indeed unstable and if the simulated behavior matches the observed characteristics.

Our research group has been studying mergers of binary white dwarf systems for about two decades. These simulations are useful in determining the role of merging white dwarfs as progenitors of R Coronae Borealis (RCB) variable stars (Staff *et al.*, 2012, 2013). RCB stars are supergiant stars which are very rare and display many unusual characteristics such as sudden declines in brightness due to dust formation, lack of hydrogen and unusual isotopic abundances (Clayton, 2012). The two contending theories of their formation are – the final helium-shell flash (FF) and the double degenerate (DD) model, which is a coalescence of two white dwarfs. The dynamical interactions of two white dwarfs during the merger are simulated using both Flow-ER and Octotiger. The merged object is mapped on a 1-dimensional stellar evolution code, MESA, in order to calculate surface abundances of these stars after secular evolution. These abundances depend on the properties of the progenitor system and the physical processes occurring during the merger, such as mixing and dredge up. Octotiger will be used for the continuation of these studies in order to confirm or reject the DD model.

Octotiger simulations can be used to probe another issue pertaining to close binary evolution – the common envelope (CE) phase. As the name suggests, during this short-lived phase of close binary evolution, the two stars share a common envelope. In this respect, this phase is similar to a contact binary system although in the latter case, both the stars fill their Roche lobes. The CE phase is proposed as the formation mechanism for low-mass and high mass X-ray binaries (LMXB, HMXB) and cataclysmic variables, as well as binary white dwarfs and black holes. The existence of such compact binary systems contains a contradiction that the progenitor of the compact object requires the parent star to essentially go through a giant or supergiant stage in the past. However, these systems typically have a short orbital period of a few hours and the corresponding separation is comparable to a solar radius, which is much smaller than the radius of a giant star. Thus it is envisioned that the higher mass star evolves off the main sequence earlier and during the giant or AGB phase, engulfs the main sequence companion, forming a common envelope. The CE phase is characterized by severe loss of mass and angular momentum and this phase of binary evolution is exceptionally complex and not yet well-understood (Ivanova *et al.*, 2013). Our collaborators have studied the CE phase of red giant stars using SPH and uniform grid based codes (Passy *et al.*, 2011). Octotiger can continue similar investigations of the CE evolution with AMR grid and with little modification. Although the compact core of a giant star is about two orders of magnitude smaller than its radius, with the combination of AMR and by utilizing large numbers of cores with the HPX runtime system, it is possible to simulate more realistic CE evolution with fully resolved cores, along with accompanying complex, non-linear processes. One interesting class of mass transferring binaries formed as a result of the CE phase are cataclysmic variables (CV). These systems consist of an accreting white dwarf with a Roche lobe filling companion. An accretion disk is formed around the white dwarf because of the angular momentum of the accreting gas. CV systems can also be modeled with Octotiger in the future and the physics of accretion disks can be studied in detail.

The stellar interactions and merger events are ultimately observed through the light they emit. We need to have a good representation of the temperature of the gas and the radiation field, in order to obtain observable quantities such as luminosity and spectra. This makes solving the coupled equations of radiative transport necessary. Since the results obtained via the Q0.7 simulation agree very well between Flow-ER and Octotiger, we can say that the exclusion of radiative

transport equations did not affect the simulations carried out in this dissertation significantly. However, without the radiative cooling, the shock-heated common envelope can be clearly observed in Octotiger simulations. In extreme cases, for example, during mass transfer on compact objects or if high mass stars are involved, the radiation pressure can dominate the processes and the luminosities involved could even approach the Eddington luminosity. The treatment of radiative transfer thus becomes desirable for obtaining reliable and physical results, as well as for reproducing optically observable properties. A variable Eddington tensor based radiation hydrodynamics module for Octotiger is being developed here at LSU, which will greatly improve the accuracy and also expand the applicability of this code. When finished, various high-energy phenomena can be modeled with the code. For example, in addition to the above mentioned cases, the interactions of strong shocks with circumstellar material can be simulated when massive stars explode in super-luminous supernova events (SLSNe). We would also like to develop a module for post-processing the Octotiger data in order to construct spectra and lightcurves from our simulations. Post-processing will allow us to use comprehensive opacity tables to compute absorption and emission features, without extensive transport calculations during the evolution. This would enable us to directly compare the results obtained from the simulations with the observations.

In conclusion, this dissertation is a step forward in the direction of investigating dynamical interactions of mass transferring binary systems. We generated quiet initial conditions for binaries with each component having a bipolytropic EoS, which can better model the internal core-envelope structure of stars. We established the limitations of the code Flow-ER in terms of dynamically evolving these systems. We proved the viability of Octotiger as a tool for reliably simulating bipolytropic binaries, and pointed out the steps to be taken for its broader applicability. In the future, the continuation of this project will allow us to numerically study and better understand evolution of close binary systems, as well as many more astrophysical phenomena.

Bibliography

Ansorg, M., Kleinwächter, A., & Meinel, R. 2003. Uniformly rotating axisymmetric fluid configurations bifurcating from highly flattened Maclaurin spheroids. MNRAS, **339**(Feb.), 515–523.

Applegate, J. H. 1988. Why stars become red giants. ApJ, **329**(June), 803–807.

Bahcall, J. N., Pinsonneault, M. H., & Wasserburg, G. J. 1995. Solar models with helium and heavy-element diffusion. *Reviews of Modern Physics*, **67**(Oct.), 781–808.

Beech, M. 1988. A double polytropic model for low-mass stars. MNRASAp&SS, **146**(July), 299–310.

Bilir, S., Karataş, Y., Demircan, O., & Eker, Z. 2005. Kinematics of W Ursae Majoris type binaries and evidence of the two types of formation. MNRAS, **357**(Feb.), 497–517.

Binnendijk, L. 1970. The orbital elements of W Ursae Majoris systems. *Vistas in Astronomy*, **12**, 217–256.

Bode, M. F., & Evans, A. (eds). 1989. *Classical novae*.

Chandrasekhar, S. 1939. *An introduction to the study of stellar structure*.

Childs, Hank, Brugger, Eric, Whitlock, Brad, Meredith, Jeremy, Ahern, Sean, Pugmire, David, Biagas, Kathleen, Miller, Mark, Harrison, Cyrus, Weber, Gunther H., Krishnan, Hari, Fogal, Thomas, Sanderson, Allen, Garth, Christoph, Bethel, E. Wes, Camp, David, Rübel, Oliver, Durant, Marc, Favre, Jean M., & Navrátil, Paul. 2012. VisIt: An End-User Tool For Visualizing and Analyzing Very Large Data. *Pages 357–372 of: High Performance Visualization–Enabling Extreme-Scale Scientific Insight*.

Clayton, G. C. 2012. What Are the R Coronae Borealis Stars? *Journal of the American Association of Variable Star Observers (JAAVSO)*, **40**(June), 539.

Cohl, H. S., & Tohline, J. E. 1999. A Compact Cylindrical Green's Function Expansion for the Solution of Potential Problems. ApJ, **527**(Dec.), 86–101.

Courant, R., Friedrichs, K., & Lewy, H. 1928. Über die partiellen Differenzengleichungen der mathematischen Physik. *Mathematische Annalen*, **100**, 32–74.

Criss, R. E., & Hofmeister, A. M. 2015. Analytical representations for simple and composite polytropes and their moments of inertia. *New Astronomy*, **36**(Apr.), 26–31.

Darwin, G. H. 1880. On the secular effects of tidal friction. *Astronomische Nachrichten*, **96**(Jan.), 217.

Després, Bruno, & Labourasse, Emmanuel. 2014 (Sept.). *Angular Momentum preserving cell-centered Lagrangian and Eulerian schemes on arbitrary grids*. Tech. rept.

D'Souza, M. C. R., Motl, P. M., Tohline, J. E., & Frank, J. 2006. Numerical Simulations of the Onset and Stability of Dynamical Mass Transfer in Binaries. ApJ, **643**(May), 381–401.

Eggen, O. J. 1967. Contact binaries, II. , **70**, 111.

Eggleton, P. P. 1983. Approximations to the radii of Roche lobes. ApJ, **268**(May), 368.

Eggleton, P. P., Faulkner, J., & Cannon, R. C. 1998. A small contribution to the giant problem. MNRAS, **298**(Aug.), 831–834.

Emden, R. 1907. *Gaskugeln: Anwendungen der Mechanischen Warmetheorie auf Kosmologische und Meteorologische Probleme*.

Eriguchi, Y., & Sugimoto, D. 1981. Another Equilibrium Sequence of Self-Gravitating and Rotating Incompressible Fluid. *Progress of Theoretical Physics*, **65**(June), 1870–1875.

Flannery, B. P. 1976. A Cyclic Thermal Instability in Contact Binary Stars. ApJ, **205**(Apr.), 217–225.

Guillot, T. 1999. A comparison of the interiors of Jupiter and Saturn. Planet. Space Sci., **47**(Oct.), 1183–1200.

Guillot, T. 2005. THE INTERIORS OF GIANT PLANETS: Models and Outstanding Questions. *Annual Review of Earth and Planetary Sciences*, **33**(Jan.), 493–530.

Hachisu, I. 1986a. A versatile method for obtaining structures of rapidly rotating stars. ApJS, **61**(July), 479–507.

Hachisu, I. 1986b. A versatile method for obtaining structures of rapidly rotating stars. II - Three-dimensional self-consistent field method. ApJS, **62**(Nov.), 461–499.

Hansen, C. J., Kawaler, S. D., & Trimble, V. 2004. *Stellar interiors : physical principles, structure, and evolution*.

Henrich, L. R., & Chandrasekhar, S. 1941. Stellar Models with Isothermal Cores. ApJ, **94**(Nov.), 525.

Hjellming, M. S., & Webbink, R. F. 1987. Thresholds for rapid mass transfer in binary systems. I - Polytropic models. ApJ, **318**(July), 794–808.

Ivanova, N., Justham, S., Chen, X., De Marco, O., Fryer, C. L., Gaburov, E., Ge, H., Glebbeek, E., Han, Z., Li, X.-D., Lu, G., Marsh, T., Podsiadlowski, P., Potter, A., Soker, N., Taam, R., Tauris, T. M., van den Heuvel, E. P. J., & Webbink, R. F. 2013. Common envelope evolution: where we stand and how we can move forward. , **21**(Feb.), 59.

Jacobson, R. A. 2003. JUP230 orbit solution. *ftp://ssd.jpl.nasa.gov/pub/eph/satellites/-nio/jup230.long.txt*.

Kadam, K., Motl, P. M., Frank, J., Clayton, G. C., & Marcello, D. C. 2016. A numerical method for generating rapidly rotating bipolytropic structures in equilibrium. MNRAS, **462**(Oct.), 2237–2245.

Kaspi, Y., Hubbard, W. B., Showman, A. P., & Flierl, G. R. 2010. Gravitational signature of Jupiter's internal dynamics. GRL, **37**(Jan.), L01204.

Kippenhahn, R., & Weigert, A. 1994. *Stellar Structure and Evolution*.

Kong, D., Liao, X., Zhang, K., & Schubert, G. 2014. The shape, internal structure and gravity of the fast spinner β Pictoris b. MNRAS, **445**(Nov.), L26–L30.

Kozai, Y. 1962. Secular perturbations of asteroids with high inclination and eccentricity. AJ, **67**(Nov.), 591.

Kuiper, G. P. 1941. On the Interpretation of β Lyrae and Other Close Binaries. *ApJ*, **93**(Jan.), 133.

Lane, J. H. 1870. *The American Journal of Science and Arts*, **50**(57).

Lawlor, T. M. 2005. A new model for V838 Monocerotis: a born-again object including an episode of accretion. MNRAS, **361**(Aug.), 695–700.

Li, L., Zhang, F., Han, Z., & Jiang, D. 2007. Formation and Evolution of W Ursae Majoris Contact Binaries. ApJ, **662**(June), 596–601.

Lidov, M. L. 1962. The evolution of orbits of artificial satellites of planets under the action of gravitational perturbations of external bodies. Planet. Space Sci., **9**(Oct.), 719–759.

Lucy, L. B. 1968. The Structure of Contact Binaries. ApJ, **151**(Mar.), 1123.

Lucy, L. B. 1976. W Ursae Majoris systems with marginal contact. ApJ, **205**(Apr.), 208–216.

Maceroni, C., & van 't Veer, F. 1996. The properties of W Ursae Majoris contact binaries: new results and old problems. A&A, **311**(July), 523–531.

Maeder, A. 1971. The Schönberg-Chandrasekhar Limit and Rotation. A&A, **14**(Oct.), 351.

Mason, E., Diaz, M., Williams, R. E., Preston, G., & Bensby, T. 2010. The peculiar nova V1309 Scorpii/nova Scorpii 2008. A candidate twin of V838 Monocerotis. A&A, **516**(June), A108.

Mestel, L. 1968. Magnetic braking by a stellar wind-I. MNRAS, **138**, 359.

Milne, E. A. 1930. The analysis of stellar structure. *The Observatory*, **53**(Nov.), 305–308.

Mochnacki, S. W., & Doughty, N. A. 1972. Models for five W Ursae Majoris systems. MNRAS, **156**, 243–252.

Molnar, L. A., Van Noord, D., Kinemuchi, K., Smolinski, J. P., Alexander, C. E., Kobulnicky, H. A., Cook, E. M., Jang, B., & Steenwyk, S. D. 2017 (Jan.). KIC 9832227: a red nova precursor. *Page 417.04 of: American Astronomical Society Meeting Abstracts*. American Astronomical Society Meeting Abstracts, vol. 229.

Motl, P. M. 2001. *Numerical simulations of dynamical mass transfer in binaries*. Ph.D. thesis, Louisiana State University and Agricultural and Mechanical College.

Motl, P. M., Tohline, J. E., & Frank, J. 2002. Numerical Methods for the Simulation of Dynamical Mass Transfer in Binaries. ApJS, **138**(Jan.), 121–148.

Motl, P. M., Frank, J., Staff, J., Clayton, G. C., Fryer, C. L., Even, W., Diehl, S., & Tohline, J.E. 2016. ApJS, **In press**.

Motl, P. M, Frank, J., Staff, J., Clayton, G. C, Fryer, C. L, Even, W., Diehl, S., & Tohline, J. E. 2017a. A Comparison of Grid-Based and SPH Binary Mass-Transfer and Merger Simulations. *ArXiv e-prints*, Feb.

Motl, P. M., Kadam, K., Frank, J., & Clayton, G. C. 2017b (Jan.). Flow Patterns in Simulated Contact Binaries. *Page 326.01 of: American Astronomical Society Meeting Abstracts*. American Astronomical Society Meeting Abstracts, vol. 229.

Müller, G., & Kempf, P. 1903. A new variable star unusually short period. ApJ, **17**(Apr.), 201–211.

Munari, U., & Henden, A. 2005 (Oct.). The first three years of the outburst and light-echo evolution of V838 Mon and the nature of its progenitor. *Pages 331–336 of:* Burderi, L., Antonelli, L. A., D'Antona, F., di Salvo, T., Israel, G. L., Piersanti, L., Tornambè, A., & Straniero, O. (eds), *Interacting Binaries: Accretion, Evolution, and Outcomes*. American Institute of Physics Conference Series, vol. 797.

Murphy, J. O. 1983. Composite and Analytical Solutions of the Lane-Emden Equation with Polytropic Indices N=1 and N=5. *Proceedings of the Astronomical Society of Australia*, **5**, 175–179.

Nakano, S., Jacques, C., & Pimentel, E. 2008. Supernova 2008fv in NGC 3147. *Central Bureau Electronic Telegrams*, **1520**(Sept.), 1.

Nandez, J. L. A., Ivanova, N., & Lombardi, Jr., J. C. 2014. V1309 ScoUnderstanding a Merger. ApJ, **786**(May), 39.

NASA. 2014. Planetary fact sheets. *http://nssdc.gsfc.nasa.gov/planetary/factsheet/-jupiterfact.html*.

Nellis, W. J. 2000. Metallization of fluid hydrogen at 140 GPa (1.4 Mbar): implications for Jupiter. Planet. Space Sci., **48**(June), 671–677.

Nellis, W. J., Weir, S. T., Holmes, N. C., Ross, M., & Mitchell, A. C. 1998. Hydrogen at high pressures and temperatures: Implications for Jupiter. *Washington DC American Geophysical Union Geophysical Monograph Series*, **101**, 357–364.

O'Connell, D. J. K. 1951. The so-called periastron effect in close eclipsing binaries ; New variable stars (fifth list). *Publications of the Riverview College Observatory*, **2**(Aug.), 85–100.

Osaki, Y. 1965. Mass-Luminosity Relationship in Close Binary Systems of W Ursae Majoris Type. , **17**, 97.

Ostriker, J. P., & Mark, J. W.-K. 1968. Rapidly rotating stars. I. The self-consistent-field method. ApJ, **151**(Mar.), 1075–1088.

Paczyński, B. 1971. Evolutionary Processes in Close Binary Systems. ARA&A, **9**, 183.

Paczyński, B., Szczygieł, D. M., Pilecki, B., & Pojmański, G. 2006. Eclipsing binaries in the All Sky Automated Survey catalogue. MNRAS, **368**(May), 1311–1318.

Padmanabhan, T. 2001. *Theoretical Astrophysics, Volume 2: Stars and Stellar Systems*.

Passy, J.-C., De Marco, O., Fryer, C. L., Herwig, F., Diehl, S., Oishi, J. S., Mac Low, M.-M., Bryan, G. L., & Rockefeller, G. 2011 (Sept.). Simulations of the Common Envelope Interaction Between a Red Giant Branch Star and Low-Mass Companions. *Page 107 of:* Schmidtobreick, L., Schreiber, M. R., & Tappert, C. (eds), *Evolution of Compact Binaries*. Astronomical Society of the Pacific Conference Series, vol. 447.

Paxton, B., Bildsten, L., Dotter, A., Herwig, F., Lesaffre, P., & Timmes, F. 2011. Modules for Experiments in Stellar Astrophysics (MESA). ApJS, **192**(Jan.), 3.

Peaceman, D. W., & Rachford, H. H. 1955. The Numerical Solution of Parabolic and Elliptic Differential Equations. *Journal of the Society for Industrial and Applied Mathematics*, **3**(1), 28–41.

Press, W., Teukolsky, S., Vetterling, W., & Flannery, B. 1986. *Numerical Recipes in Fortran*. 2nd edn. Cambridge University Press.

Pribulla, T., & Rucinski, S. M. 2006. Contact Binaries with Additional Components. I. The Extant Data. AJ, **131**(June), 2986–3007.

Rappaport, S., Verbunt, F., & Joss, P. C. 1983. A new technique for calculations of binary stellar evolution, with application to magnetic braking. ApJ, **275**(Dec.), 713–731.

Rasio, F. A. 1995. The minimum mass ratio of W Ursae Majoris binaries. APJ, **444**(May), L41–L43.

Retter, A., & Marom, A. 2003. A model of an expanding giant that swallowed planets for the eruption of V838 Monocerotis. MNRAS, **345**(Oct.), L25–L28.

Richardson, L. F. 1911. The Approximate Arithmetical Solution by Finite Differences of Physical Problems Involving Differential Equations, with an Application to the Stresses in a Masonry Dam. *Philosophical Transactions of the Royal Society of London A: Mathematical, Physical and Engineering Sciences*, **210**(459-470), 307–357.

Robertson, J. A., & Eggleton, P. P. 1977. The evolution of W Ursae Majoris systems. MNRAS, **179**(May), 359–375.

Ruciński, S. M. 1973. The W UMa-type Systems as Contact Binaries. I. Two Methods of Geometrical Elements Determination. Degree of Contact. Acta Astronomica, **23**, 79.

Rucinski, S. M. 1988. Rotational properties of composite polytrope models. AJ, **95**(June), 1895–1907.

Rucinski, S. M. 1993. A simple description of light curves of W UMa systems. PASP, **105**(Dec.), 1433–1440.

Rucinski, S. M. 1998. Contact Binaries of the Galactic Disk: Comparison of the Baade's Window and Open Cluster Samples. AJ, **116**(Dec.), 2998–3017.

Rucinski, S. M. 2000. W UMA-Type Binary Stars in Globular Clusters. AJ, **120**(July), 319–332.

Rucinski, S. M. 2006. Luminosity function of contact binaries based on the All Sky Automated Survey (ASAS). MNRAS, **368**(May), 1319–1322.

Schatzman, E. 1962. A theory of the role of magnetic activity during star formation. *Annales d'Astrophysique*, **25**(Feb.), 18.

Schönberg, M., & Chandrasekhar, S. 1942. On the Evolution of the Main-Sequence Stars. ApJ, **96**(Sept.), 161.

Shu, F. H. 1980. Theories of contact binary stars. *Pages 477–483 of:* Plavec, M. J., Popper, D. M., & Ulrich, R. K. (eds), *Close Binary Stars: Observations and Interpretation*. IAU Symposium, vol. 88.

Shu, F. H., Lubow, S. H., & Anderson, L. 1976a. On the structure of contact binaries. I - The contact discontinuity. ApJ, **209**(Oct.), 536–546.

Shu, F. H., Lubow, S. H., & Anderson, L. 1976b. On the structure of contact binaries. I - The contact discontinuity. ApJ, **209**(Oct.), 536–546.

Skumanich, A. 1972. Time Scales for CA II Emission Decay, Rotational Braking, and Lithium Depletion. ApJ, **171**(Feb.), 565.

Snellen, I. A. G., Brandl, B. R., de Kok, R. J., Brogi, M., Birkby, J., & Schwarz, H. 2014. Fast spin of the young extrasolar planet β Pictoris b. Nature, **509**(May), 63–65.

Soker, N., & Tylenda, R. 2003. Main-Sequence Stellar Eruption Model for V838 Monocerotis. APJ, **582**(Jan.), L105–L108.

Staff, J., Menon, A., Herwig, F., Clayton, G. C., Even, W. P., Fryer, C. L., Motl, P., Tohline, J. E., Geballe, T., & Pignatari, M. 2013 (Jan.). Simulations of White Dwarf Mergers. *Page 137 of: 18th European White Dwarf Workshop.* Astronomical Society of the Pacific Conference Series, vol. 469.

Staff, J., Wiggins, B., Marcello, D., & Motl, P. M. 2017. The role of dredge-up in double white dwarf mergers. **in press**.

Staff, J. E., Menon, A., Herwig, F., Even, W., Fryer, C. L., Motl, P. M., Geballe, T., Pignatari, M., Clayton, G. C., & Tohline, J. E. 2012. Do R Coronae Borealis Stars Form from Double White Dwarf Mergers? ApJ, **757**(Sept.), 76.

Stępień, K. 1995. Loss of angular momentum of cool close binaries and formation of contact systems. MNRAS, **274**(June), 1019–1028.

Stępień, K. 2006. Evolutionary Status of Late-Type Contact Binaries. Acta Astronomica, **56**(June), 199–218.

Stępień, K. 2009. Large-scale circulations and energy transport in contact binaries. MNRAS, **397**(Aug.), 857–867.

Stępień, K. 2011. Evolution of the progenitor binary of V1309 Scorpii before merger. A&A, **531**(July), A18.

Stępień, K., Schmitt, J. H. M. M., & Voges, W. 2001. ROSAT all-sky survey of W Ursae Majoris stars and the problem of supersaturation. A&A, **370**(Apr.), 157–169.

Stone, J. M., Mihalas, D., & Norman, M. L. 1992. ZEUS-2D: A radiation magnetohydrodynamics code for astrophysical flows in two space dimensions. III - The radiation hydrodynamic algorithms and tests. ApJS, **80**(June), 819–845.

Sugimoto, D., & Fujimoto, M. Y. 2000. Why Stars Become Red Giants. ApJ, **538**(Aug.), 837–853.

Tassoul, J.-L. 1978. *Theory of rotating stars*.

Tohline, J. E. 2002. The Origin of Binary Stars. ARA&A, **40**, 349–385.

Tylenda, R., Hajduk, M., Kamiński, T., Udalski, A., Soszyński, I., Szymański, M. K., Kubiak, M., Pietrzyński, G., Poleski, R., Wyrzykowski, Ł., & Ulaczyk, K. 2011. V1309 Scorpii: merger of a contact binary. A&A, **528**(Apr.), A114.

van der Sluys. 2006. Ph.D. thesis, Utrecht University.

Vilhu, O. 1982. Detached to contact scenario for the origin of W UMa stars. A&A, **109**(May), 17–22.

Vilhu, O., & Moss, D. 1986. Magnetic braking in cool dwarfs. AJ, **92**(Nov.), 1178–1182.

Yakut, K., & Eggleton, P. P. 2005. Evolution of Close Binary Systems. ApJ, **629**(Aug.), 1055–1074.

Zeipel, H. V. 1925. The generation of energy in a star rotating as a rigid body. Reply to Dr. Jeans' criticism. MNRAS, **85**(June), 678.

Appendix: Copyright Permissions

Figures 1.1, 2.1, 2.2, 2.3, 2.4, 2.5, 2.6, 2.7, 2.8, 2.9, 2.10, 4.2, 6.3, 6.4 and Table 2.1 are reprinted with permissions from respective authors or under fair use (Chicago Manual of Style, 15th ed.).

Vita

Kundan Kadam was born on December 4th 1984, in Bombay, India. He finished his undergraduate studies at Sathaye College in April 2005. He earned a Master of Science degree in astronomy and space physics from the University of Mumbai in April 2007. In August 2009 he joined the Louisiana State University to pursue graduate studies. He is currently a candidate for the degree of Doctor of Philosophy in physics, which will be awarded in May 2017.